Embedding Morphoelasticity in Agent-Based Model for Wound Contraction in Burn Injuries

Thesis report

W.S. Gorter

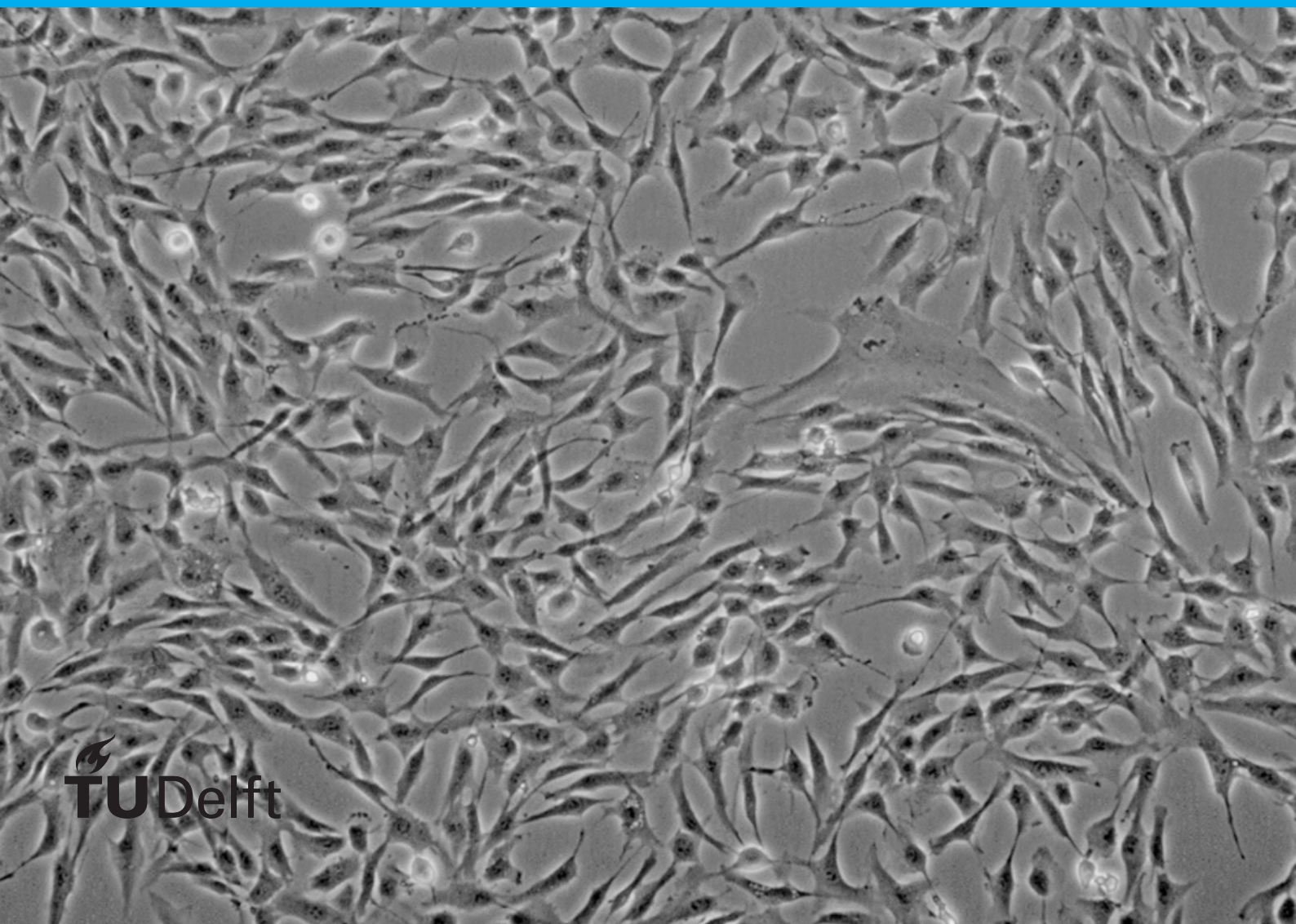

TU Delft

Embedding Morphoelasticity in Agent-Based Model for Wound Contraction in Burn Injuries

Thesis report

by

W.S. Gorter

to obtain the degree of Master of Science
at the Delft University of Technology,
to be defended publicly on Tuesday January 15, 2021 at 10:00 AM.

Program:	Applied Mathematics	
Specialization:	Compuational Science and Engineering	
Student number:	4392841	
Project duration:	February 3, 2020 – January 15, 2021	
Thesis committee:	Prof. dr. ir. F.J. Vermolen,	TU Delft / UHASSELT, supervisor
	Drs. ing. E.K. van Es,	VORtech bv, supervisor
	Dr. H.M. Schuttelaars,	TU Delft
Guest member:	Q. Peng, MSc	TU Delft, daily supervisor

An electronic version of this thesis is available at `http://repository.tudelft.nl/`.

TU Delft VORTECH

Preface

This the report of my Master's thesis, which I finished in January 2021. During this thesis project, I worked on an agent-based model for burn injuries. It was a very enriching experience to apply the theory which I have learned during my study to a practical case. It was highly motivating to know that my project is part of a bigger framework of research, which, in future, possibly can be used in practice.

During my thesis project, the worldwide Covid-19 crisis started, which means that a pretty large part of my project had to be carried out at home. Although this made things more difficult, I am grateful to have had the opportunity to carry out and to finish this project.

At first, I am grateful to God, who I believe is the Creator of the universe and who gave me the mental and physical ability to do this work. Secondly, I want to thank my supervisors. My TU Delft supervisor was Fred Vermolen. During the first period of my thesis work, when there were no restrictions due to Covid-19, you always welcomed me warmly at your office and we never started discussing my work before I received a cup of tea. I really appreciated that you always encouraged me to go on and you were never pessimistic. One thing I have learned from you is: 'for every question you solve, another question rises', which is the fuel of science. After Covid-19 came in (and you left to the University of Hasselt), we had many online meetings, in which the tea lacked, but the quality of your ideas was as high as before.

My supervisor at VORtech bv was Eli van Es. From you I learned the first principles of working with Linux and programming in C++. If I had a question about these kind of subjects, you were always available to help, even when it turned out that the duration of my project was going to be considerably longer than initially planned. Thank you for the support and for your patience when explaining difficult programming subjects. I also want to thank the other colleagues at VORtech. The ambiance at VORtech is very pleasant, which is for example reflected during the joint lunch time. Although currently, this is not possible because of working from home, I believe it will be the same when the Covid-19 crisis is over. It was a very enjoyable experience to be an intern at VORtech.

Next to Fred, I got another supervisor at TU Delft who is usually called Alice (but whose official name is Qiyao Peng). As PhD student, you are studying the same topic as I did in my thesis work and hence you were perfectly capable to be my daily supervisor when Fred went to Hasselt. When I started writing my final report, in my opinion you were very critical on my (English) writing an you had many comments. But now I am convinced my English writing indeed could be improved a lot (and it can still be improved...). I am very grateful that you helped me with this and you were always ready to answer my questions.

Finally, I am grateful to my family and friends for encouraging me, showing their interest and attending my (online) graduation defense. In particular, I want to thank my wife Maartje for standing together with me, during enjoyable moments as well as during tough moments. Many thanks for your love and support!

W.S. Gorter
Rotterdam, January 2021

Contents

1

Introduction

Burn injuries form a very specific type of skin wounds, which can cause much suffering and inconvenience to the patients. One who has serious burn injuries, can be literally scarred for life due to the complications developed post wounding. Wound contracture is one of the symptoms that is characteristic for burn injuries and it can yield many complications. At the location of the wound, an unusual large number of fibroblasts accumulates. This is a type of skin cells that exert forces on their direct neighbourhood. Normally, skin is elastic and if forces are removed, the skin recovers to its original shape again. However, in the case of burn injuries, the forces can be so strong, that the skin, like other elastic materials, deforms permanently. Hence, contractures, excessive and pathological contractions are developed. Investigating the healing of burn injuries is necessary to obtain more insights and to know which factors can influence wound contraction and scar formation. This could be helpful in order to give a treatment that is better in tune to avoid complications as much as possible.

In this thesis, the main goal is to collaborate the morphoelastic model [18] into the agent-base model for wound healing [12]. The agent-based model [12] describes the healing process in the perspective of displacements of cells with various phenotypes, and dynamics of the concentration of different chemokines. The morphoelastic model [18] provides an advanced model to describe the permanent plastic deformation as a consequence of excessive forces. The new model that is developed in this thesis is a more complete and generic model which uses the components from the aforementioned models as well as new features that are added.

To validate the model and estimate the probability of the occurrence of contractures, a large number of simulations are necessary. Hence, for the sake of computational efficiency, this model will be implemented in C++. Currently, the agent-based model has already been developed in C++; see [12] for more details. The implementation of the morphoelastic model in C++ will be carried out in this report. Hence, a relatively large part of this report is dedicated to the development of the morphoelastic part of the model.

In Chapter 2, the biological background and preliminary knowledge is given. In Chapter 3, various models to describe deformation are presented in one dimension and they are extended to higher dimensionality in Chapter 4. Chapter 5 illustrates how cell traction forces are implemented in the form of Dirac Delta distributions in the two-dimensional morphoelastic model. Furthermore, it is investigated how the model reacts to several parameters. In Chapter 6, the morphoelastic model is incorporated in the agent-based model. Monte Carlo simulations are carried out to get more insights into the model. Chapter 7 focuses on the improvements on computational efficiency, which is the basis of the parallel computing in the forthcoming work. Finally, Chapter 8 contains the conclusion, discussions and suggestions for future work.

2

Biological Background

In this chapter, at first a general description of the skin and dermal wound healing is given. Subsequently, basic knowledge of described, which is necessary for the development and investigation of the (morpho)elastic models. In the last section, several modelling options for burn injuries are described.

2.1. Skin structure and dermal wound healing

The descriptions in this section are based on [12], [18] and [21]. The human skin consists of three layers: epidermis, dermis and hypodermis (see Figure 2.1). The epidermis is a very thin layer (approximately 0.1 millimeter) at the top of the skin, which protects the skin against infection from pathogens and against ultraviolet radiation. It plays a role in the regulation of perspiration as well. Below the epidermis, the dermis is located, which is much thicker than the epidermis (approximately 0.5 to 5 millimeter, depending on the location at the body). It consists of cells of several phenotypes and it contains the extracellular matrix (ECM), which is the largest component of the dermis. Furthermore, the dermis harbours blood vessels and other biological materials. During the healing of a dermal wound, the fibroblasts are the main components to maintain the ECM. The bottom layer of the skin is called the hypodermis, which connects the dermis to the tissue below the skin. It mainly contains fat cells which are held in a framework of collagen fibres [6]. The hypodermis is also called subcutis.

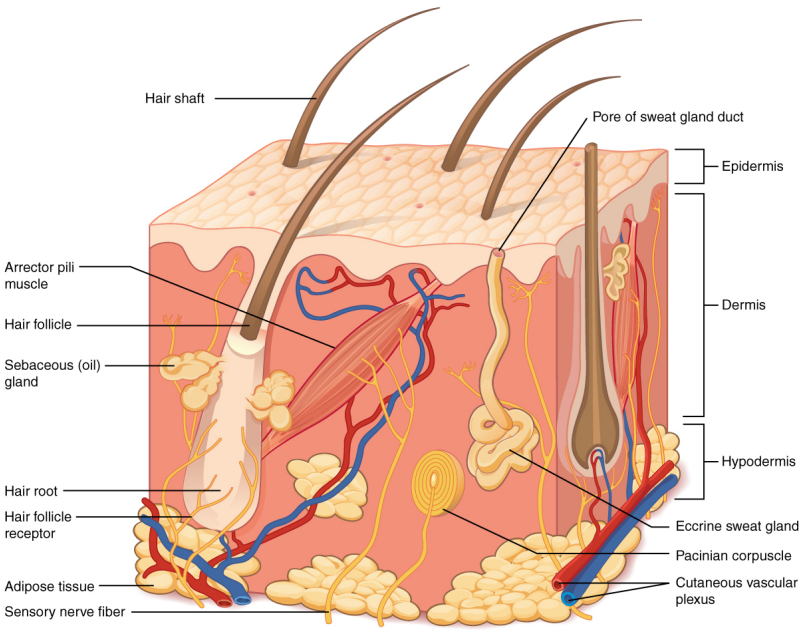

Figure 2.1: A schematic of human skin. Source: [14]

The healing process of dermal wounds (in which the dermis is damaged) consists of four partially overlapping stages, namely hemostasis, inflammation, profliferation and maturation [9], [16], [18]. The main features of the four stages are described below.

1. Hemostasis
   The hemostasis starts immediately after the wounding. During this stage, the injury stops bleeding by formation of blood clots. The blood vessels near the injury constrict in order to prevent further blood loss. Furthermore, platelets stick together and to the injured skin. To form a fibrin network, the platelets release several chemokines (also called signaling molecules). These are the chemicals that influence the production and the behavior of cells, for example Platelet Derived Growth Factor (PDGF) and Transforming Growth Factor β (TGF-β). The hemostasis stage usually lasts a few days. In the case of burn injuries, there is almost no hemostatis.

2. Inflammation
   The inflammation is the main process of wound healing. This phase is characterised by a high activity of the immune system. For instance, white blood cells enter the wound, which clean the wound of bacteria and other harmful elements and stimulate the forming of new blood vessels. An example of a white blood cell type is the macrophage, which is the main phenotype secreting TGF-β. This stage starts some days after the injury and lasts approximately one week.

3. Proliferation
   In this stage, many parts of the skin are restored and contraction occurs. The epidermis is restored and the production of new blood vessels is continued. The number of cells increase as a consequence of cell division. In particular, fibroblasts are attracted to the wound area from the uninjured region by high concentrations of TGF-β. Furthermore, high concentrations of TGF-β will trigger the fibroblasts to differentiate to myofibroblasts, which exert much larger forces on their direct neighbourhood. Next to it, (myo)fibroblasts release the collagen that is needed to rebuild the ECM. The proliferation stage starts approximately five days after the injury and can last several weeks.

4. Maturation
   In this phase, the ECM is remodelled, which means that the structure is changing. In particular, collagen of type III is replaced by collagen type I, which is stiffer and has a more randomized orientation, whereas type III has a nonisotropic orientation. This stage starts during the last part of the proliferation stage and can last several years, depending on the wound.

2.2. Principles of elasticity theory

In this section, we will introduce the relevant quantities in elasticity theory and explain the relations between them. The descriptions are based on [7], [11] and [18],

2.2.1. Definition of stress

The first important quantity is stress, most commonly denoted with σ. It is defined by

$$\sigma := \frac{F}{A_c}. \tag{2.2.1}$$

Here, F denotes the force and A_c denotes a cross-sectional area on which the force is exerted. We assume here that the force is exerted perpendicular to the area, which is called normal stress. Later, we will introduce the concept of shear stress, which is the force being exerted tangential to the area. As an example of normal stress, one could think of a bar on which a force is exerted at both ends. If the bar is stretched, the stresses are called tensile normal stresses. It is called compressive normal stress if the force is reversed in direction, causing the bar to compress. In this example, A_c is the area of the grey-coloured surface (see Figure 2.2). Furthermore, in Equation (2.2.1), it is assumed that the force is uniformly distributed over the area, which is a special case. If the force is non-uniformly distributed, one could define the stress on a more local scale as

$$\sigma(\boldsymbol{x}) = \lim_{A_c \to 0} \frac{\int_\Omega F(\tilde{\boldsymbol{x}})\, \mathrm{d}\tilde{\boldsymbol{x}}}{A_c},$$

where $\Omega \in \mathbb{R}^2$, $A_c := A_c(\Omega)$ is the area of Ω and

$$\lim_{A_c \to 0} \Omega = \{\boldsymbol{x}\}.$$

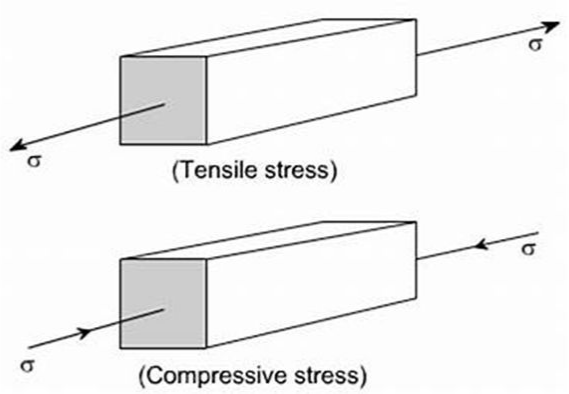

Figure 2.2: Tensile and compressive stress in a bar. Source: [17]

More information on this can for example be found in [7].

2.2.2. Shear stress

Besides normal stress, we need to define shear stress, which is the stress caused by a force exerted tangential to the area (see Figure 2.3). As it can be seen in the figure, shear stress (if it is tensile) causes the area to move in the direction of the exerted force, while the opposite side of the object remains in place. Similarly, shear stress can be defined as $\sigma_s = \frac{F}{A}$. In three dimensions, we have one normal stress vector per dimension and

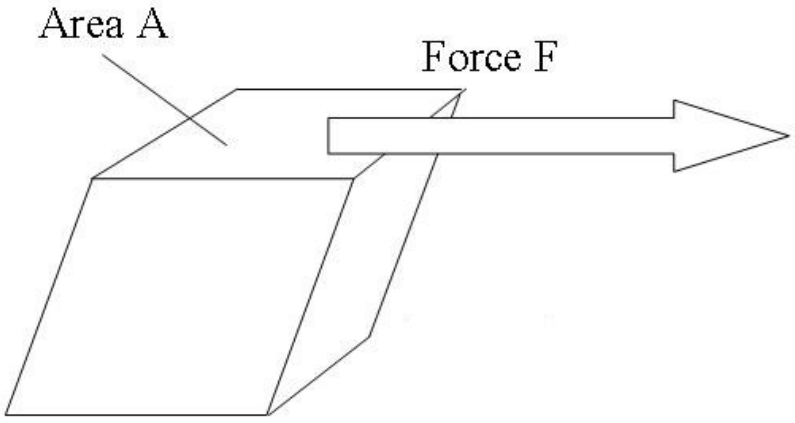

Figure 2.3: Shear stress. Source: [20]

two shear stress vectors per dimension. Hence, the stress becomes a tensor of nine partial stresses:

$$\underline{\underline{\sigma}} := \begin{pmatrix} \sigma_{11} & \sigma_{12} & \sigma_{13} \\ \sigma_{21} & \sigma_{22} & \sigma_{23} \\ \sigma_{31} & \sigma_{32} & \sigma_{33} \end{pmatrix}.$$

In Figure 2.4, we see that σ_{ii} denotes normal stress in direction of basisvector $\boldsymbol{e}_i$ ($i = 1,2,3$), while σ_{ij} denotes shear stress on an area in direction of basisvector $\boldsymbol{e}_i$ ($i = 1,2,3$), with force pointing towards the direction of basisvector $\boldsymbol{e}_j$ ($j = 1,2,3$). The stress tensor at a specific location $\boldsymbol{x} \in \mathbb{R}^3$ can be obtained by letting the cube in Figure 2.4 shrink to one point, namely $\boldsymbol{x}$, and taking the limit of the σ_{ij}'s as the volume of the cube tends to 0.

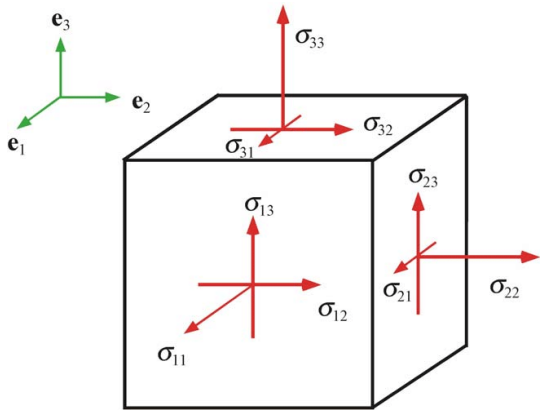

Figure 2.4: Cube with normal and shear stresses in three dimensions. Source: [2]

2.2.3. Displacement and Eulerian and Lagrangian approach

Another important quantity is displacement. Suppose a tensile stress is exerted on a bar, as in Figure 2.2. If the initial length of the bar is $L_0 = L$, the bar will elongate as a consequence of the stress. Suppose the new length of the bar is $L_1 = L + \delta$, then the displacement is defined as

$$u := L_1 - L_0 = L + \delta - L = \delta.$$

Similarly to the stress, the displacement can be defined locally as well. However, this can be done in two ways. Suppose the coordinates of the aforementioned bar are $[0, L_0]$ in initial state and after stretching it out, the coordinates are $[0, L_1]$. The displacement can be defined locally with respect to the new coordinates, but also with respect to the old coordinates. Usually, the new coordinates are denoted with x and the old coordinates with X. Furthermore there is a mapping $x = x(X)$ between the old and the new coordinates (or reversed: $X = X(x)$). The x-coordinates are called Eulerian coordinates, while the X-coordinates are called Lagrangian coordinates. It is important to distinguish between the Eulerian and the Lagrangian approach, since it has a significant impact on the models. The displacement can be defined locally either Eulerian or Lagrangian:

$$u(x) := x - X(x)$$

and

$$u(X) = x(X) - X.$$

Other quantities can also be defined in both ways. Suppose the material has a property c (for instance the concentration of a chemokine), then it can be defined as $c = c(x) = c(X(x))$ or $c = c(X) = c(x(X))$. In particular, the different approaches have an impact on spatial derivatives, which are given by

$$\frac{\mathrm{d}c}{\mathrm{d}x}(x,t) \text{ and } \frac{\mathrm{d}c}{\mathrm{d}X}(X,t),$$

with the mutual relationships

$$\frac{\mathrm{d}c}{\mathrm{d}x}(x) = \frac{\mathrm{d}c}{\mathrm{d}X}(X(x)) \cdot \frac{\mathrm{d}X}{\mathrm{d}x}(x)$$

and

$$\frac{\mathrm{d}c}{\mathrm{d}X}(X) = \frac{\mathrm{d}c}{\mathrm{d}x}(x(X)) \cdot \frac{\mathrm{d}x}{\mathrm{d}X}(X).$$

Suppose that c is not only dependent on the location but also on time t, that is,

$$c = c(x,t) = c(X(x),t).$$

Then the mapping between x and X is dependent on time as well: $x = x(X,t)$. Subsequently, we have the Eulerian partial time derivative

$$\frac{\partial c}{\partial t}(x,t),$$

and the Langrangian time derivative

$$\frac{\partial c}{\partial t}(X,t) = \frac{\partial c}{\partial t}(x(X),t) + \frac{\partial c}{\partial x}(x(X),t) \cdot \frac{\mathrm{d}x}{\mathrm{d}t}(X,t).$$

The latter derivative is called the material derivative, which is, in Eulerian coordinates, commonly denoted by

$$\frac{\mathrm{D}c}{\mathrm{D}t} := \frac{\partial c}{\partial t} + v\frac{\partial c}{\partial x}.$$

The expression

$$v := \frac{\partial x}{\partial t}(X,t) = \frac{\mathrm{D}u}{\mathrm{D}t}(x,t)$$

is the velocity of the particle with initial position $x(X,0) = X$. The material derivative obeys the normal differentiation rules, such as the Product Rule.

2.2.4. Definition of strain

The concept of strain describes the extent to which the material is stretched as a consequence of exerted forces. Suppose we have a bar of length L to which a force is exerted at the ends, causing the bar to be stretched to a length of $L+\delta$. Then the strain, commonly denoted with ε is defined as

$$\varepsilon := \frac{L_1 - L_0}{L_0} = \frac{\delta}{L}.$$

This is an Eulerian global definition of strain. Actually, strain is a ratio that represents the elongation per unit length. As in the case of stress, strain can be defined locally as well. The local Eulerian strain is defined as

$$\varepsilon(x) := \frac{\mathrm{d}u}{\mathrm{d}x}.$$

In Lagrangian coordinates, strain is expressed as:

$$\varepsilon(X) := \frac{\mathrm{d}u}{\mathrm{d}X}.$$

Globally, the latter definition corresponds with

$$\varepsilon_L := \frac{L_1}{L_0} = \frac{L+\delta}{L}.$$

Similar to stress, strain can be defined in three dimension with normal strain and shear strain. Analogously to the case of stress (see Section 2.2.1), strain can be defined as a tensor in three dimensions:

$$\underline{\underline{\varepsilon}} := \begin{pmatrix} \varepsilon_{11} & \varepsilon_{12} & \varepsilon_{13} \\ \varepsilon_{21} & \varepsilon_{22} & \varepsilon_{23} \\ \varepsilon_{31} & \varepsilon_{32} & \varepsilon_{33} \end{pmatrix}.$$

However, there are several ways in which the strain tensor is defined. For now we choose the following definition, in accordance with [18]:

$$\underline{\underline{\varepsilon}} := \frac{1}{2}\left(\nabla u + (\nabla u)^T\right). \tag{2.2.2}$$

Note that, if we use Eulerian coordinates, then

$$\nabla = \nabla^E := \begin{pmatrix} \frac{\partial}{\partial x} \\ \frac{\partial}{\partial y} \\ \frac{\partial}{\partial z} \end{pmatrix},$$

whereas in Lagrangian coordinates,

$$\nabla = \nabla^L := \begin{pmatrix} \frac{\partial}{\partial X} \\ \frac{\partial}{\partial Y} \\ \frac{\partial}{\partial Z} \end{pmatrix}.$$

2.2.5. Poisson's effect

The Poisson's effect is a phenomenon that is important in elasticity theory and that we will use in our models. If the material is stretched in a certain direction, then it will be compressed in the perpetual directions. Simi-

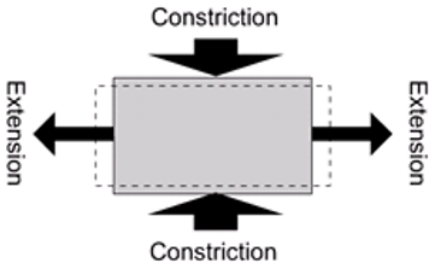

Figure 2.5: Poisson's effect in two dimensions. The solid lines represent the original shape and the dashed lines represent the deformed shape. Source: [5]

larly, if it is compressed in a certain direction, then it will be stretched in the other directions. In Figure 2.5, an illustration of the phenomenon in two dimensions is given: a rectangle is stretched in the x-direction, which causes a constriction in the y-direction. A dimensionless quantity called Poisson's ratio is used in order to measure the Poisson's effect:

$$\eta := -\frac{\varepsilon_y}{\varepsilon_x} = \frac{\partial u}{\partial x}\frac{\partial y}{\partial u}.$$

In the case of isotropic material, we have that the Poisson's effect in z-direction is equal to the effect in y-direction. Hence, η is valid for both the y- and the z-direction. In the literature, Poisson's ratio is usually denoted with a ν instead of an η [16], [18]. However, in order to prevent confusion with the velocity v, in this thesis we will denote it by an η.

2.2.6. Viscosity

There is another important phenomenon that has to be described, namely viscosity. This can be illustrated with a dashpot, see Figure 2.6. The dashpot is filled with a fluid. One can imagine, if the fluid is very viscous,

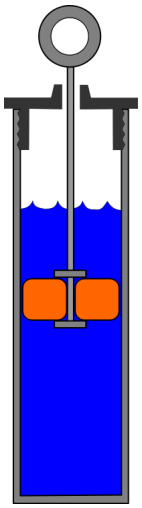

Figure 2.6: Dashpot. Source: [24]

for example oil or syrup, it becomes very hard to move the piston through the dashpot. Opposite to the case of elasticity, stress does not immediately result in strain. In other words, viscosity is a measure of resistance from the fluid and it can be conceptualized as an inner friction.

2.3. Morphoelasticity

Morphoelasticity describes what happens if the deformation of a material becomes too large. In Figure 2.7, the relation between the stress and the strain is shown, which is subdivided in mainly two regions. In these regions, the material behaves differently. In the next two subsections, this will be explained in more detail.

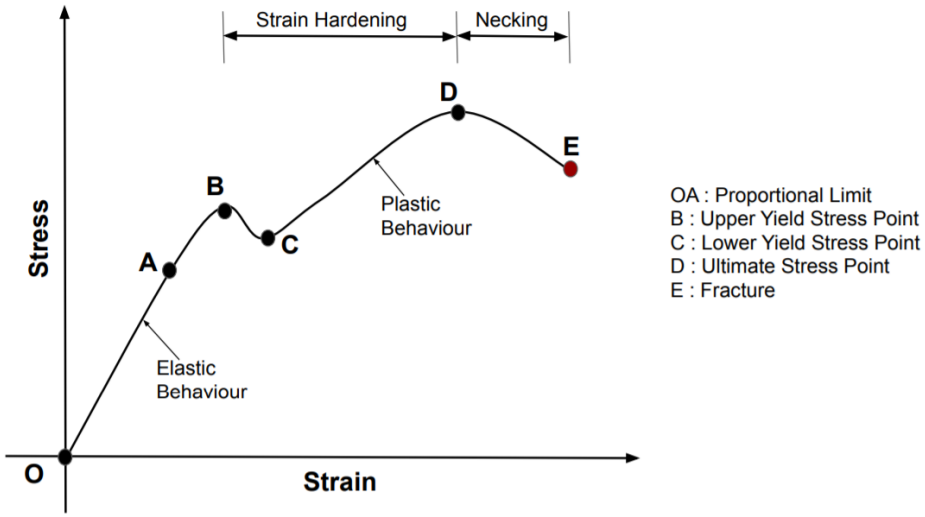

Figure 2.7: Stress-strain curve with several regions of deformation. Source: [19]

2.3.1. Linear region

For small values of σ, there exists a linear relation between stress and strain, that is,

$$\sigma = E_s \varepsilon, \tag{2.3.1}$$

which is known as Hooke's law. The parameter E_s is called the Young's modulus. The interval $[0, \varepsilon_0]$, with $\varepsilon_0 := \max\{\varepsilon > 0 : \text{Hooke's law is applicable}\}$, is called the linear region and the magnitude of ε_0 differs per material. For shear stresses, the Young's modulus is not equal to the Young's modulus for normal stresses. Hence, we introduce the shear modulus ζ, so that, for $i, j \in \{1,2,3\}$,

$$\sigma_{ij} = \begin{cases} E_s \varepsilon_{ij}, & \text{if } i = j, \\ \zeta \varepsilon_{ij}, & \text{if } i \neq j. \end{cases} \tag{2.3.2}$$

It can be proven that ζ is related to E_s and to the Poisson's ratio η, in the following way (see [11] and [18]):

$$\zeta = \frac{E_s}{(1+\eta)}. \tag{2.3.3}$$

For the normal strain in three dimensions, we have

$$E_s \varepsilon_{11} = \sigma_{11} - \eta\sigma_{22} - \eta\sigma_{33}. \tag{2.3.4}$$

Here, the right-hand side part σ_{11} accounts for the normal one-dimensional Hooke's law, while the part $\eta\sigma_{22} + \eta\sigma_{33}$ incorporates the Poisson's effect. For ε_{22} and ε_{33}, the same can be done, yielding

$$\begin{pmatrix} \sigma_{11} \\ \sigma_{22} \\ \sigma_{33} \end{pmatrix} = E_s \begin{pmatrix} 1 & -\eta & -\eta \\ -\eta & 1 & -\eta \\ -\eta & -\eta & 1 \end{pmatrix}^{-1} \begin{pmatrix} \varepsilon_{11} \\ \varepsilon_{22} \\ \varepsilon_{33} \end{pmatrix} \tag{2.3.5}$$

$$= \frac{E_s}{1+\eta} \begin{pmatrix} \eta/(1-2\eta)+1 & \eta/(1-2\eta) & \eta/(1-2\eta) \\ \eta/(1-2\eta) & \eta/(1-2\eta)+1 & \eta/(1-2\eta) \\ \eta/(1-2\eta) & \eta/(1-2\eta) & \eta/(1-2\eta)+1 \end{pmatrix} \begin{pmatrix} \varepsilon_{11} \\ \varepsilon_{22} \\ \varepsilon_{33} \end{pmatrix}. \tag{2.3.6}$$

Furthermore, considering the shear strain, we have established that

$$\sigma_{ij} = \zeta \varepsilon_{ij} = \frac{E_s}{1+\eta} \varepsilon_{ij}. \tag{2.3.7}$$

Altogether, this yields

$$\underline{\underline{\sigma}} = \frac{E_s}{1+\eta} \left(\underline{\underline{\varepsilon}} + \frac{\eta}{1-2\eta} \mathrm{Tr}(\underline{\underline{\varepsilon}}) \mathrm{I} \right). \tag{2.3.8}$$

Here, $\mathrm{Tr}(\underline{\underline{\varepsilon}}) := \varepsilon_{11} + \varepsilon_{22} + \varepsilon_{33}$ is the trace of $\underline{\underline{\varepsilon}}$ and I denotes the 3×3-identity matrix. This establishes Hooke's law generalized to three dimensions.

2.3.2. Plastic deformation

The deformation that occurs in the linear region is called elastic deformation. If the strain exceeds the linear region, the material will behave in another way. Beyond the linear region, plastic deformation will occur: the material is deformed permanently. The process of permanent deformation being formed, is called morphoelasticity.

If the material is only deformed elastically, it can be totally restored to the initial state when it is released from stress. However, if the stress passes beyond the linear region, it will cause a permanent distortion in the material. In the context of burn wounds, this phenomenon causes wound contracture and increased scar formation. Hence, it is important to incorporate morphoelasticity into the model. Two types of cells called fibroblasts and myofibroblasts are mainly involved in the contraction of the skin. As it was mentioned earlier, in pacticular the myofibroblasts exert larger forces on the direct surrounding area. Furthermore, (myo)fibroblasts produce collagen I fibres, which is of another type then the usual collagen III. Collagen I is more isotropic and stronger, which causes contraction as well. During the proliferation stage, the (myo)fibroblast density is often larger in the wound area than in the surrounding healthy skin [12]. As a consequence of the contractile forces, the area of the wound shrinks and hence the (initially undamaged) skin around the wound is also stretched towards the wound. When, eventually, the wound is healed, in most severe cases, there is a remaining deformation of the skin, which may lead to contractures.

2.4. Agent-based model

There are different ways to model the cells in the skin [23]. There are mainly two categories of models, namely models based on cell densities and agent-based models, which model the individual cells as particles. The model that is developed in this thesis is an agent-based model. This type of models has several advantages. Firstly, it contains more parameters that can be measured in experiments and it is more realistic. Secondly, it is easier to incorporate stochastic components into the model and to investigate their influence on the cells. Furthermore, the biological processes are easier to visualize in these models, which is an advantage when presenting the results to medical professionals. However, agent-based models have a nonnegligible drawback as well: the computational cost are much larger than for cell density models. This is due to the fact that for every iteration, the displacements of all the cells has to be computed separately. As a result, the agent-based model is less suitable when modelling on a large scale. However, the computational cost can be reduced by an efficient implementation. For example, the cell displacements are suitable for implementation on the GPU, which increases the efficiency of computation.

3

Preliminaries: one-dimensional model of force balance

In this chapter, several one-dimensional models will be derived. The derivations are based on [18]. The Cauchy Momentum Equation lies at the root of all the models, hence in the first section this equation will be derived. In the subsequent sections, the several models are stated and the numerical aspects are addressed. The results are presented in the last section.

3.1. Cauchy Momentum Equation

The Cauchy Momentum Equation relates the impulse of a movement to the exerted forces on the moving area. Therefore, the Cauchy Momentum Equation is the continuum analogue of Newton's second law:

$$\boldsymbol{p} := m\boldsymbol{v}, \tag{3.1.1}$$

where $\boldsymbol{p}$ denotes the impulse and m and $\boldsymbol{v}$ are the mass and the velocity respectively. Hence, the impulse represents the 'amount of movement'. Newton's second law now prescribes that the change of the impulse in time is proportional to the resultant of the exerted force:

$$\boldsymbol{F}_{\text{res}} = \frac{\mathrm{d}\boldsymbol{p}}{\mathrm{d}t}, \tag{3.1.2}$$

where $\boldsymbol{F}_{\text{res}}$ is the resulting force, that is, the sum of all (directed) forces exerted on the object. Let $\Omega(t) = [x_0(t), x_1(t)] \times [y_0(t), y_1(t)] \times [z_0(t), z_1(t)]$ be a cube in $\mathbb{R}^3$. Considering the x-direction, in this continuum case, the impulse over Ω is the product of the local densities and velocities, integrated over the volume of Ω:

$$p_1 = \int_\Omega \rho v_1 \, \mathrm{d}\Omega, \tag{3.1.3}$$

where p_1 and v_1 denote the impulse and velocity in x-direction. The forces working on Ω fall into two categories, namely internal and external forces. The internal forces are usually called body forces. Denoting with f_1 the resultant body force per unit volume in the x-direction, we have

$$(F^b_{\text{res}})_1 = \int_\Omega f_1 \, \mathrm{d}\Omega. \tag{3.1.4}$$

The external forces can be computed based on the stresses. For example, considering the normal stress in x-direction σ_{11}, we have that the resulting external force is equal to the difference in the normal forces at x_1

and those at x_0:

$$\begin{aligned}(F_{\text{res}}^{\text{ext}})_{11} = (F_{\text{ext}})_{11}(x_1) - (F_{\text{ext}})_{11}(x_0) &= A\tilde{\sigma}_{11}(x_1) - A\tilde{\sigma}_{11}(x_0)\\ &= (y_1-y_0)(z_1-z_0)\left(\tilde{\sigma}_{11}(x_1)-\tilde{\sigma}_{11}(x_0)\right)\\ &= \int_{z_0}^{z_1}\int_{y_0}^{y_1} \sigma_{11}(x_1,y,z)-\sigma_{11}(x_0,y,z)\,\mathrm{d}A \qquad (3.1.5)\\ &= \int_{z_0}^{z_1}\int_{y_0}^{y_1}\int_{x_0}^{x_1} \frac{\partial\sigma_{11}}{\partial x}(x,y,z)\,\mathrm{d}\Omega\\ &= \int_{\Omega}\frac{\partial\sigma_{11}}{\partial x}\,\mathrm{d}\Omega.\end{aligned}$$

Here, $\tilde{\sigma}_{11}(x_i)$ denotes the average of σ_{11} over the surface $S := \{(x,y,z) : x = x_i, y \in [y_0,y_1], z \in [z_0,z_1]\}$ and $A := A(S)$ is the area of S. Other stress in the x-direction are the shear stress σ_{21} and σ_{31}. Doing the same for these, we obtain

$$(F_{\text{res}}^{\text{ext}})_{21} = \int_{\Omega}\frac{\partial\sigma_{21}}{\partial y}\,\mathrm{d}\Omega \qquad (3.1.6)$$

and

$$(F_{\text{res}}^{\text{ext}})_{31} = \int_{\Omega}\frac{\partial\sigma_{31}}{\partial z}\,\mathrm{d}\Omega.$$

The total resultant force in the x-direction now is equal to

$$\begin{aligned}(F_{\text{res}})_1 = (F_{\text{res}}^{\text{ext}})_1 + (F_{\text{res}}^{b})_1 &= \int_{\Omega}\frac{\partial\sigma_{11}}{\partial x}+\frac{\partial\sigma_{21}}{\partial y}+\frac{\partial\sigma_{31}}{\partial z}\,\mathrm{d}\Omega + \int_{\Omega} f_1\,\mathrm{d}\Omega\\ &= \int_{\Omega}\nabla\cdot\boldsymbol{\sigma}_{\cdot 1} + f_1\,\mathrm{d}\Omega.\end{aligned}$$

Applying Newton's second law, we have

$$\frac{\mathrm{d}}{\mathrm{d}t}\left(\int_{\Omega}\rho v_1\,\mathrm{d}\Omega\right) = \int_{\Omega}\nabla\cdot\boldsymbol{\sigma}_{\cdot 1} + f_1\,\mathrm{d}\Omega. \qquad (3.1.7)$$

We will use Reynold's Transport Theorem (see [16]), in order to move the time derivative into the integral. Let $\Omega(t)$ be a time-dependent domain in $\mathbb{R}^d$ and let $\partial\Omega(t)$ be the boundary of Ω. Furthermore, let f with $\frac{\partial f}{\partial t} \in L^2(\Omega(t))$ be a given function and let $\boldsymbol{v}$ represent the velocity of moving boundary $\partial\Omega(t)$, then

$$\frac{\mathrm{d}}{\mathrm{d}t}\int_{\Omega(t)} f(\boldsymbol{x}(t),t)\mathrm{d}\Omega = \int_{\Omega(t)}\frac{\partial f}{\partial t}(\boldsymbol{x}(t),t)\mathrm{d}\Omega + \int_{\partial\Omega(t)} f(\boldsymbol{x}(t),t)\,\boldsymbol{v}\cdot\boldsymbol{n}\mathrm{d}\Gamma,$$

with $\boldsymbol{n}$ being the outward pointing unit normal vector. Applying **Theorem 3.1** on the left-hand side of Equation (3.1.7), we obtain

$$\begin{aligned}\frac{\mathrm{d}}{\mathrm{d}t}\left(\int_{\Omega(t)}\rho v_1\,\mathrm{d}\Omega\right) &= \int_{\Omega(t)}\frac{\partial(\rho v_1)}{\partial t}\mathrm{d}\Omega + \oint_{\partial\Omega(t)}\rho v_1(\boldsymbol{v}\cdot\boldsymbol{n})\,\mathrm{d}\zeta\\ &= \int_{\Omega(t)}\frac{\partial(\rho v_1)}{\partial t}\mathrm{d}\Omega + \oint_{\partial\Omega(t)}(\rho v_1\boldsymbol{v}\cdot\boldsymbol{n})\,\mathrm{d}\zeta\\ &= \int_{\Omega(t)}\frac{\partial(\rho v_1)}{\partial t}\mathrm{d}\Omega + \int_{\Omega(t)}\nabla\cdot(\rho v_1\boldsymbol{v})\,\mathrm{d}\Omega \qquad (3.1.8)\\ &= \int_{\Omega(t)}\rho\frac{\partial v_1}{\partial t} + v_1\frac{\partial\rho}{\partial t} + v_1\nabla\cdot(\rho\boldsymbol{v}) + \rho\boldsymbol{v}\cdot\nabla v_1\,\mathrm{d}\Omega\\ &= \int_{\Omega(t)}\rho\frac{\partial v_1}{\partial t} + \rho\boldsymbol{v}\cdot\nabla v_1\,\mathrm{d}\Omega\\ &= \int_{\Omega(t)}\rho\frac{\mathrm{D}v_1}{\mathrm{D}t}\,\mathrm{d}\Omega.\end{aligned}$$

Here, $\boldsymbol{v} := (v_1,v_2,v_3)^T$ and in the second last equality, we used the Continuity Equation which reads

$$\frac{\partial\rho}{\partial t} + \nabla\cdot(\rho\boldsymbol{v}) = 0. \qquad (3.1.9)$$

Hence, combining Equation (3.1.7) and (3.1.8), we have

$$\int_{\Omega(t)} \rho \frac{\mathrm{D}v_1}{\mathrm{D}t}\,\mathrm{d}\Omega = \int_{\Omega(t)} \nabla\cdot\boldsymbol{\sigma}_{\cdot 1} + f_1\,\mathrm{d}\Omega. \tag{3.1.10}$$

Considering that Ω was chosen arbitrarily, it follows that

$$\rho \frac{\mathrm{D}v_1}{\mathrm{D}t} = \nabla\cdot\boldsymbol{\sigma}_{\cdot 1} + f_1. \tag{3.1.11}$$

For the y-direction and the z-direction, this can be done analogously, which eventually yields:

$$\rho \frac{\mathrm{D}\boldsymbol{v}}{\mathrm{D}t} = \nabla\cdot\underline{\underline{\sigma}} + \boldsymbol{f}, \tag{3.1.12}$$

where $\boldsymbol{f} = (f_1, f_2, f_3)^T$. This is called the convective form of the Cauchy Momentum Equation. Besides, there exists a conservation form of the Cauchy Momentum Equation, which is derived as follows:

$$\begin{aligned}
\rho \frac{\mathrm{D}\boldsymbol{v}}{\mathrm{D}t} = \frac{\mathrm{D}(\rho\boldsymbol{v})}{\mathrm{D}t} - \boldsymbol{v}\frac{\mathrm{D}\rho}{\mathrm{D}t} &= \frac{\mathrm{D}(\rho\boldsymbol{v})}{\mathrm{D}t} - \boldsymbol{v}\left(\frac{\partial\rho}{\partial t} + \boldsymbol{v}\cdot\nabla\rho\right) \\
&= \frac{\mathrm{D}(\rho\boldsymbol{v})}{\mathrm{D}t} - \boldsymbol{v}\left(\frac{\partial\rho}{\partial t} + \nabla\cdot(\rho\boldsymbol{v}) - \rho(\nabla\cdot\boldsymbol{v})\right) \\
&= \frac{\mathrm{D}(\rho\boldsymbol{v})}{\mathrm{D}t} + \boldsymbol{v}\rho(\nabla\cdot\boldsymbol{v}).
\end{aligned} \tag{3.1.13}$$

In the last equality, we used that $\frac{\partial\rho}{\partial t} + \nabla\cdot(\rho\boldsymbol{v}) = 0$, which is the continuity equation in three dimensions. The conservation form of the Cauchy Momentum Equation now reads as

$$\frac{\mathrm{D}(\rho\boldsymbol{v})}{\mathrm{D}t} + \boldsymbol{v}\rho(\nabla\cdot\boldsymbol{v}) = \nabla\cdot\underline{\underline{\sigma}} + \boldsymbol{f}. \tag{3.1.14}$$

We will use the latter form (Equation 3.1.14) when deriving the viscoelastic and morphoelastic model (Sections 3.3 and 3.4).

3.2. One-dimensional elastic model

In this section, we will consider a one-dimensional elastic model.

3.2.1. Derivation

We use a one-dimensional version of convective form of the Cauchy Momentum Equation derived in Equation 3.1.12:

$$\rho \frac{\mathrm{D}v}{\mathrm{D}t} = \frac{\partial\sigma}{\partial x} + f. \tag{3.2.1}$$

Suppose that we have an equilibrium state, that is, $\frac{\mathrm{D}v}{\mathrm{D}t} = 0$. Then, using Hooke's Law $\sigma = E_s\varepsilon = E_s\frac{\mathrm{d}u}{\mathrm{d}x}$, we obtain the following time-independent model :

$$(BVP): \begin{cases} -E_s\frac{\mathrm{d}^2u}{\mathrm{d}x^2} = f(x),\ 0 < x < L, \\ u(0) = 0, \\ \frac{\partial u}{\partial x}(L) = 0. \end{cases}$$

The model can be made time-dependent by implementing time-dependent body forces:

$$(IBVP_1): \begin{cases} -E_s\frac{\partial^2u}{\partial x^2} = f(x,t), & 0 < x < l(t), t > 0, \\ u(0,t) = 0, & t > 0, \\ \frac{\partial u}{\partial x}(l(t),t) = 0, & t > 0, \\ u(x,0) = 0, & 0 \le x \le l(t), \end{cases}$$

where $l(t) := x(L,t)$. An initial condition is added: there is no displacement at the start.

3.2.2. Numerical aspects

In the appendix, the Weak Form (W) of (BVP) is derived, which yields the following:

$$(W): \begin{cases} \text{Find } u \in H^1(\Omega) \text{ with } u(0) = 0 \text{ such that} \\ E_s \int_0^L u'(x)\phi'(x)\,\mathrm{d}x = \int_0^L f(x)\phi(x)\,\mathrm{d}x, \\ \text{for all } \phi(x) \in H^1(\Omega) \text{ with } \phi(0) = 0. \end{cases}$$

In order to obtain the Galerkin equations, we approximate u with

$$u(x) \approx u^n(x) := \sum_{j=0}^{n} u_j \phi_j(x).$$

Using linear basis functions $\phi = \phi_i(x) := \alpha_i + \beta_i x$ such that $\phi_i(x_j) = \delta_{ij}$. This yields

$$E_s \sum_{j=0}^{n} u_j \int_0^L \phi_i'(x)\phi_j'(x)\,\mathrm{d}x = \int_0^L f(x)\phi_i(x)\,\mathrm{d}x$$

Hence, we obtain a system

$$S\boldsymbol{u} = \boldsymbol{f}.$$

Here, S is an $(n+1)\times(n+1)$-matrix and $\boldsymbol{f}$ is a vector of length $n+1$, with the following element matrix and vector:

$$(S)_{e_m} = \frac{E}{h_{e_m}} \begin{pmatrix} 1 & -1 \\ -1 & 1 \end{pmatrix}, \tag{3.2.2}$$

$$(\boldsymbol{f})_{e_m} = \frac{h_{e_m}}{2} \begin{pmatrix} f(x_{m-1}) \\ f(x_m) \end{pmatrix}, \tag{3.2.3}$$

where e_m denotes the element $[x_{m-1}, x_m]$ and h_e denotes the length of element e_m, which is equal to $x_m - x_{m-1}$. Furthermore, the solution

$$\mathbf{u} := (u_0, \ldots, u_n)^T \tag{3.2.4}$$

at each model point can be solved. As for the model with the time-dependent body force ($IBVP_1$), the weak form will be as follows:

$$(W1): \begin{cases} \text{Find } u \in H^1(\Omega(t)) \text{ with } u(x(0)) = 0 \text{ and } u(0) = 0 \text{ such that} \\ E_s \int_0^{l(t)} \frac{\partial u}{\partial x}(x,t)\phi'(x)\,\mathrm{d}x = \int_0^{l(t)} f(x,t)\phi(x)\,\mathrm{d}x, \\ \text{for all } \phi(x,t) \in H^1(\Omega(t)) \text{ with } \phi(0,t) = 0. \end{cases}$$

The Galerkin equations will be derived in the same way as before, resulting in:

$$E_s \sum_{j=0}^{n} u_j(t) \int_0^{l(t)} \frac{\partial \phi_i}{\partial x}(x,t) \frac{\partial \phi_j}{\partial x}(x,t)\,\mathrm{d}x = \int_0^{l(t)} f(x,t)\phi_i(x,t)\,\mathrm{d}x.$$

This again yields the system

$$S\boldsymbol{u} = \boldsymbol{f}.$$

However, here the vector $\boldsymbol{f}$ is time-dependent, as well as the vector $\boldsymbol{u}$. Hence, for each time iteration $t_i = i \cdot \Delta t$, the system has to be solved separately.

3.2.3. Elastic model with inertia

In the former subsections, $\frac{\mathrm{D}v}{\mathrm{D}t}$ was set to be zero, which means that the inertia was not incorporated. If we suppose $\frac{\mathrm{D}v}{\mathrm{D}t} \neq 0$, then the entire Cauchy Momentum Equation is taken into account. Hence, the differential equation is:

$$\frac{\mathrm{D}v}{\mathrm{D}t} = E_s \frac{\partial^2 u}{\partial x^2} + f,$$

that is,

$$\frac{\mathrm{D}^2 u}{\mathrm{D}t^2} = E_s \frac{\partial^2 u}{\partial x^2} + f.$$

This is actually the wave equation and according to the theory of wave equations, this will yield oscillatory solutions. Subsequently, the numerical solution is oscillatory as well. The derivation of the weak form and the numerical system is exactly the same as it is for the viscoelastic model in the next section, taking $\mu = 0$. Therefore we omit the derivation and numerical results for this model for now. As for the viscoelastic model, if μ is large enough, the damping causes the oscillations to disappear.

3.3. Viscoelastic model

In the former section, a purely elastic model was described. Due to the characteristic of the skin, incorporating viscosity is necessary.

3.3.1. Derivation

In the concept of viscosity, stress is proportionate with the strain rate, that is, the extent in which the strain changes in time:

$$\sigma = \mu \frac{\partial \varepsilon}{\partial t}(X,t) = \mu \frac{\mathrm{D}\varepsilon}{\mathrm{D}t}(x,t). \tag{3.3.1}$$

Here, μ is the viscosity coefficient, representing how viscous the fluid is. In the context of the skin, both pure elasticity and pure viscosity are not the best way to describe the behaviour of the material [18]. A better concept is viscoelasticity, which combines elasticity with viscosity, yielding:

$$\sigma = E_s \varepsilon + \mu \frac{\mathrm{D}\varepsilon}{\mathrm{D}t}, \tag{3.3.2}$$

which is called the Kelvin-Voigt model [16]. Now note that

$$\frac{\partial \varepsilon}{\partial t}(X,t) = \frac{\partial}{\partial t}\left(\frac{\partial u}{\partial X}\right) = \frac{\partial}{\partial X}\left(\frac{\partial u}{\partial t}(X,t)\right) = \frac{\partial v}{\partial X} = \frac{\partial v}{\partial x}\frac{\partial x}{\partial X}. \tag{3.3.3}$$

Assuming that the deformation is relatively small, that is

$$\frac{\partial x}{\partial X} \approx 1, \tag{3.3.4}$$

we can approximate

$$\sigma \approx E_s \varepsilon + \mu \frac{\partial v}{\partial x}. \tag{3.3.5}$$

Together with the Cauchy Momentum Equation, we obtain a viscoelastic model in one-dimension:

$$(IBVP_2): \begin{cases} \frac{\mathrm{D}(\rho v)}{\mathrm{D}t} + \rho v \frac{\partial v}{\partial x} = \frac{\partial \sigma}{\partial x} + f, & 0 < x < l(t), t > 0, \\ \sigma = E_s \varepsilon + \mu \frac{\partial v}{\partial x}, & 0 < x < l(t), t > 0, \\ \varepsilon = \frac{\partial u}{\partial x}, & 0 < x < l(t), t > 0, \\ v = \frac{\mathrm{D}u}{\mathrm{D}t}, & 0 < x < l(t), t > 0, \\ v(0,t) = 0, & t > 0, \\ \sigma(l(t),t) = 0, & t > 0, \\ u(x,0) = 0, & 0 \leq x \leq l(t), \\ v(x,0) = 0, & 0 \leq x \leq l(t). \end{cases}$$

This model can be viewed as an extension of the time-dependent elasticity model stated in $(IBVP_1)$.

3.3.2. Material derivative of linear basis functions

The following theorem reflects the fact that piecewise linear basis functions do not change in the Lagrangian framework as the mesh is moving. That is, the material derivative of the basis function is equal to 0. Suppose $\phi_i(x,t) = \phi_i(x(X,t),t) \in L^2(H^1(\Omega(t)),(0,T))$ is a Finite Element basis function that is piecewise linear on the elements at X and such that $\phi_i(x_j,t) = \delta_{ij}$, where

$$\delta_{ij} = \begin{cases} 1, & \text{if } i = j, \\ 0, & \text{if } i \neq j. \end{cases} \tag{3.3.6}$$

Then we have

$$\frac{\mathrm{D}\phi_i}{\mathrm{D}t}(x,t) = 0. \tag{3.3.7}$$

Proof. We have that

$$\frac{\mathrm{D}\phi_i}{\mathrm{D}t}(x_j,t) = \frac{\partial\phi_i}{\partial t}(X_j,t) = \lim_{\Delta t\to 0}\frac{\phi_i(X_j,t+\Delta t)-\phi_i(X_j,t)}{\Delta t} = \lim_{\Delta t\to 0}\frac{\delta_{ij}-\delta_{ij}}{\Delta t} = 0. \tag{3.3.8}$$

For any $x \in [x_k, x_{k+1}$, we can write

$$x = x(X,t) = x(\lambda_1 X_k + \lambda_2 X_{k+1}, t), \tag{3.3.9}$$

such that

$$\lambda_1 + \lambda_2 = 1. \tag{3.3.10}$$

Then it follows that

$$\frac{\mathrm{D}\phi_i}{\mathrm{D}t}(x,t) = \frac{\partial\phi_i}{\partial t}(\lambda_1 X_k + \lambda_2 X_{k+1}, t). \tag{3.3.11}$$

By the linearity of the time derivative, since ϕ_i is piecewise linear with respect to X, the time derivative $\frac{\partial\phi_i}{\partial t}(X,t)$ is piecewise linear as well. Hence, this time derivative function can be written as

$$\frac{\partial\phi_i}{\partial t}(X,t) = A(t) + B(t)X, \tag{3.3.12}$$

where $A(t)$ and $B(t)$ are constant with respect to X. Combining this with Equations (4.2.2), (4.2.4) and (4.2.5), it follows that

$$\begin{aligned} \frac{\mathrm{D}\phi_i}{\mathrm{D}t}(x,t) &= \frac{\partial\phi_i}{\partial t}(\lambda_1 X_k + \lambda_2 X_{k+1}, t) \\ &= A(t) + B(t)(\lambda_1 X_k + \lambda_2 X_{k+1}) \\ &= (\lambda_1+\lambda_2)A(t) + \lambda_1 B(t)X_k + \lambda_2 B(t)X_{k+1} \\ &= \lambda_1(A(t)+B(t)X_k) + \lambda_2(A(t)+B(t)X_{k+1}) \\ &= \lambda_1\frac{\mathrm{D}\phi_i}{\mathrm{D}t}(x_k,t) + \lambda_2\frac{\mathrm{D}\phi_i}{\mathrm{D}t}(x_{k+1},t) \\ &= 0. \end{aligned} \tag{3.3.13}$$

□

If we have a certain quantity $c(x,t)$, then by Theorem 3.3.2 and the Product Rule, we have

$$\frac{\mathrm{D}c}{\mathrm{D}t}\phi_i = \frac{\mathrm{D}\left(c\phi_i\right)}{\mathrm{D}t}, \tag{3.3.14}$$

which is used to derive the weak forms of the time-dependent models.

3.3.3. Finite-element approximations of the viscoelastic model

In the appendix, the Weak Form (W2) of $(IBVP_2)$ is derived, yielding:

$$(W2): \begin{cases} \text{Find } u \in L^2(H^1(\Omega(t)),(0,T)) \text{ with } u(x,0)=0 \text{ and } u(0,t)=0 \text{ such that} \\ \frac{\mathrm{d}}{\mathrm{d}t}\left(\int_0^{l(t)} \rho v\phi \,\mathrm{d}x\right) + \int_0^{l(t)} \mu \frac{\partial v}{\partial x}\frac{\partial \phi}{\partial x} + E_s \frac{\partial u}{\partial x}\frac{\partial \phi}{\partial x}\,\mathrm{d}x = \int_0^{l(t)} f\phi \,\mathrm{d}x, \\ \text{for all } \phi(x,t) \in H^1(\Omega(t)) \text{ with } \phi(0,t)=0 \text{ and } v(x,0)=0. \end{cases}$$

Euler Backward is used to approximate time integration. Furthermore, to obtain the Galerkin equations, we approximate v by

$$v(x,t) \approx v^n(x,t) := \sum_{j=0}^{n} v_j(t)\phi_j(x,t).$$

In addition, we select linear basis functions $\phi = \phi_i(x,t) := \alpha_i(t) + \beta_i(t)x$ such that $\phi_i(x_j) = \delta_{ij}$. This yields

$$\begin{aligned} & \rho \sum_{j=0}^{n} v_j^+ \int_0^{l(t+\Delta t)} \phi_i^+ \phi_j^+ \,\mathrm{d}x \\ + \quad & \Delta t\left(E_s \sum_{j=0}^{n} u_j^+ \int_0^{l(t+\Delta t)} \frac{\partial \phi_i^+}{\partial x}\frac{\partial \phi_j^+}{\partial x}\,\mathrm{d}x + \mu \sum_{j=0}^{n} v_j^+ \int_0^{l(t+\Delta t)} \frac{\partial \phi_i^+}{\partial x}\frac{\partial \phi_j^+}{\partial x}\,\mathrm{d}x\right) \\ = \quad & \rho \sum_{j=0}^{n} v_j \int_0^{l(t)} \phi_i \phi_j \,\mathrm{d}x + \Delta t \int_0^{l(t+\Delta t)} f^+ \phi_i^+ \,\mathrm{d}x. \end{aligned} \tag{3.3.15}$$

Here,

$$v_j^+ := v_j(t+\Delta t),\ u_j^+ := u_j(t+\Delta t),\ \phi_i^+ := \phi_i(x,t+\Delta t) \text{ and } f^+ := f(x,t+\Delta t),$$

and

$$v_j := v_j(t),\ u_j := u_j(t) \text{ and } \phi_i := \phi_i(x,t).$$

This yields a system

$$\left(\rho S_1^{k+1} + \Delta t \mu S_2^{k+1}\right)\mathbf{v}^{k+1} = \rho S_1^k \boldsymbol{v}^k - \Delta t E_s S_2^{k+1}\boldsymbol{u}^{k+1} + \Delta t \boldsymbol{f}^{k+1}. \tag{3.3.16}$$

Here, S_1 and S_2 are $(n+1)\times(n+1)$-matrices with corresponding element matrices

$$(S_1^k)_e = \frac{h_e^k}{6}\begin{pmatrix} 2 & 1 \\ 1 & 2 \end{pmatrix}, \tag{3.3.17}$$

$$(S_2^k)_e = \frac{1}{h_e^k}\begin{pmatrix} 1 & -1 \\ -1 & 1 \end{pmatrix}. \tag{3.3.18}$$

Furthermore,

$$\mathbf{v}^k := \left(v_0^k,\ldots,v_n^k\right)^T. \tag{3.3.19}$$

Since both $\boldsymbol{u}^{k+1}$ and $\boldsymbol{f}^{k+1}$ need to be known before computing $\boldsymbol{v}^{k+1}$, the following approximations are used:

$$x_i^{k+1} \approx x_i^k + \Delta t v_i^k, \tag{3.3.20}$$

$$u_i^{k+1} \approx u_i^k + \Delta t v_i^k. \tag{3.3.21}$$

3.4. Morphoelastic model

In Section 2.3, morphoelasticity was described as the main cause of wound contractures. Therefore, in this section we will derive a morphoelastic model.

3.4.1. Derivation

In Subsection 2.2.3, the mapping between the Eulerian and Lagrangian coordinates was already introduced. Subsequently, we introduce the deformation gradient F, which is defined as

$$F(X,t) := \frac{\partial x}{\partial X}(X,t). \tag{3.4.1}$$

This gradient represents the magnitude of the deformation. The deformation gradient can be divided into plastic deformation α and elastic deformation γ:

$$F(X,t) = \alpha(X,t)\gamma(X,t) \tag{3.4.2}$$

Initially, there is no plastic deformation or stress. Hence, the zero-stress state is the same as the initial state. If plastic deformation occurs, the tissue will not again retake its initial position when it is released from stress. As a consequence, the zero-stress state is no longer equal to the initial state. Hence, denoting the zero-stress state with z, we have:

$$\alpha(X,t) = \frac{\partial z}{\partial X}(X,t) \tag{3.4.3}$$

and

$$\gamma(X,t) = \frac{\partial x}{\partial z}(z(X,t),t). \tag{3.4.4}$$

Here, the zero-stress state can be viewed as a function of the initial state and time. Therefore, we have

$$F(X,t) = \frac{\partial x}{\partial X}(X,t) = \frac{\partial x}{\partial z}(z,t)\frac{\partial z}{\partial x}(X,t) = \alpha\gamma. \tag{3.4.5}$$

Figure 3.1 shows the relations between various states. The growth of the plastic deformation is defined as

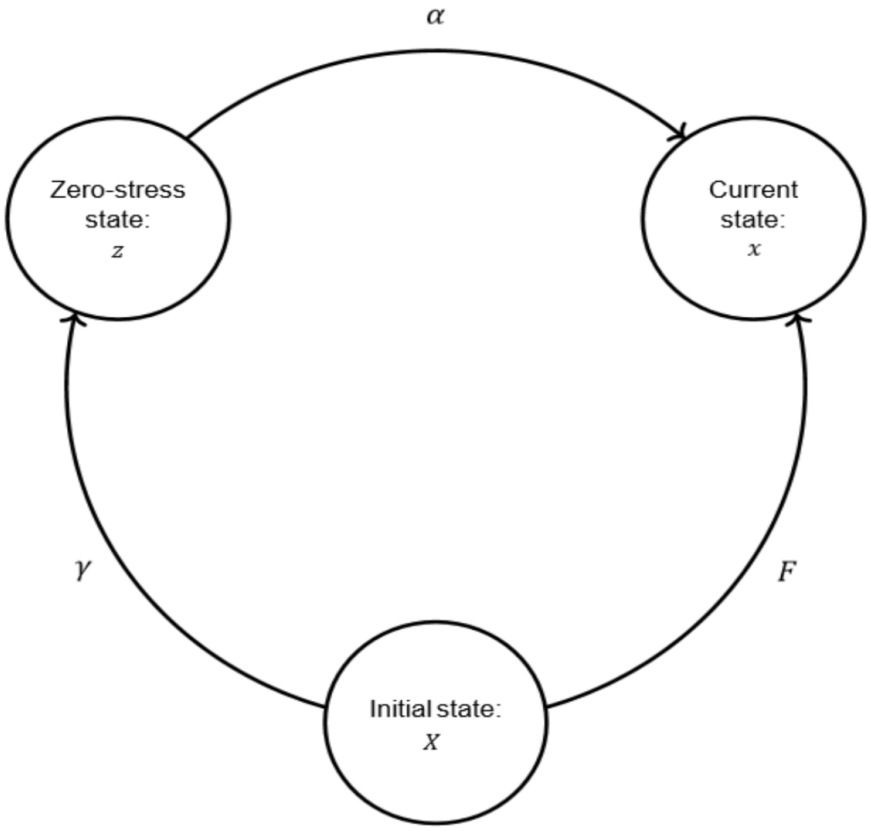

Figure 3.1: Relation between initial state, zero-stress state and current state. Source: [18] (Figure 4.7)

follows, written in Eulerian coordinates:

$$\frac{\mathrm{D}\gamma}{\mathrm{D}t}(x,t) = F(x,t)g(x,t), \tag{3.4.6}$$

where $g(x,t)$ represents the growth rate of the material. Since $\gamma = \alpha^{-1}F = F\alpha^{-1}$, Equation (3.4.6) results in

$$F\frac{\mathrm{D}\alpha^{-1}}{\mathrm{D}t} + \alpha^{-1}\frac{\mathrm{D}F}{\mathrm{D}t} = Fg, \tag{3.4.7}$$

$$\frac{\mathrm{D}\alpha^{-1}}{\mathrm{D}t} + F^{-1}\alpha^{-1}\frac{\mathrm{D}F}{\mathrm{D}t} = g. \tag{3.4.8}$$

Note that

$$F^{-1}\frac{\mathrm{D}F}{\mathrm{D}t} = \frac{\partial X}{\partial x}\frac{\mathrm{D}}{\mathrm{D}t}\left(\frac{\partial x}{\partial X}\right) = \frac{\partial X}{\partial x}\frac{\partial v}{\partial X} = \frac{\partial v}{\partial x}. \tag{3.4.9}$$

Here, we used that $F^{-1} = 1/(\partial x/\partial X) = \partial X/\partial x$, assuming $\partial x/\partial X \neq 0$. Furthermore, we used the Product Rule, which yields

$$\frac{\mathrm{D}}{\mathrm{D}t}\left(\frac{\partial x}{\partial X}(x,t)\right) = \frac{\partial}{\partial t}\left(\frac{\partial x}{\partial X}(X,t)\right) = \frac{\partial}{\partial X}\left(\frac{\partial x}{\partial t}(X,t)\right) = \frac{\partial v}{\partial X}. \tag{3.4.10}$$

Combining Equation (3.4.8) and (3.4.9), we obtain

$$\frac{\mathrm{D}\alpha^{-1}}{\mathrm{D}t} + \alpha^{-1}\frac{\partial v}{\partial x} = g. \tag{3.4.11}$$

We can express α^{-1} in terms of the strain. In Section 2.3.1, in the context of pure elasticity, (Eulerian) strain was defined as

$$\varepsilon = \frac{\partial u}{\partial x} = \frac{\partial(x - X(x,t))}{\partial x}. \tag{3.4.12}$$

However, note that if a permanent deformation has occured, such that we have zero-stress state z instead of X, it is more appropriate to use the following for the strain:

$$\varepsilon(x,t) := \frac{\partial(x-z)}{\partial x} = 1 - \frac{\partial z}{\partial x} = 1 - \frac{1}{\alpha} = 1 - \alpha^{-1}, \tag{3.4.13}$$

provided that $\alpha \neq 0$. Hence, $\alpha^{-1} = 1 - \varepsilon$ and Equation (3.4.11) results in

$$\frac{\mathrm{D}(1-\varepsilon)}{\mathrm{D}t} + (1-\varepsilon)\frac{\partial v}{\partial x} = g, \tag{3.4.14}$$

$$\frac{\mathrm{D}\varepsilon}{\mathrm{D}t} + (\varepsilon - 1)\frac{\partial v}{\partial x} = -g. \tag{3.4.15}$$

In [18], this equation is referred to as the Strain Evolution Equation. Therefore, a one-dimension morphoelastic model is given by

$$(IBVP_3): \begin{cases} \frac{\mathrm{D}(\rho v)}{\mathrm{D}t} + \rho v\frac{\partial v}{\partial x} = \frac{\partial \sigma}{\partial x} + f, & 0 < x < l(t), t > 0, \\ \frac{\mathrm{D}\varepsilon}{\mathrm{D}t} + (\varepsilon - 1)\frac{\partial v}{\partial x} = -g, & 0 < x < l(t), t > 0, \\ \sigma = E_s\varepsilon + \mu\frac{\partial v}{\partial x}, & 0 < x < l(t), t > 0, \\ v = \frac{\mathrm{D}u}{\mathrm{D}t}, & 0 < x < l(t), t > 0, \\ u(0,t) = 0, & t > 0, \\ v(0,t) = 0, & t > 0, \\ \sigma(l(t),t) = 0, & t > 0, \\ v(x,0) = 0, & 0 \leq x \leq l(t). \end{cases}$$

In [13], it is suggested that a suitable choice for g is

$$g(x,t) = \xi\varepsilon(x,t), \tag{3.4.16}$$

where ξ is a positive constant. This makes the rate of permanent deformation linearly dependent on the strain. In other words, the larger ξ, the larger the permanent deformation.

3.4.2. Finite-element approximations of the morphoelastic model

In this subsection, we will derive the finite-element approximations for the one-dimensional morphoelastic model ($IBVP_3$). We have already derived the weak form for the Cauchy Momentum Equation, which resulted in Equation (A.2.12). Note that in ($IBVP_3$), we are searching for solutions of v as well as ε. In this way, we obtain as a weak form

$$(W3_a): \begin{cases} \text{Find } v \in L^2(H^1(\Omega(t)),(0,T)) \text{ with } v(x,0)=0 \text{ and } v(0,t)=0 \text{ such that} \\ \frac{\mathrm{d}}{\mathrm{d}t}\left(\int_0^{l(t)} \rho v\phi \,\mathrm{d}x\right) + \int_0^{l(t)} \mu \frac{\partial v}{\partial x}\frac{\partial \phi}{\partial x} + E_s\varepsilon\frac{\partial \phi}{\partial x}\,\mathrm{d}x = \int_0^{l(t)} f\phi \,\mathrm{d}x, \\ \text{for all } \phi(x,t) \in H^1(\Omega(t)) \text{ with } \phi(0,t)=0. \end{cases}$$

To obtain the Galerkin equations, we approximate ε with

$$\varepsilon(x,t) \approx \varepsilon^n(x,t) := \sum_{j=0}^{n} \varepsilon_j(t)\phi_j(x,t).$$

Following the same assumptions and procedures as in former derivations,this yields

$$\begin{aligned} & \rho \sum_{j=0}^{n} v_j^+ \int_0^{l(t+\Delta t)} \phi_i^+\phi_j^+ \,\mathrm{d}x \\ + \quad & \Delta t\left(E_s \sum_{j=0}^{n} \varepsilon_j^+ \int_0^{l(t+\Delta t)} \frac{\partial \phi_i^+}{\partial x}\phi_j^+ \,\mathrm{d}x + \mu \sum_{j=0}^{n} v_j^+ \int_0^{l(t+\Delta t)} \frac{\partial \phi_i^+}{\partial x}\frac{\partial \phi_j^+}{\partial x}\,\mathrm{d}x\right) \\ = \quad & \rho \sum_{j=0}^{n} v_j \int_0^{l(t)} \phi_i\phi_j + \Delta t \int_0^{l(t+\Delta t)} f^+\phi_i^+ \,\mathrm{d}x. \end{aligned} \tag{3.4.17}$$

Here,

$$\varepsilon_j^+ := \varepsilon_j(t+\Delta t) \text{ and } \varepsilon_j := \varepsilon_j(t).$$

In the appendix, the Weak Form (W3$_b$) of the Strain Evolution Equation is derived, yielding:

$$(W3_b): \begin{cases} \text{Find } \varepsilon \in L^2(H^1(\Omega(t)),(0,T)) \text{ such that} \\ \frac{\mathrm{d}}{\mathrm{d}t}\left(\int_0^{l(t)} \varepsilon\psi \,\mathrm{d}x\right) - \int_0^{l(t)} \frac{\partial v}{\partial x}\psi \,\mathrm{d}x = -\int_0^{l(t)} g\psi \,\mathrm{d}x, \\ \text{for all } \psi(x,t) \in H^1(\Omega(t)). \end{cases}$$

Substituting $g = \xi\varepsilon$, as it was discussed in Subsection 3.4.1, we obtain

$$\frac{\mathrm{d}}{\mathrm{d}t}\left(\int_0^{l(t)} \varepsilon\psi \,\mathrm{d}x\right) + \int_0^{l(t)} \xi\varepsilon\psi - \frac{\partial v}{\partial x}\psi \,\mathrm{d}x \quad = \quad 0. \tag{3.4.18}$$

For the Strain Evolution Equation, time integration will work well for Euler Forward as well as for Euler Backward. We will derive the Galerkin equations for both methods, to compare the results for both methods. We again select linear basis functions, $\psi = \phi_i$. Starting with Euler Forward, we have

$$\sum_{j=0}^{n} \varepsilon_j^+ \int_0^{l(t+\Delta t)} \phi_i^+\phi_j^+ \,\mathrm{d}x = (1-\Delta t\xi)\sum_{j=0}^{n} \varepsilon_j \int_0^{l(t)} \phi_i\phi_j \,\mathrm{d}x + \Delta t \sum_{j=0}^{n} v_j \int_0^{l(t)} \phi_i \frac{\partial \phi_j}{\partial x}\,\mathrm{d}x. \tag{3.4.19}$$

Together with Equation (3.4.17), this yields two systems

$$\left(\rho S_1^{k+1} + \Delta t\mu S_2^{k+1}\right)\mathbf{v}^{k+1} + \Delta t E_s S_3^{k+1}\boldsymbol{\varepsilon}^{k+1} = \rho S_1^k \boldsymbol{v}^k + \Delta t \boldsymbol{f}^{k+1} \tag{3.4.20}$$

and

$$S_1^{k+1}\boldsymbol{\varepsilon}^{k+1} = (1-\Delta t\xi)\, S_1^k\boldsymbol{\varepsilon}^k + \Delta t S_4^k \mathbf{v}^k. \tag{3.4.21}$$

Here, S_3 and S_4 are $(n+1)\times(n+1)$-matrices with corresponding element matrices

$$(S_3^k)_e = \frac{1}{2}\begin{pmatrix}-1 & -1\\ 1 & 1\end{pmatrix}, \tag{3.4.22}$$

$$(S_4^k)_e = \frac{1}{2}\begin{pmatrix}-1 & 1\\ -1 & 1\end{pmatrix}, \tag{3.4.23}$$

Furthermore,

$$\boldsymbol{\varepsilon}^k := \left(\varepsilon_0^k,\ldots,\varepsilon_n^k\right)^T. \tag{3.4.24}$$

Alternatively, we can use the Euler Backward method in order to solve the strain evoluation equation. This yields, starting from Equation (A.3.8),

$$(1+\Delta t\xi)\sum_{j=0}^{n}\varepsilon_j^+\int_0^{l(t+\Delta t)}\phi_i^+\phi_j^+\,\mathrm{d}x=\sum_{j=0}^{n}\varepsilon_j\int_0^{l(t)}\phi_i\phi_j\,\mathrm{d}x+\Delta t\sum_{j=0}^{n}v_j\int_0^{l(t+\Delta t)}\phi_i^+\frac{\partial\phi_j^+}{\partial x}\,\mathrm{d}x, \tag{3.4.25}$$

that is,

$$(1+\Delta t\xi)S_1^{k+1}\boldsymbol{\varepsilon}^{k+1}=S_1^k\boldsymbol{\varepsilon}+\Delta tS_4^{k+1}\boldsymbol{v}^{k+1}. \tag{3.4.26}$$

Combined with Equation (3.4.17), we now obtain a system of $2(n+1)$ equations. Define

$$\boldsymbol{w}^k := (\varepsilon_0^k,\ldots,\varepsilon_n^k,v_0^k,\ldots,v_n^k)^T=\begin{pmatrix}\boldsymbol{\varepsilon}^k\\ \boldsymbol{v}^k\end{pmatrix},$$

then the system reads as

$$S^{k+1}\boldsymbol{w}^{k+1}=T^k\boldsymbol{w}^k+\Delta t\boldsymbol{\Phi}^{k+1}, \tag{3.4.27}$$

where

$$S^k := \begin{pmatrix}(1+\Delta t\xi)S_1^k & -\Delta tS_4^k\\ \Delta tE_sS_3^k & \rho S_1^k+\Delta t\mu S_2^k\end{pmatrix}, \tag{3.4.28}$$

$$T^k := \begin{pmatrix}S_1^k & 0\\ 0 & \rho S_1^k\end{pmatrix} \tag{3.4.29}$$

and

$$\boldsymbol{\Phi}^k := \begin{pmatrix}\mathbf{0}\\ \boldsymbol{f}^k\end{pmatrix}. \tag{3.4.30}$$

As can be seen, the 0's in the matrix T^k denote zero matrices of size $(n+1)\times(n+1)$ and the $\mathbf{0}$ in $\boldsymbol{f}^k$ denotes a zero vector of length $n-1$. In the next section, these two methods will be compared and we will mainly focus on the convergence.

3.5. Results

In this section, the results of the aforementioned models will be shown. In the first and second subsection, the details of the body force and overview of parameters are given. Then the time-independent model is considered and in the fourth subsection, the time-dependent models are treated.

3.5.1. Body force

In all the models, the body forces were for the utmost extent chosen in accordance with [18]. In the time-independent model, the body force function is given by:

$$f(x)=\begin{cases}\bar{f}, \text{ if } x\le\frac{L}{2},\\ -\bar{f}, \text{ if } x>\frac{L}{2},\end{cases} \tag{3.5.1}$$

where $\bar{f} \geq 0$ is viewed as a parameter that reflects the magnitude of the body force. To have a smooth force function against time, we define the time-dependent function

$$T(t) := \begin{cases} 1 - \exp\left(-C_f \cdot t/t_f\right), & \text{if } 0 \leq t < t_f, \\ \left(1 - \exp\left(-C_f \cdot t/t_f\right)\right) \exp\left(-\left(t - t_f\right)\right), & \text{if } t \geq t_f. \end{cases} \tag{3.5.2}$$

Here, $C_f \geq 0$ is a measure that is positively related to the maximal number of fibroblasts that enter the area. Furthermore, t_f denotes the time when the number of fibroblasts maximizes in the area. The body force function is then defined by

$$f(x,t) = \begin{cases} \bar{f} \cdot T(t), & \text{if } 0 \leq x \leq x\left(\frac{L}{2}, t\right), \\ -\bar{f} \cdot T(t), & \text{if } x > x\left(\frac{L}{2}, t\right). \end{cases} \tag{3.5.3}$$

Here, $x(\frac{L}{2}, t)$ denotes the x-position at time t with original position $X = \frac{L}{2}$, that is the middle of the tissue. Note that the body forces are equal to 0 initially and are increasing with time, until the moment that the maximum number of fibroblasts is reached. After that, the body forces decrease again.

3.5.2. Parameters

In Table 3.1, the chosen parameters are stated. In the column 'application', it is described in which models the parameter is used. It is important to point out that not all of the chosen values are calibrated to reality. We chose these values here to reproduce the results of [18] as far as possible.

Description	**Parameter**	**Value**	**Unit**	**Application**
Fibroblasts measure	C_f	4.0	-	all models
Duration of body force	t_f	20.0	day	all time-dependent models
Body Force	$\bar{f}$	5.0	$\mathrm{N{\cdot}g{\cdot}cell^{-1}{\cdot}cm^{-1}}$	all models
Elasticity (Young's modulus)	E_s	31.0	$\mathrm{N{\cdot}cm^{-2}}$	all models
Tissue length	L	10.0	cm	all models
Number of gridnodes	n	50	-	all models
Time step	Δt	0.02	day	all time-dependent models
General material density	ρ	1.02	$\mathrm{g{\cdot}cm^{-1}}$	visco- and morphoelastic model
Viscosity parameter	μ	100.0	$\mathrm{N{\cdot}day{\cdot}cm^{-1}}$	visco- and morphoelastic model
Rate of permanent deformation	ξ	0.05	-	morphoelastic model
Duration of simulated time	T	40.0	day	all models

Table 3.1: Overview of used parameters in the time-dependent one-dimensional models

3.5.3. One-dimensional time-independent purely elastic model

In this subsection, the results of the time-independent model (BVP) are presented. In Figures 3.2A and 3.2B, x and u are plotted as a function of the original coordinates X. In Figure 3.2A, the initial state is represented as well (blue dashed line). Hence, the graph in Figure 3.2B actually shows the difference between the two curves in Figure 3.2A.
The body force tries to contract the one-dimensional tissue towards the middle $X = 5$. Since there is a fixed boundary condition $u(0) = 0$, the actual displacement is larger at the right side of the middle than it is at the left side. This yields the behaviour as it is shown in Figure 3.2.

3.5.4. One-dimensional time-dependent models

In this subsection, results of the time-dependent models ($IBVP_1$), ($IBVP_2$) and ($IBVP_3$) are shown. The curves of x and u as a function of X at a certain moment in time, are more or less the same as the graphs in Figure 3.2. Therefore, we omit that here. However, since the models are time-dependent, the development

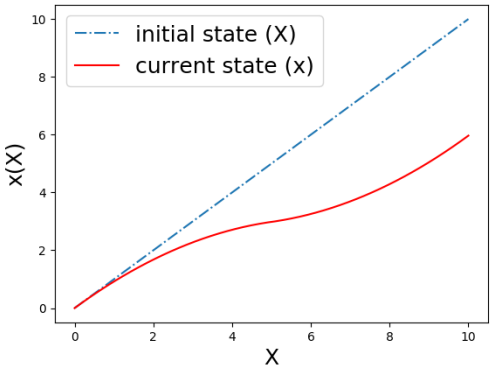

A. Plot of x as a function of X.

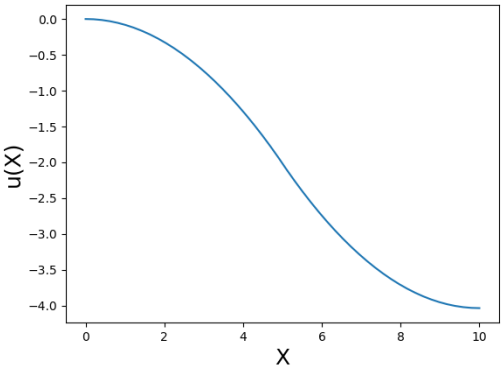

B. Plot of u as a function of X.

Figure 3.2: Equilibrium state in purely elastic model.

of the tissue length can be shown as a function of time and then the difference between the three models is clearly visible. (see Figure 3.3). The tissue length is defined as $l(t) := x(L,t)$: since the tissue does not move at $X = 0$, the length only depends of the position at $X = L$. The main differences between the several models can be seen in the figures. At $t = 20$, where the tissue starts to recover towards the initial state, the graph is much smoother in the viscoelastic model than in the purely elastic model. The other difference is that displacements are somewhat smaller than in the purely elastic model, which is mainly because the viscoelasticity causes a delay in the displacements. Therefore, the tissue starts to recover again while the displacement is not yet as large as in the purely elastic model. As for the morphoelastic model, a plastic deformation has occurred, which causes the tissue not to recover to the initial state. Therefore, for $\xi > 0$, the final length is smaller than the initial length, as opposed to the other models.

The one-dimensional morphoelastic model is less suitable for the case that the plastic deformation is very small, that is, if ξ is zero or close to zero. This can be explained as follows: the equation that is to be solved, is

$$\frac{\mathrm{D}\varepsilon}{\mathrm{D}t} + (\varepsilon - 1)\frac{\partial v}{\partial x} = -\xi\varepsilon. \tag{3.5.4}$$

This means,

$$\frac{\mathrm{D}\varepsilon}{\mathrm{D}t} - \frac{\partial v}{\partial x} = -\xi\varepsilon - \varepsilon\frac{\partial v}{\partial x} = -\left(\xi + \frac{\partial v}{\partial x}\right)\varepsilon. \tag{3.5.5}$$

Supposing $\xi = 0$, we have

$$\frac{\mathrm{D}\varepsilon}{\mathrm{D}t} = -\frac{\partial v}{\partial x}\varepsilon + \frac{\partial v}{\partial x}. \tag{3.5.6}$$

The problem $\varepsilon' = \lambda\varepsilon$ is unstable for $\lambda > 0$. Further, time integration with Euler Backward is unstable in this case, resulted from that the problem is ill-posed. However, this is the type of problem we have in Equation (3.5.6): if $\frac{\partial v}{\partial x} < 0$ while at the same time $\left|\frac{\partial v}{\partial x}\right|$ is not very large. This explains why Euler Backward yields bad results for large t when $\xi = 0$. When ξ is very small, as was the case in the above example, the problem occurs as well.

As an example, Figure 3.4 shows a plot of u at $t = 40$ and a plot of $l(t)$ for $\xi = 10^{-4}$ (the other parameters remain the same). Although the graph of the length is smooth, it can be seen that in the plot of the displacements, oscillations appear at the boundaries and in the middle.

3.5.5. Comparison between Euler Forward and Euler Backward in morphoelastic model

In Subsection 3.4.2, we have seen that there are two approaches to solve the morphoelastic model numerically. In the first method, Euler Forward is used to solve the Strain Evolution Equation, which yields two systems, stated in Equation (3.4.20) and (3.4.21). In the second method, Euler Backward is used, which yields one system, stated in Equation (3.4.27).

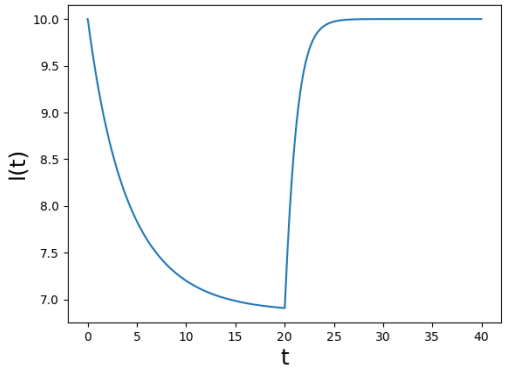

A. Elastic model

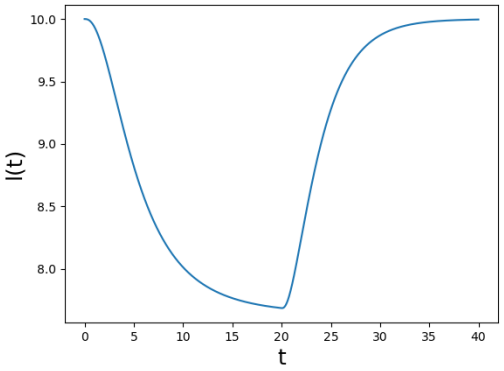

B. Viscoelastic model

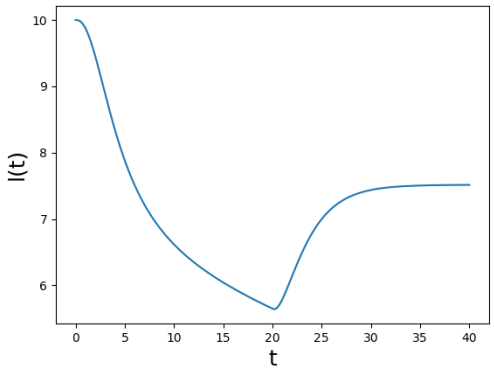

C. Morphoelastic model

Figure 3.3: Plots of tissue length as a function of t for different models

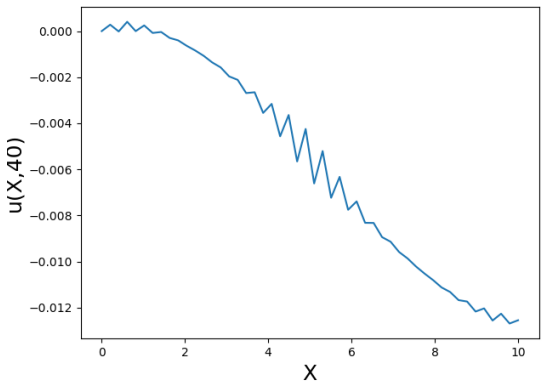

A. Plot of u as a function of X at $t = 40$

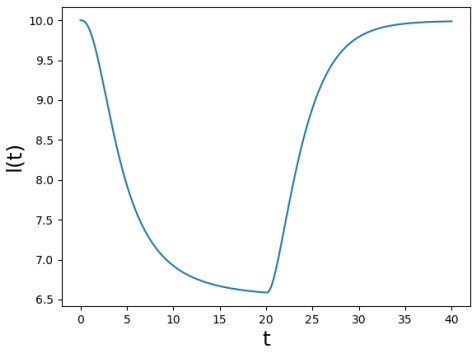

B. Plot of length as a function of t

Figure 3.4: Morphoelastic model with $\xi = 10^{-4}$

In order to consider the convergence of both methods, we define the following variable:

$$M_d := \max_{0\leq k\leq K} \max_{0\leq i\leq n} \left| u^1(x_i, t_k) - u^2(x_i, t_k) \right|, \tag{3.5.7}$$

where $u^1(x_i, t_k)$ and $u^2(x_i, t_k)$ are the displacements at x_i at iteration k, computed with the Euler Forward and Euler Backward method respectively. Hence, M_d reflects the maximum over time and location of the difference between the two methods. In Figure 3.5, a log-log plot of the value of M_d is shown as function of the time step dt. The total length of the simulations was $t = 40$ days and all parameters (except for the time step) were the same as in Table 3.2. It can be seen that the relationship between the maximal error and the time step is linear and

$$O(M_d) = O(\Delta t).$$

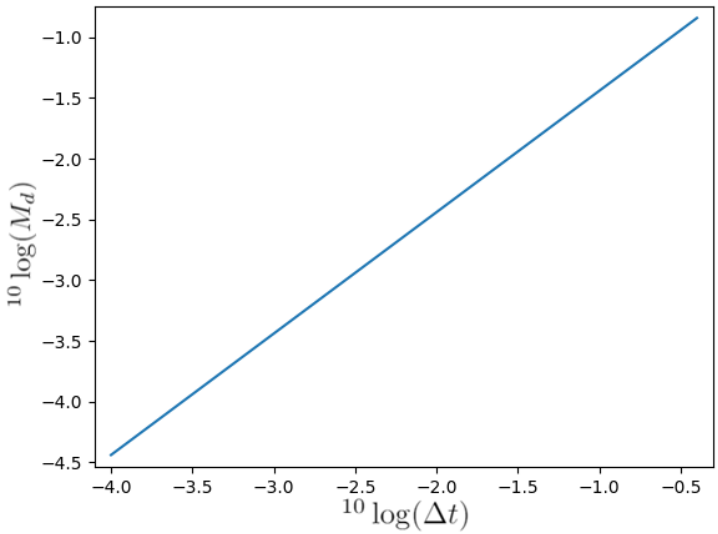

Figure 3.5: Log-log plot of M_d as function of time step

4

Two-Dimensional model of force balance with body force

In this chapter, we will generalize the models to the case of multi-dimensions. In the first section, the model derivation is done. The second section handles the numerical aspects and in the third section the results are presented. Since the computations for three dimensions are far more complex than for two dimensions, we mainly work on two-dimensional models in this manuscript.

4.1. Derivation

We will consider a purely elastic model, a viscoelastic model and a morphoelastic model.

4.1.1. Purely elastic model

In multi-dimensional models, several equations of the one-dimensional models need to be generalized. We use the Cauchy Momentum Equation in multi-dimensions Equation (3.1.14), Hooke's law in three dimensions (Equation (2.3.8)) and the definition of $\underline{\underline{\varepsilon}}$ in Equation (2.2.2), which yield:

$$(IBVP_4): \begin{cases} \frac{\mathrm{D}(\rho \boldsymbol{v})}{\mathrm{D}t} + \boldsymbol{v}\rho(\nabla \cdot \boldsymbol{v}) = \nabla \cdot \underline{\underline{\sigma}} + \boldsymbol{f}, & \boldsymbol{x} \in \Omega, t > 0, \\ \underline{\underline{\sigma}} = \frac{E_s\sqrt{\rho}}{1+\eta}\left(\underline{\underline{\varepsilon}} + \frac{\eta}{1-2\eta}\mathrm{Tr}(\underline{\underline{\varepsilon}})\mathrm{I}\right), & \boldsymbol{x} \in \Omega, t > 0, \\ \underline{\underline{\varepsilon}} = \frac{1}{2}\left(\nabla \boldsymbol{u} + (\nabla \boldsymbol{u})^T\right), & \boldsymbol{x} \in \Omega, t > 0, \\ \underline{\underline{\sigma}} \cdot \boldsymbol{n} + a\boldsymbol{u} = \boldsymbol{0}, & \boldsymbol{x} \in \partial\Omega, t > 0, \\ \boldsymbol{u}(\boldsymbol{x}, 0) = \boldsymbol{0}, & \boldsymbol{x} \in \Omega, \\ \boldsymbol{v}(\boldsymbol{x}, 0) = \boldsymbol{0}, & \boldsymbol{x} \in \Omega. \end{cases}$$

4.1.2. Viscoelastic model

At first we need to define the symmetric and skew part of a matrix. Let A be an $n \times n$-matrix. Then the symmetric part of A is an $n \times n$-matrix defined by

$$\mathrm{sym}\,(A) = \frac{1}{2}\left(A + A^T\right).$$

The skew part of A is an $n \times n$-matrix defined by

$$\mathrm{skew}\,(A) = \frac{1}{2}\left(A - A^T\right).$$

In the viscoelastic model, the stress tensor is extended with a viscoelastic part:

$$\underline{\underline{\sigma}} = \underline{\underline{\sigma}}_{\mathrm{visco}} + \underline{\underline{\sigma}}_{\mathrm{elas}}, \tag{4.1.1}$$

where $\underline{\underline{\sigma}}_{\text{elas}}$ is the elastic part of the stress tensor as defined in Hooke's law (Equation (2.3.8)) and used in Subsection 4.1.1. Furthermore, $\underline{\underline{\sigma}}_{\text{visco}}$ is the viscoelastic part of the stress tensor. It is defined as:

$$\underline{\underline{\sigma}}_{\text{visco}} = \mu \frac{\mathrm{D}\underline{\underline{\varepsilon}}}{\mathrm{D}t}. \tag{4.1.2}$$

According to [13], this can be written as:

$$\underline{\underline{\sigma}}_{\text{visco}} = \mu_1 \,\text{sym}\,(\nabla \boldsymbol{v}) + \mu_2 \text{Tr}\,(\nabla \boldsymbol{v})\,\underline{\underline{I}}, \tag{4.1.3}$$

where $\text{sym}\,(\nabla \boldsymbol{v}) := \frac{1}{2}\left(\nabla \boldsymbol{v} + \nabla \boldsymbol{v}^T\right)$ and μ_1 and μ_2 are the shear viscosity and bulk viscosity respectively. Hence, the stress tensor is given by:

$$\underline{\underline{\sigma}} = \mu_1 \,\text{sym}\,(\nabla \boldsymbol{v}) + \mu_2 \text{Tr}\,(\nabla \boldsymbol{v})\,\underline{\underline{I}} + \frac{E_s}{1+\eta}\left(\underline{\underline{\varepsilon}} + \frac{\eta}{1-2\eta}\text{Tr}(\underline{\underline{\varepsilon}})\underline{\underline{I}}\right).$$

Hence, the viscoelastic model is given by

$$(IBVP_5): \begin{cases} \frac{\mathrm{D}(\rho \boldsymbol{v})}{\mathrm{D}t} + \boldsymbol{v}\rho(\nabla \cdot \boldsymbol{v}) = \nabla \cdot \underline{\underline{\sigma}} + \boldsymbol{f}, & \boldsymbol{x} \in \Omega, t > 0, \\ \underline{\underline{\sigma}} = \mu_1 \text{sym}(\nabla \boldsymbol{v}) + \mu_2 \text{Tr}(\nabla \boldsymbol{v})\underline{\underline{I}} + \frac{E_s\sqrt{\rho}}{1+\eta}\left(\underline{\underline{\varepsilon}} + \frac{\eta}{1-2\eta}\text{Tr}(\underline{\underline{\varepsilon}})\underline{\underline{I}}\right), & \boldsymbol{x} \in \Omega, t > 0, \\ \underline{\underline{\varepsilon}} = \frac{1}{2}\left(\nabla \boldsymbol{u} + (\nabla \boldsymbol{u})^T\right), & \boldsymbol{x} \in \Omega, t > 0, \\ \underline{\underline{\sigma}} \cdot \boldsymbol{n} + a\boldsymbol{u} = \boldsymbol{0}, & \boldsymbol{x} \in \partial\Omega, t > 0, \\ \boldsymbol{u}(\boldsymbol{x}, 0) = \boldsymbol{0}, & \boldsymbol{x} \in \Omega, \\ \boldsymbol{v}(\boldsymbol{x}, 0) = \boldsymbol{0}, & \boldsymbol{x} \in \Omega. \end{cases}$$

4.1.3. Morphoelastic model

In the morphoelastic model in higher dimensions, we have a generalization of the Strain Evolution Equation (3.4.14). According to [10], the multi-dimensional Strain Evolution Equation reads:

$$\frac{\mathrm{D}\underline{\underline{\varepsilon}}}{\mathrm{D}t} + \underline{\underline{\varepsilon}}\,\text{skew}\left(\frac{\partial \boldsymbol{v}}{\partial \boldsymbol{x}}\right) - \text{skew}\left(\frac{\partial \boldsymbol{v}}{\partial \boldsymbol{x}}\right)\underline{\underline{\varepsilon}} + \left(\text{Tr}\left(\underline{\underline{\varepsilon}}\right) - 1\right)\text{sym}\left(\frac{\partial \boldsymbol{v}}{\partial \boldsymbol{x}}\right) = -\underline{\underline{g}}. \tag{4.1.4}$$

Hence, the full multi-dimensional morphoelastic model reads:

$$(IBVP_6): \begin{cases} \frac{\mathrm{D}(\rho \boldsymbol{v})}{\mathrm{D}t} + \boldsymbol{v}\rho(\nabla \cdot \boldsymbol{v}) = \nabla \cdot \underline{\underline{\sigma}} + \boldsymbol{f}, & \boldsymbol{x} \in \Omega, t > 0, \\ \underline{\underline{\sigma}} = \frac{\mu_1}{2}\left(\nabla \boldsymbol{v} + (\nabla \boldsymbol{v})^T\right) + \mu_2\left(\nabla \cdot \boldsymbol{v}\right)\underline{\underline{I}} + \frac{E_s\sqrt{\rho}}{1+\eta}\left(\underline{\underline{\varepsilon}} + \frac{\eta}{1-2\eta}\text{Tr}(\underline{\underline{\varepsilon}})\underline{\underline{I}}\right), & \boldsymbol{x} \in \Omega, t > 0, \\ \frac{\mathrm{D}\underline{\underline{\varepsilon}}}{\mathrm{D}t} + \underline{\underline{\varepsilon}}\,\text{skew}\left(\frac{\partial \boldsymbol{v}}{\partial \boldsymbol{x}}\right) - \text{skew}\left(\frac{\partial \boldsymbol{v}}{\partial \boldsymbol{x}}\right)\underline{\underline{\varepsilon}} + \left(\text{Tr}\left(\underline{\underline{\varepsilon}}\right) - 1\right)\text{sym}\left(\frac{\partial \boldsymbol{v}}{\partial \boldsymbol{x}}\right) = -\underline{\underline{g}}, & \boldsymbol{x} \in \Omega, t > 0, \\ \underline{\underline{\sigma}} \cdot \boldsymbol{n} + a\boldsymbol{u} = \boldsymbol{0}, & \boldsymbol{x} \in \partial\Omega, t > 0, \\ \boldsymbol{u}(\boldsymbol{x}, 0) = \boldsymbol{0}, & \boldsymbol{x} \in \Omega. \end{cases}$$

4.2. Numerical systems

In this section, we will derive the weak forms and the Galerkin equations for the models derived in Section 4.1. For the derivation of the weak forms, a generalization for multi-dimensions of Theorem 3.3.2 is used [4]. Let $\Omega(t) \in \mathbb{R}^n$ and $\phi_i(\boldsymbol{x}, t) = \phi_i(\boldsymbol{x}(\boldsymbol{X}, t), t) \in L^2(H^1(\Omega(t)), (0, T))$ is a Finite Element triangular basis function that is piecewise linear at $\boldsymbol{X}$, such that $\phi_i(\boldsymbol{x}_j, t) = \delta_{ij}$, where

$$\delta_{ij} = \begin{cases} 1, & \text{if } i = j, \\ 0, & \text{if } i \neq j. \end{cases}$$

Then we have

$$\frac{\mathrm{D}\phi_i}{\mathrm{D}t}(\boldsymbol{x},t)=0. \tag{4.2.1}$$

Proof. Similarly to the proof of Theorem 3.3.2, we have that

$$\frac{\mathrm{D}\phi_i}{\mathrm{D}t}(\boldsymbol{x}_j,t)=\frac{\partial\phi_i}{\partial t}(\boldsymbol{X}_j,t)=\lim_{\Delta t\to 0}\frac{\phi_i(\boldsymbol{X}_j,t+\Delta t)-\phi_i(\boldsymbol{X}_j,t)}{\Delta t}=\lim_{\Delta t\to 0}\frac{\delta_{ij}-\delta_{ij}}{\Delta t}=0. \tag{4.2.2}$$

Notice that for general $\boldsymbol{x}\in\Omega(t)$, we can write

$$\boldsymbol{x}=\boldsymbol{x}(\boldsymbol{X},t)=\boldsymbol{x}(\lambda_0\boldsymbol{X}_0+\ldots+\lambda_N\boldsymbol{X}_N,t), \tag{4.2.3}$$

such that

$$\sum_{j=0}^{N}\lambda_j=1. \tag{4.2.4}$$

Then it follows that

$$\frac{\mathrm{D}\phi_i}{\mathrm{D}t}(\boldsymbol{x},t)=\frac{\partial\phi_i}{\partial t}\left(\sum_{j=0}^{N}\lambda_j\boldsymbol{X}_j,t\right). \tag{4.2.5}$$

By definition of the time derivative, since ϕ_i is piecewise linear in $\boldsymbol{X}$, the time derivative $\frac{\partial\phi_i}{\partial t}(\boldsymbol{X},t)$ is piecewise linear as well. Hence, this time derivative function can be written as

$$\frac{\partial\phi_i}{\partial t}(\boldsymbol{X},t)=A_0(t)+A_1(t)X^1+\ldots+A_n(t)X^n, \tag{4.2.6}$$

where X^k denotes the k-th component of the vector $\boldsymbol{X}$. Combining this with Equations (4.2.2), (4.2.4) and (4.2.5), it follows that

$$\begin{aligned}
\frac{\mathrm{D}\phi_i}{\mathrm{D}t}(\boldsymbol{x},t) &= \frac{\partial\phi_i}{\partial t}\left(\sum_{j=0}^{N}\lambda_j\boldsymbol{X}_j,t\right)\\
&= A_0(t)+\sum_{k=1}^{n}\left(A_k(t)\cdot\left[\sum_{j=0}^{N}\lambda_j\boldsymbol{X}_j\right]^k\right)\\
&= \left(\sum_{j=0}^{N}\lambda_j\right)\cdot A_0(t)+\sum_{j=0}^{N}\left(\lambda_j\left[\sum_{k=1}^{n}A_k(t)X_j^k\right]\right)\\
&= \sum_{j=0}^{N}\left(\lambda_j\left[A_0(t)+\sum_{k=1}^{n}A_k(t)Xj^k\right]\right)\\
&= \sum_{j=0}^{N}\left(\lambda_j\frac{\mathrm{D}\phi_i}{\mathrm{D}t}(\boldsymbol{x}_j,t)\right)\\
&= 0.
\end{aligned}$$

□

4.2.1. Purely elastic model

In the appendix, the weak form (W4) of $(IBVP_4)$ is derived:

$$
(W4): \begin{cases} \text{Find } v_1, v_2 \in L^2(H^1(\Omega(t)),(0,T)), \text{ such that} \\ \rho \frac{\mathrm{d}}{\mathrm{d}t}\left(\int_{\Omega(t)} v_1\phi_1 \,\mathrm{d}\Omega\right) = \\ \quad -\frac{E_s\sqrt{\rho}}{1+\eta}\int_{\Omega(t)}\left(\frac{1-\eta}{1-2\eta}\frac{\partial u_1}{\partial x}+\frac{\eta}{1-2\eta}\frac{\partial u_2}{\partial y}\right)\frac{\partial \phi_1}{\partial x}+\frac{1}{2}\left(\frac{\partial u_1}{\partial y}+\frac{\partial u_2}{\partial x}\right)\frac{\partial \phi_1}{\partial y}\mathrm{d}\Omega \\ \quad +\int_{\Omega(t)} f_1\phi_1 \,\mathrm{d}\Omega - a\oint_{\partial\Omega(t)} u_1\phi_1 \,\mathrm{d}\Gamma, \\ \rho \frac{\mathrm{d}}{\mathrm{d}t}\left(\int_{\Omega(t)} v_2\phi_2 \,\mathrm{d}\Omega\right) = \\ \quad -\frac{E_s\sqrt{\rho}}{1+\eta}\int_{\Omega(t)}\frac{1}{2}\left(\frac{\partial u_1}{\partial y}+\frac{\partial u_2}{\partial x}\right)\frac{\partial \phi_2}{\partial x}+\left(\frac{\eta}{1-2\eta}\frac{\partial u_1}{\partial x}+\frac{1-\eta}{1-2\eta}\frac{\partial u_2}{\partial y}\right)\frac{\partial \phi_2}{\partial y}\mathrm{d}\Omega \\ \quad +\int_{\Omega(t)} f_2\phi_2 \,\mathrm{d}\Omega - a\oint_{\partial\Omega(t)} u_2\phi_2 \,\mathrm{d}\Gamma, \\ \text{for all } \phi_1(\boldsymbol{x},t), \phi_2(\boldsymbol{x},t) \in H^1(\Omega(t)). \end{cases}
$$

Defining $N := (n_x+1)\cdot(n_y+1)-1$ (which is the number of nodes in Ω minus one), this yields the following Galerkin equations:

$$
\begin{aligned}
\rho\sum_{j=0}^{N}(v_1)_j^+\int_{\Omega^+}\phi_i^+\phi_j^+ \,\mathrm{d}\Omega &= \rho\sum_{j=0}^{N}(v_1)_j\int_{\Omega(t)}\phi_i\phi_j \,\mathrm{d}\Omega \\
&+ \Delta t\frac{E_s\sqrt{\rho}}{1+\eta}\sum_{j=0}^{N}(u_1)_j^+\left(-\int_{\Omega^+}\frac{1-\eta}{1-2\eta}\frac{\partial\phi_i^+}{\partial x}\frac{\partial\phi_j^+}{\partial x}+\frac{1}{2}\frac{\partial\phi_i^+}{\partial y}\frac{\partial\phi_j^+}{\partial y}\mathrm{d}\Omega\right) \\
&+ \Delta t\frac{E_s\sqrt{\rho}}{1+\eta}\sum_{j=0}^{N}(u_2)_j^+\left(-\int_{\Omega^+}\frac{\eta}{1-2\eta}\frac{\partial\phi_i^+}{\partial x}\frac{\partial\phi_j^+}{\partial y}+\frac{1}{2}\frac{\partial\phi_i^+}{\partial y}\frac{\partial\phi_j^+}{\partial x}\mathrm{d}\Omega\right) \\
&+ \Delta t\int_{\Omega^+} f_1^+\phi_i^+ \,\mathrm{d}\Omega, \qquad (4.2.7)
\end{aligned}
$$

and

$$
\begin{aligned}
\rho\sum_{j=0}^{N}(v_2)_j^+\int_{\Omega^+}\phi_i^+\phi_j^+ \,\mathrm{d}\Omega &= \rho\sum_{j=0}^{N}(v_2)_j\int_{\Omega(t)}\phi_i\phi_j \,\mathrm{d}\Omega \\
&+ \Delta t\frac{E_s\sqrt{\rho}}{1+\eta}\sum_{j=0}^{N}(u_1)_j^+\left(-\int_{\Omega^+}\frac{1}{2}\frac{\partial\phi_i^+}{\partial x}\frac{\partial\phi_j^+}{\partial y}+\frac{\eta}{1-2\eta}\frac{\partial\phi_i^+}{\partial y}\frac{\partial\phi_j^+}{\partial x}\mathrm{d}\Omega\right) \\
&+ \Delta t\frac{E_s\sqrt{\rho}}{1+\eta}\sum_{j=0}^{N}(u_2)_j^+\left(-\int_{\Omega^+}\frac{1}{2}\frac{\partial\phi_i^+}{\partial x}\frac{\partial\phi_j^+}{\partial x}+\frac{1-\eta}{1-2\eta}\frac{\partial\phi_i^+}{\partial y}\frac{\partial\phi_j^+}{\partial y}\mathrm{d}\Omega\right) \\
&+ \Delta t\int_{\Omega^+} f_2^+\phi_i^+ \,\mathrm{d}\Omega. \qquad (4.2.8)
\end{aligned}
$$

Here, $\Omega^+ := \Omega(t+\Delta t)$. Furthermore, all variables with a superscript + should be evaluated at $t = t+\Delta t$. After deriving the Galerkin equations, we obtain the following numerical systems for the purely elastic model:

$$
\begin{aligned}
\left(\rho M_1^{k+1}+\Delta t^2 B^{k+1}\right)\boldsymbol{v}_1^{k+1} &= \rho M_1^k\boldsymbol{v}_1^k \\
&+ \Delta t\frac{E_s\sqrt{\rho}}{1+\eta}\left(\left(\frac{1-\eta}{1-2\eta}S_1^{k+1}+\frac{1}{2}S_2^{k+1}\right)\boldsymbol{u}_1^{k+1}+\left(\frac{\eta}{1-2\eta}S_3^{k+1}+\frac{1}{2}S_4^{k+1}\right)\boldsymbol{u}_2^{k+1}\right) \\
&+ \Delta t\boldsymbol{f}_1^{k+1} - a\cdot\Delta t\cdot\boldsymbol{b}_1^k, \qquad (4.2.9)
\end{aligned}
$$

and

$$
\begin{aligned}
\left(\rho M_1^{k+1}+\Delta t^2 B^{k+1}\right)\boldsymbol{v}_2^{k+1} &= \rho M_1^k\boldsymbol{v}_2^k \\
&+ \Delta t\frac{E_s\sqrt{\rho}}{1+\eta}\left(\left(\frac{\eta}{1-2\eta}S_4^{k+1}+\frac{1}{2}S_3^{k+1}\right)\boldsymbol{u}_1^{k+1}+\left(\frac{1-\eta}{1-2\eta}S_2^{k+1}+\frac{1}{2}S_1^{k+1}\right)\boldsymbol{u}_2^{k+1}\right) \\
&+ \Delta t\boldsymbol{f}_2^{k+1} - a\cdot\Delta t\cdot\boldsymbol{b}_2^k. \qquad (4.2.10)
\end{aligned}
$$

The matrices M_1^k,S_l^k ($l = 1,\dots 4$) and B^k, are $(N+1)\times(N+1)$-matrices and $\boldsymbol{f}_1^k$, $\boldsymbol{f}_2^k$, $\boldsymbol{b}_1^k$ and $\boldsymbol{b}_2^k$ vectors of length $N+1$ with the following (boundary) element matrices and element vector:

$$(M_1^k)_e = \frac{|\Delta|_e^k}{24}\begin{pmatrix}2&1&1\\1&2&1\\1&1&2\end{pmatrix}, \tag{4.2.11}$$

$$(S_1^k)_e = -\frac{|\Delta|_e^k}{2}\begin{pmatrix}\beta_1\beta_1&\beta_1\beta_2&\beta_1\beta_3\\\beta_2\beta_1&\beta_2\beta_2&\beta_2\beta_3\\\beta_3\beta_1&\beta_3\beta_2&\beta_3\beta_3\end{pmatrix}, \tag{4.2.12}$$

$$(S_2^k)_e = -\frac{|\Delta|_e^k}{2}\begin{pmatrix}\gamma_1\gamma_1&\gamma_1\gamma_2&\gamma_1\gamma_3\\\gamma_2\gamma_1&\gamma_2\gamma_2&\gamma_2\gamma_3\\\gamma_3\gamma_1&\gamma_3\gamma_2&\gamma_3\gamma_3\end{pmatrix}, \tag{4.2.13}$$

$$(S_3^k)_e = -\frac{|\Delta|_e^k}{2}\begin{pmatrix}\beta_1\gamma_1&\beta_1\gamma_2&\beta_1\gamma_3\\\beta_2\gamma_1&\beta_2\gamma_2&\beta_2\gamma_3\\\beta_3\gamma_1&\beta_3\gamma_2&\beta_3\gamma_3\end{pmatrix}, \tag{4.2.14}$$

$$(S_4^k)_e = -\frac{|\Delta|_e^k}{2}\begin{pmatrix}\gamma_1\beta_1&\gamma_1\beta_2&\gamma_1\beta_3\\\gamma_2\beta_1&\gamma_2\beta_2&\gamma_2\beta_3\\\gamma_3\beta_1&\gamma_3\beta_2&\gamma_3\beta_3\end{pmatrix}, \tag{4.2.15}$$

$$(B^k)_{be} = a\cdot\frac{||\boldsymbol{q}_2^k-\boldsymbol{q}_1^k||}{6}\begin{pmatrix}2&1\\1&2\end{pmatrix}, \tag{4.2.16}$$

$$(\boldsymbol{f}_d^k)_e = \frac{|\Delta|_e^k}{6}\begin{pmatrix}f_d(p_1^k,k\Delta t)\\f_d(p_2^k,k\Delta t)\\f_d(p_3^k,k\Delta t)\end{pmatrix}, \tag{4.2.17}$$

$$(\boldsymbol{b}_d^k)_{be} = \frac{||\boldsymbol{q}_2^{k+1}-\boldsymbol{q}_1^{k+1}||}{2}\begin{pmatrix}u_d(\boldsymbol{q}_1^k,k\Delta t)\\u_d(\boldsymbol{q}_2^k,k\Delta t)\end{pmatrix}, \tag{4.2.18}$$

where $|\Delta|_e^k$ denotes twice the area of the element $e = (p_1^k, p_2^k, p_3^k)$ at time step k and $||\boldsymbol{q}_2^k - \boldsymbol{q}_1^k||$ is the length of boundary element $be = [\boldsymbol{q}_1^k, \boldsymbol{q}_2^k]$ at time step k. For B^k, $\boldsymbol{b}_1^k$ and $\boldsymbol{b}_2^k$, only boundary element matrix and vectors are given, since this matrix and vector are related to the boundary condition. For internal elements, the element matrix of B^k is a zero matrix and the element vectors of $\boldsymbol{b}_d^k$ are zero vectors. Furthermore,

$$\beta_i := \beta_{p_i}, \qquad \gamma_i := \gamma_{p_i}, \qquad i \in \{1,2,3\},$$

and

$$\boldsymbol{v}_d^k := \left((v_d)_0^k,\dots,(v_d)_N^k\right)^T,\ \boldsymbol{u}_d^k := \left((u_d)_0^k,\dots,(u_d)_N^k\right)^T \text{ and } \boldsymbol{f}_d^k := \left((f_d)_0^k,\dots,(f_d)_N^k\right)^T,\ (d=1,2).$$

Same as in the one-dimensional case, $\boldsymbol{u}_d^{k+1}$ is approximated by:

$$\boldsymbol{u}_d^{k+1} \approx \boldsymbol{u}_d^k + \Delta t\,\boldsymbol{v}_d^k, \qquad d \in \{1,2\}. \tag{4.2.19}$$

4.2.2. Viscoelastic model

In the appendix, the weak form (W5) of ($IBVP_5$) is derived:

$$
(W5):\begin{cases}
\text{Find } v_1, v_2 \in L^2(H^1(\Omega(t)),(0,T)), \text{ such that} \\
\rho \frac{\mathrm{d}}{\mathrm{d}t}\left(\int_{\Omega(t)} v_1\phi_1 \,\mathrm{d}\Omega\right) = \\
\qquad \int_{\Omega(t)} -\frac{\mu_1}{2}\left(\frac{\partial v_1}{\partial y}+\frac{\partial v_2}{\partial x}\right)\frac{\partial \phi}{\partial x} - \left(\mu_2\frac{\partial v_1}{\partial x}+\left(\mu_1+\mu_2\right)\frac{\partial v_2}{\partial y}\right)\frac{\partial \phi}{\partial y}\mathrm{d}\Omega \\
\qquad -\frac{E_s\sqrt{\rho}}{1+\eta}\int_{\Omega(t)}\left(\frac{1-\eta}{1-2\eta}\frac{\partial u_1}{\partial x}+\frac{\eta}{1-2\eta}\frac{\partial u_2}{\partial y}\right)\frac{\partial \phi_1}{\partial x}+\frac{1}{2}\left(\frac{\partial u_1}{\partial y}+\frac{\partial u_2}{\partial x}\right)\frac{\partial \phi_1}{\partial y}\mathrm{d}\Omega \\
\qquad +\int_{\Omega(t)} f_1\phi_1 \,\mathrm{d}\Omega - a\oint_{\partial\Omega(t)} u_1\phi_1 \,\mathrm{d}\Gamma, \\
\rho \frac{\mathrm{d}}{\mathrm{d}t}\left(\int_{\Omega(t)} v_2\phi_2 \,\mathrm{d}\Omega\right) = \\
\qquad \int_{\Omega(t)} -\frac{\mu_1}{2}\left(\frac{\partial v_1}{\partial y}+\frac{\partial v_2}{\partial x}\right)\frac{\partial \phi}{\partial x} - \left(\mu_2\frac{\partial v_1}{\partial x}+\left(\mu_1+\mu_2\right)\frac{\partial v_2}{\partial y}\right)\frac{\partial \phi}{\partial y}\mathrm{d}\Omega \\
\qquad -\frac{E_s\sqrt{\rho}}{1+\eta}\int_{\Omega(t)}\frac{1}{2}\left(\frac{\partial u_1}{\partial y}+\frac{\partial u_2}{\partial x}\right)\frac{\partial \phi_2}{\partial x}+\left(\frac{\eta}{1-2\eta}\frac{\partial u_1}{\partial x}+\frac{1-\eta}{1-2\eta}\frac{\partial u_2}{\partial y}\right)\frac{\partial \phi_2}{\partial y}\mathrm{d}\Omega \\
\qquad +\int_{\Omega(t)} f_2\phi_2 \,\mathrm{d}\Omega - a\oint_{\partial\Omega(t)} u_2\phi_2 \,\mathrm{d}\Gamma, \\
\text{for all } \phi_1(\boldsymbol{x},t), \phi_2(\boldsymbol{x},t) \in H^1(\Omega(t)).
\end{cases}
$$

This means that Equation (4.2.9) becomes:

$$
\begin{aligned}
\left(\rho M_1^{k+1}+\Delta t^2 B^{k+1}\right)\boldsymbol{v}_1^{k+1} &= \rho M_1^k \boldsymbol{v}_1^k \\
&+ \Delta t\frac{E_s\sqrt{\rho}}{1+\eta}\left(\left(\frac{1-\eta}{1-2\eta}S_1^{k+1}+\frac{1}{2}S_2^{k+1}\right)\boldsymbol{u}_1^{k+1}+\left(\frac{\eta}{1-2\eta}S_3^{k+1}+\frac{1}{2}S_4^{k+1}\right)\boldsymbol{u}_2^{k+1}\right) \\
&+ \Delta t\left(\left(\left(\mu_1+\mu_2\right)S_1^{k+1}+\frac{\mu_1}{2}S_2^{k+1}\right)\boldsymbol{v}_1^{k+1}+\left(\mu_2 S_3^{k+1}+\frac{\mu_1}{2}S_4^{k+1}\right)\boldsymbol{v}_2^{k+1}\right) \\
&+ \Delta t\boldsymbol{f}_1^{k+1} - a\cdot\Delta t\cdot\boldsymbol{b}_1^k, \qquad (4.2.20)
\end{aligned}
$$

and Equation (4.2.10) becomes:

$$
\begin{aligned}
\left(\rho M_1^{k+1}+\Delta t^2 B^{k+1}\right)\boldsymbol{v}_2^{k+1} &= \rho M_1^k \boldsymbol{v}_2^k \\
&+ \Delta t\frac{E_s\sqrt{\rho}}{1+\eta}\left(\left(\frac{\eta}{1-2\eta}S_4^{k+1}+\frac{1}{2}S_3^{k+1}\right)\boldsymbol{u}_1^{k+1}+\left(\frac{1-\eta}{1-2\eta}S_2^{k+1}+\frac{1}{2}S_1^{k+1}\right)\boldsymbol{u}_2^{k+1}\right) \\
&+ \Delta t\left(\left(\frac{\mu_1}{2}S_3^{k+1}+\mu_2 S_4^{k+1}\right)\boldsymbol{v}_1^{k+1}+\left(\frac{\mu_1}{2}S_1^{k+1}+\left(\mu_1+\mu_2\right)S_2^{k+1}\right)\boldsymbol{v}_2^{k+1}\right) \\
&+ \Delta t\boldsymbol{f}_2^{k+1} - a\cdot\Delta t\cdot\boldsymbol{b}_2^k. \qquad (4.2.21)
\end{aligned}
$$

4.2.3. Morphoelastic model

In the morphoelastic model, the Strain Evolution Equations are included:

$$
\begin{cases}
\frac{\mathrm{D}\varepsilon_{11}}{\mathrm{D}t}+\varepsilon_{11}\nabla\cdot\boldsymbol{v} = & \left(1-\varepsilon_{22}\right)\frac{\partial v_1}{\partial x}+\varepsilon_{11}\frac{\partial v_2}{\partial y}+\frac{1}{2}\left(\varepsilon_{21}+\varepsilon_{12}\right)\left(\frac{\partial v_1}{\partial y}-\frac{\partial v_2}{\partial x}\right)-g_{11}, \\
\frac{\mathrm{D}\varepsilon_{12}}{\mathrm{D}t}+\varepsilon_{12}\nabla\cdot\boldsymbol{v} = & \varepsilon_{12}\nabla\cdot\boldsymbol{v}+\frac{1}{2}\left(\left(1-2\varepsilon_{11}\right)\frac{\partial v_1}{\partial y}+\left(1-2\varepsilon_{22}\right)\frac{\partial v_2}{\partial x}\right)-g_{12},\ \varepsilon_{21}=\varepsilon_{12}, \\
\frac{\mathrm{D}\varepsilon_{22}}{\mathrm{D}t}+\varepsilon_{22}\nabla\cdot\boldsymbol{v} = & \left(1-\varepsilon_{11}\right)\frac{\partial v_2}{\partial y}+\varepsilon_{22}\frac{\partial v_1}{\partial x}-\frac{1}{2}\left(\varepsilon_{12}+\varepsilon_{21}\right)\left(\frac{\partial v_1}{\partial y}-\frac{\partial v_2}{\partial x}\right)-g_{22}.
\end{cases}
$$

Hence, we seek the solutions to both $\boldsymbol{v}$ and $\underline{\underline{\varepsilon}}$. The viscoelastic systems in Equation (4.2.20) and (4.2.21) become:

$$
\begin{aligned}
\rho M_1^{k+1}\boldsymbol{v}_1^{k+1} = \rho M_1^k\boldsymbol{v}_1^k &+ \Delta t\frac{E_s\sqrt{\rho}}{1+\eta}\left(\frac{1-\eta}{1-2\eta}P_1^{k+1}\boldsymbol{\varepsilon}_{11}^{k+1}+P_2^{k+1}\boldsymbol{\varepsilon}_{12}^{k+1}+\frac{\eta}{1-2\eta}P_1^{k+1}\boldsymbol{\varepsilon}_{22}^{k+1}\right) \\
&+ \Delta t\left(\left(\left(\mu_1+\mu_2\right)S_1^{k+1}+\frac{\mu_1}{2}S_2^{k+1}\right)\boldsymbol{v}_1^{k+1}+\left(\mu_2 S_3^{k+1}+\frac{\mu_1}{2}S_4^{k+1}\right)\boldsymbol{v}_2^{k+1}\right) \qquad (4.2.22) \\
&+ \Delta t\boldsymbol{f}_1^{k+1} - a\cdot\Delta t\cdot\boldsymbol{b}_1^k, \qquad (4.2.23)
\end{aligned}
$$

and

$$\begin{aligned}\rho M_1^{k+1}\boldsymbol{v}_2^{k+1} = \rho M_1^k \boldsymbol{v}_2^k \quad &+ \quad \Delta t \frac{E_s\sqrt{\rho}}{1+\eta}\left(\frac{\eta}{1-2\eta}P_2^{k+1}\boldsymbol{\varepsilon}_{11}^{k+1} + P_1^{k+1}\boldsymbol{\varepsilon}_{12}^{k+1} + \frac{1-\eta}{1-2\eta}P_2^{k+1}\boldsymbol{\varepsilon}_{22}^{k+1}\right) \\ &+ \quad \Delta t\left(\left(\frac{\mu_1}{2}S_3^{k+1} + \mu_2 S_4^{k+1}\right)\boldsymbol{v}_1^{k+1} + \left(\frac{\mu_1}{2}S_1^{k+1} + (\mu_1+\mu_2)S_2^{k+1}\right)\boldsymbol{v}_2^{k+1}\right) \quad (4.2.24) \\ &+ \quad \Delta t \boldsymbol{f}_2^{k+1} - a\cdot\Delta t\cdot\boldsymbol{b}_2^k. \quad (4.2.25)\end{aligned}$$

Here, P_1^k and P_2^k are $(N+1)\times(N+1)$-matrices with corresponding element matrices:

$$(P_1^k)_e = -\frac{|\Delta|_e^k}{6}\begin{pmatrix}\beta_1 & \beta_1 & \beta_1\\ \beta_2 & \beta_2 & \beta_2\\ \beta_3 & \beta_3 & \beta_3\end{pmatrix}, \quad (4.2.26)$$

$$(P_2^k)_e = -\frac{|\Delta|_e^k}{6}\begin{pmatrix}\gamma_1 & \gamma_1 & \gamma_1\\ \gamma_2 & \gamma_2 & \gamma_2\\ \gamma_3 & \gamma_3 & \gamma_3\end{pmatrix}. \quad (4.2.27)$$

In the appendix, the weak form (W6) of the Strain Evolution Equations is derived, yielding:

$$(W6): \begin{cases}\text{Find } \varepsilon_{11},\varepsilon_{12},\varepsilon_{22}\in L^2(H^1(\Omega(t)),(0,T)), \text{ such that}\\ \frac{\mathrm{d}}{\mathrm{d}t}\left(\int_{\Omega(t)}\varepsilon_{11}\phi_1\,\mathrm{d}\Omega\right) =\\ \qquad \int_{\Omega(t)}\left((1-\varepsilon_{22})\frac{\partial v_1}{\partial x} + \varepsilon_{11}\frac{\partial v_2}{\partial y} + \frac{1}{2}(\varepsilon_{21}+\varepsilon_{12})\left(\frac{\partial v_1}{\partial y}-\frac{\partial v_2}{\partial x}\right) - g_{11}\right)\phi_1\,\mathrm{d}\Omega,\\ \frac{\mathrm{d}}{\mathrm{d}t}\left(\int_{\Omega(t)}\varepsilon_{12}\phi_2\,\mathrm{d}\Omega\right) =\\ \qquad \int_{\Omega(t)}\left(\varepsilon_{12}\nabla\cdot\boldsymbol{v} + \frac{1}{2}\left((1-2\varepsilon_{11})\frac{\partial v_1}{\partial y} + (1-2\varepsilon_{22})\frac{\partial v_2}{\partial x}\right) - g_{12}\right)\phi_2\,\mathrm{d}\Omega,\\ \frac{\mathrm{d}}{\mathrm{d}t}\left(\int_{\Omega(t)}\varepsilon_{22}\phi_3\,\mathrm{d}\Omega\right) =\\ \qquad \int_{\Omega(t)}\left((1-\varepsilon_{11})\frac{\partial v_2}{\partial y} + \varepsilon_{22}\frac{\partial v_1}{\partial x} - \frac{1}{2}(\varepsilon_{12}+\varepsilon_{21})\left(\frac{\partial v_1}{\partial y}-\frac{\partial v_2}{\partial x}\right) - g_{22}\right)\phi_3\,\mathrm{d}\Omega,\\ \text{for all } \phi_1(\boldsymbol{x},t),\phi_2(\boldsymbol{x},t)\in H^1(\Omega(t)).\end{cases}$$

Deriving the Galerkin Equations and applying Euler Backward result in a non-linear system:

$$\begin{cases}(1+\xi\Delta t)M_1^{k+1}\boldsymbol{\varepsilon}_{11}^{k+1} = & M_1^k\boldsymbol{\varepsilon}_{11}^k + \Delta t T_1^{k+1}\boldsymbol{v}_1^{k+1} + \Delta t\boldsymbol{f}_{\varepsilon_{11}}^{k+1}(\boldsymbol{w}^{k+1}),\\ (1+\xi\Delta t)M_1^{k+1}\boldsymbol{\varepsilon}_{12}^{k+1} = & M_1^k\boldsymbol{\varepsilon}_{12}^k + \frac{\Delta t}{2}\left(T_2^{k+1}\boldsymbol{v}_1^{k+1} + T_1^{k+1}\boldsymbol{v}_2^{k+1}\right) + \Delta t\boldsymbol{f}_{\varepsilon_{12}}^{k+1}(\boldsymbol{w}^{k+1}),\\ (1+\xi\Delta t)M_1^{k+1}\boldsymbol{\varepsilon}_{22}^{k+1} = & M_1^k\boldsymbol{\varepsilon}_{22}^k + \Delta t T_2^{k+1}\boldsymbol{v}_2^{k+1} + \Delta t\boldsymbol{f}_{\varepsilon_{22}}^{k+1}(\boldsymbol{w}^{k+1}).\end{cases} \quad (4.2.28)$$

Here, T_1 and T_2 are $(N+1)\times(N+1)$-matrices, with the following element matrices:

$$(T_1^k)_e = \frac{|\Delta|_e^k}{6}\begin{pmatrix}\beta_1 & \beta_2 & \beta_3\\ \beta_1 & \beta_2 & \beta_3\\ \beta_1 & \beta_2 & \beta_3\end{pmatrix}, \quad (4.2.29)$$

$$(T_2^k)_e = \frac{|\Delta|_e^k}{6}\begin{pmatrix}\gamma_1 & \gamma_2 & \gamma_3\\ \gamma_1 & \gamma_2 & \gamma_3\\ \gamma_1 & \gamma_2 & \gamma_3\end{pmatrix}. \quad (4.2.30)$$

Furthermore,

$$\boldsymbol{\varepsilon}_{d_1d_2}^k := \left((\varepsilon_{d_1d_2})_0^k,\ldots,(\varepsilon_{d_1d_2})_N^k\right)^T, \qquad d_1,d_2\in\{1,2\},$$

and

$$\boldsymbol{w}^k := (\boldsymbol{\varepsilon}_{11}^k,\boldsymbol{\varepsilon}_{12}^k,\boldsymbol{\varepsilon}_{22}^k,\boldsymbol{v}_1^k,\boldsymbol{v}_2^k)^T.$$

Note that $\boldsymbol{f}_{\varepsilon_{11}}^{k+1}$, $\boldsymbol{f}_{\varepsilon_{12}}^{k+1}$ and $\boldsymbol{f}_{\varepsilon_{22}}^{k+1}$ are vector-valued functions of $\boldsymbol{w}^k$ with length $N+1$. The element vectors are defined by

$$(\boldsymbol{f}_{\varepsilon_{11}}^k(\boldsymbol{w}^k))_e := \frac{|\Delta|_e^k}{24}\begin{pmatrix}-\left[\boldsymbol{\beta}_e\cdot(\boldsymbol{v}_1)_e\right]\bar{\boldsymbol{\varepsilon}}_{22}^1 + \left[\boldsymbol{\gamma}_e\cdot(\boldsymbol{v}_2)_e\right]\bar{\boldsymbol{\varepsilon}}_{11}^1 + \left[\boldsymbol{\gamma}_e\cdot(\boldsymbol{v}_1)_e - \boldsymbol{\beta}_e\cdot(\boldsymbol{v}_2)_e\right]\bar{\boldsymbol{\varepsilon}}_{12}^1\\ -\left[\boldsymbol{\beta}_e\cdot(\boldsymbol{v}_1)_e\right]\bar{\boldsymbol{\varepsilon}}_{22}^2 + \left[\boldsymbol{\gamma}_e\cdot(\boldsymbol{v}_2)_e\right]\bar{\boldsymbol{\varepsilon}}_{11}^2 + \left[\boldsymbol{\gamma}_e\cdot(\boldsymbol{v}_1)_e - \boldsymbol{\beta}_e\cdot(\boldsymbol{v}_2)_e\right]\bar{\boldsymbol{\varepsilon}}_{12}^2\\ -\left[\boldsymbol{\beta}_e\cdot(\boldsymbol{v}_1)_e\right]\bar{\boldsymbol{\varepsilon}}_{22}^3 + \left[\boldsymbol{\gamma}_e\cdot(\boldsymbol{v}_2)_e\right]\bar{\boldsymbol{\varepsilon}}_{11}^3 + \left[\boldsymbol{\gamma}_e\cdot(\boldsymbol{v}_1)_e - \boldsymbol{\beta}_e\cdot(\boldsymbol{v}_2)_e\right]\bar{\boldsymbol{\varepsilon}}_{12}^3\end{pmatrix}, \quad (4.2.31)$$

$$(\boldsymbol{f}^k_{\varepsilon_{12}}(\boldsymbol{w}^k))_e := \frac{|\Delta|^k_e}{24}\begin{pmatrix}[\boldsymbol{\beta}_e\cdot(\boldsymbol{v}_1)_e+\boldsymbol{\gamma}_e\cdot(\boldsymbol{v}_2)_e]\bar{\boldsymbol{\varepsilon}}^1_{12}-[\boldsymbol{\gamma}_e\cdot(\boldsymbol{v}_1)_e]\bar{\boldsymbol{\varepsilon}}^1_{11}-[\boldsymbol{\beta}_e\cdot(\boldsymbol{v}_2)_e]\bar{\boldsymbol{\varepsilon}}^1_{22}\\ [\boldsymbol{\beta}_e\cdot(\boldsymbol{v}_1)_e+\boldsymbol{\gamma}_e\cdot(\boldsymbol{v}_2)_e]\bar{\boldsymbol{\varepsilon}}^2_{12}-[\boldsymbol{\gamma}_e\cdot(\boldsymbol{v}_1)_e]\bar{\boldsymbol{\varepsilon}}^2_{11}-[\boldsymbol{\beta}_e\cdot(\boldsymbol{v}_2)_e]\bar{\boldsymbol{\varepsilon}}^2_{22}\\ [\boldsymbol{\beta}_e\cdot(\boldsymbol{v}_1)_e+\boldsymbol{\gamma}_e\cdot(\boldsymbol{v}_2)_e]\bar{\boldsymbol{\varepsilon}}^3_{12}-[\boldsymbol{\gamma}_e\cdot(\boldsymbol{v}_1)_e]\bar{\boldsymbol{\varepsilon}}^3_{11}-[\boldsymbol{\beta}_e\cdot(\boldsymbol{v}_2)_e]\bar{\boldsymbol{\varepsilon}}^3_{22}\end{pmatrix}, \tag{4.2.32}$$

and

$$(\boldsymbol{f}^k_{\varepsilon_{22}}(\boldsymbol{w}^k))_e := \frac{|\Delta|^k_e}{24}\begin{pmatrix}-[\boldsymbol{\gamma}_e\cdot(\boldsymbol{v}_2)_e]\bar{\boldsymbol{\varepsilon}}^1_{11}+[\boldsymbol{\beta}_e\cdot(\boldsymbol{v}_1)_e]\bar{\boldsymbol{\varepsilon}}^1_{22}+[\boldsymbol{\gamma}_e\cdot(\boldsymbol{v}_1)_e-\boldsymbol{\beta}_e\cdot(\boldsymbol{v}_2)_e]\bar{\boldsymbol{\varepsilon}}^1_{12}\\ -[\boldsymbol{\gamma}_e\cdot(\boldsymbol{v}_2)_e]\bar{\boldsymbol{\varepsilon}}^2_{11}+[\boldsymbol{\beta}_e\cdot(\boldsymbol{v}_1)_e]\bar{\boldsymbol{\varepsilon}}^2_{22}+[\boldsymbol{\gamma}_e\cdot(\boldsymbol{v}_1)_e-\boldsymbol{\beta}_e\cdot(\boldsymbol{v}_2)_e]\bar{\boldsymbol{\varepsilon}}^2_{12}\\ -[\boldsymbol{\gamma}_e\cdot(\boldsymbol{v}_2)_e]\bar{\boldsymbol{\varepsilon}}^3_{11}+[\boldsymbol{\beta}_e\cdot(\boldsymbol{v}_1)_e]\bar{\boldsymbol{\varepsilon}}^3_{22}+[\boldsymbol{\gamma}_e\cdot(\boldsymbol{v}_1)_e-\boldsymbol{\beta}_e\cdot(\boldsymbol{v}_2)_e]\bar{\boldsymbol{\varepsilon}}^3_{12}\end{pmatrix}. \tag{4.2.33}$$

Here,

$$\boldsymbol{\beta}_e := (\beta_{p1},\beta_{p2},\beta_{p3})^T, \qquad \boldsymbol{\gamma}_e := (\gamma_{p1},\gamma_{p2},\gamma_{p3})^T.$$

Furthermore,

$$(\boldsymbol{v}_d)_e := ((v_d)_{p_1},(v_d)_{p_2},(v_d)_{p_3})^T$$

and

$$\bar{\boldsymbol{\varepsilon}}^i_{d_1d_2} := (\varepsilon_{d_1d_2})_{p_1}+(\varepsilon_{d_1d_2})_{p_2}+(\varepsilon_{d_1d_2})_{p_3}+(\varepsilon_{d_1d_2})_{p_i}.$$

Combining Equations (4.2.23), (4.2.25) and (4.2.28) together in one single system, we obtain:

$$\overline{M}^{k+1}\boldsymbol{w}^{k+1} = M^k\boldsymbol{w}^k + \Delta t S^{k+1}\boldsymbol{w}^{k+1} + \Delta t\boldsymbol{f}^{k+1}(\boldsymbol{w}^{k+1}), \tag{4.2.34}$$

where

$$\overline{M}^k := \begin{pmatrix}(1+\xi\Delta t)M^k_1 & \mathrm{O} & \mathrm{O} & \mathrm{O} & \mathrm{O}\\ \mathrm{O} & (1+\xi\Delta t)M^k_1 & \mathrm{O} & \mathrm{O} & \mathrm{O}\\ \mathrm{O} & \mathrm{O} & (1+\xi\Delta t)M^k_1 & \mathrm{O} & \mathrm{O}\\ \mathrm{O} & \mathrm{O} & \mathrm{O} & \rho M^k_1+\Delta t^2B^{k+1} & \mathrm{O}\\ \mathrm{O} & \mathrm{O} & \mathrm{O} & \mathrm{O} & \rho M^k_1+\Delta t^2B^{k+1}\end{pmatrix}, \tag{4.2.35}$$

$$M^k := \begin{pmatrix}M^k_1 & \mathrm{O} & \mathrm{O} & \mathrm{O} & \mathrm{O}\\ \mathrm{O} & M^k_1 & \mathrm{O} & \mathrm{O} & \mathrm{O}\\ \mathrm{O} & \mathrm{O} & M^k_1 & \mathrm{O} & \mathrm{O}\\ \mathrm{O} & \mathrm{O} & \mathrm{O} & \rho M^k_1 & \mathrm{O}\\ \mathrm{O} & \mathrm{O} & \mathrm{O} & \mathrm{O} & \rho M^k_1\end{pmatrix}, \tag{4.2.36}$$

$$S^k := \begin{pmatrix}\mathrm{O} & \mathrm{O} & \mathrm{O} & T^k_1 & \mathrm{O}\\ \mathrm{O} & \mathrm{O} & \mathrm{O} & 0.5T^k_2 & 0.5T^k_1\\ \mathrm{O} & \mathrm{O} & \mathrm{O} & \mathrm{O} & T^k_2\\ \bar{E}_s\bar{\eta}_1P^k_1 & \bar{E}_sP^k_2 & \bar{E}_s\bar{\eta}_2P^k_1 & \bar{\mu}S^k_1+0.5\mu_1S^k_2 & \mu_2S^k_3+0.5\mu_1S^k_4\\ \bar{E}_s\bar{\eta}_2P^k_2 & \bar{E}_sP^k_1 & \bar{E}_s\bar{\eta}_1P^k_2 & 0.5\mu_1S^k_3+\mu_2S^k_4 & 0.5\mu_1S^k_1+\bar{\mu}S^k_2\end{pmatrix}, \tag{4.2.37}$$

and

$$\boldsymbol{f}^k(\boldsymbol{w}^k) := \begin{pmatrix}\boldsymbol{f}^k_{\varepsilon_{11}}(\boldsymbol{w}^k)\\ \boldsymbol{f}^k_{\varepsilon_{12}}(\boldsymbol{w}^k)\\ \boldsymbol{f}^k_{\varepsilon_{22}}(\boldsymbol{w}^k)\\ \boldsymbol{f}^k_1-a\cdot\boldsymbol{b}^k_1\\ \boldsymbol{f}^k_2-a\cdot\boldsymbol{b}^k_2\end{pmatrix}. \tag{4.2.38}$$

Here,

$$\bar{E}_s := \frac{E_s\sqrt{\rho}}{1+\eta}, \qquad \bar{\eta}_1 := \frac{1-\eta}{1-2\eta}, \qquad \bar{\eta}_2 := \frac{\eta}{1-2\eta}, \qquad \bar{\mu} := \mu_1+\mu_2.$$

Since $\boldsymbol{f}^{k+1}$ is a non-linear function of $\boldsymbol{w}^k$, we have to solve the equations by means of an iterative method. We choose the iterative method of Picard. We have

$$\boldsymbol{w}^{k+1} = \left(\overline{M}^{k+1}-\Delta tS^{k+1}\right)^{-1}\left(M^k\boldsymbol{w}^k+\Delta t\boldsymbol{f}^{k+1}(\boldsymbol{w}^{k+1})\right). \tag{4.2.39}$$

Starting with an initial guess $\boldsymbol{w}_0^{k+1}$, we define for $n \geq 0$:

$$\boldsymbol{w}_{n+1}^{k+1} := \left(\overline{M}^{k+1} - \Delta t S^{k+1}\right)^{-1} \left(M^k \boldsymbol{w}^k + \Delta t \boldsymbol{f}^{k+1}(\boldsymbol{w}_n^{k+1})\right). \tag{4.2.40}$$

This process will be continued until the residual

$$r_n := \left|\left|\left(\overline{M}^{k+1} - \Delta t S^{k+1}\right) \boldsymbol{w}_n^{k+1} - \left(M^k \boldsymbol{w}^k + \Delta t \boldsymbol{f}^{k+1}(\boldsymbol{w}_n^{k+1})\right)\right|\right|_2, \tag{4.2.41}$$

is small enough. Here $||\cdot||_2$ denotes the Euclidean norm.

4.3. Results

In this session, we will mainly display the results regarding all the aforementioned two-dimensional models, in particular, the area changing over time and the deformation of the computational domain. The parameter values are taken from Table 4.1. Here, we consider a body force only in horizontal direction, which is defined

Description	**Parameter**	**Value**	**Unit**	**Application**
Fibroblasts measure	C_f	4.0	-	all models
Duration of body force	t_f	10.0	day	all models
Maximal magnitude of body force	$\bar{f}$	50.0	$\mathrm{N{\cdot}g{\cdot}cell^{-1}{\cdot}cm^{-1}}$	all models
Elasticity of the ECM	E_s	31.0	$\mathrm{N{\cdot}cm^{-2}}$	all models
Length of domain in x-direction	L_x	1.0	cm	all models
Length of domain in y-direction	L_y	1.0	cm	all models
Number of gridnodes in x-direction	n_x	20	-	all models
Number of gridnodes in y-direction	n_y	20	-	all models
Time step	Δt	0.04	day	all models
Material density	ρ	1.02	$\mathrm{g{\cdot}cm^{-1}}$	models including Cauchy Momentum Eq.
Shear viscosity	μ_1	100.0	$\mathrm{N{\cdot}day{\cdot}cm^{-1}}$	visco- and morphoelastic models
Bulk viscosity	μ_2	100.0	$\mathrm{N{\cdot}day{\cdot}cm^{-1}}$	visco- and morphoelastic models
Degree of permanent deformation	ξ	0.05	-	morphoelastic model
Duration of simulated time	T	16	day	all models
Parameter in Robin boundary condition	a	31.0	-	all models

Table 4.1: Overview of used parameters in the two-dimensional models

as follows:

$$\boldsymbol{f}(x,y,t) = \begin{cases} \left(\bar{f} \cdot T(t), 0\right)^T, & \text{if } 0 \leq x \leq x\left(\frac{L_x}{2}, t\right), \\ \left(-\bar{f} \cdot T(t), 0\right)^T, & \text{if } x > x\left(\frac{L_x}{2}, t\right), \end{cases} \tag{4.3.1}$$

where $T(t)$ is defined as in Equation (5.1.7).

In Figure 4.1, the displacement of the nodal points is shown at $t = 8$ days. It can be seen that the tissue, in particular the points in the centre of the computational domain, mainly migrates in the horizontal direction. Furthermore, in the vertical direction, especially around $x = 0$, the tissue slightly expands, which is due to the Poisson's effect. We only show one plot of this type for all the models, since the differences are not so clearly visible in the plot.

In Figure 4.2, the dynamic of the area of the computational domain is shown for the purely elastic, viscoelastic and morphoelastic model respectively. We see that the behaviour of the area is the same as the behaviour of the length in the one-dimensional case. In the elastic model, a sharp transition can be observed at $t = 10$ days (the moment at which the body force starts to decrease). In the viscoelastic model, the transition starts at the same moment, but it is much smoother due to the delay caused by viscosity. In the morphoelastic model, since $\xi > 0$, it can be observed that the wound does not fully recover to its initial state: a permanent deformation is developed.

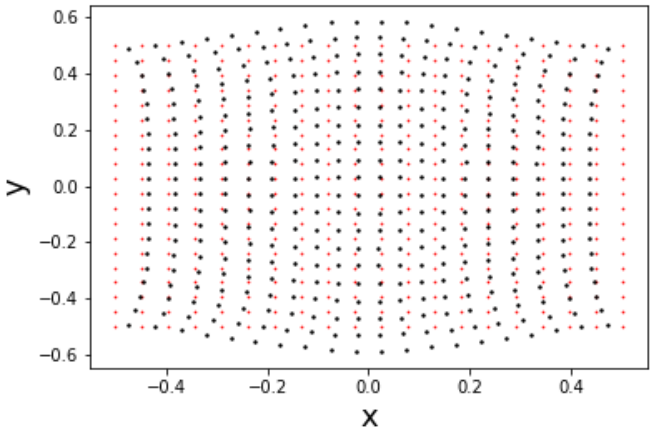

Figure 4.1: The nodal points of finite element methods are shown, where red scatters present the initial positions and black scatters represent the positions at $t = 8$ days. Here, the morphoelastic model is used.

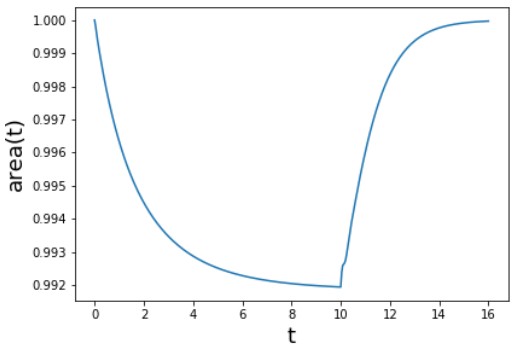

A. Elastic model

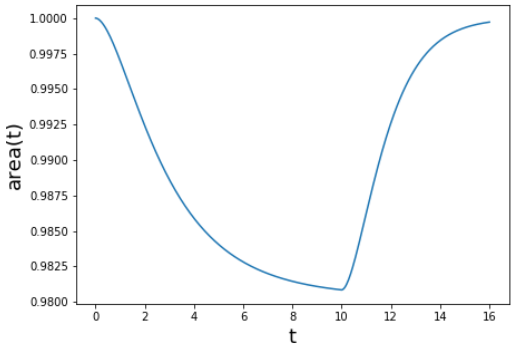

B. Viscoelastic model

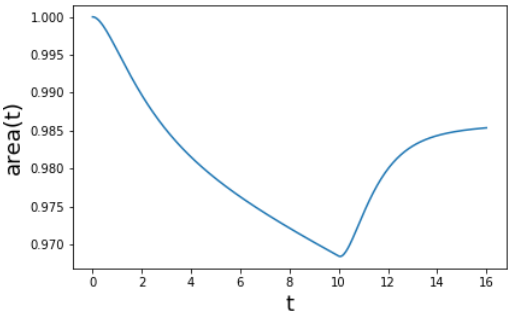

C. Morphoelastic model

Figure 4.2: Plots of tissue area as function of time

5

Two-dimensional morphoelastic model with point forces

In the former chapters, a general body force was used to model the contraction of the wound. in the application of wound healing, we model the point forces exerted by the (myo)fibroblasts in the form of Dirac Delta distributions. Therefore, the model stated in Chapter 4 will be modifeid due to the special characteristics of the Dirac Delta distribution. At first, the mathematical model is described. Subsequently, the results are presented. In the last section, the model is tested by means of a parameter sensitivity test.

5.1. Mathematical model

During wound healing, in particular the proliferation phase, the (myo)fibroblasts exert pulling forces on the direct environment (the extracellular matrix) and cause local contractions of the wound. According to [1], we will use Dirac Delta distributions in order to model these point forces. Suppose there is one single (myo)fibroblast in the domain with cell centre at $\boldsymbol{x}_c$. We assume that the forces are exerted on the cell boundary, which is a continuous curve denoted by $\partial\Omega_c$ and the forces are directed towards $\boldsymbol{x}_c$. Dividing $\partial\Omega_c$ into multiple line segments, the corresponding force then becomes [1], [16]

$$\boldsymbol{f}_p(\boldsymbol{x}) = \sum_{j=1}^{N_S} P \cdot \boldsymbol{n}(\boldsymbol{x})\delta(\boldsymbol{x}-\boldsymbol{x}_j)\Delta\Gamma_j, \tag{5.1.1}$$

where N_S is the number of line segments of the cell, P is the magnitude of the pulling force per length unit, $\boldsymbol{n}(\boldsymbol{x})$ is the unit inward pointing unit normal vector (towards the cell centre) at position $\boldsymbol{x}$, $\boldsymbol{x}_j$ is the midpoint on the line segment j and $\Delta\Gamma_j$ is the length of the line segment j. This method is also used in fluid dynamics and is known as the immerse boundary method [16]. As $N_S \to \infty$, that is, $\Delta\Gamma_N^j \to 0$, Equation (5.1.1) becomes

$$\boldsymbol{f}_p(\boldsymbol{x}) = \oint_{\partial\Omega_c} P \cdot \boldsymbol{n}(\boldsymbol{x})\delta(\boldsymbol{x}-\boldsymbol{x}_s)\mathrm{d}\Gamma, \tag{5.1.2}$$

where $\boldsymbol{x}_s$ is a point on the cell boundary. Usually, a biological cell is modelled as a circle in two dimensions and a sphere in three dimensions. As $N_S \to \infty$, the curve $\partial\Omega_c$ becomes a circle. However, it will significantly increase the computational cost [16]. Besides, we are working on a relatively small wound with multiple cells, so in the quest of the balance of the accuracy of the solution and the computational efficiency, simple polygon like triangles ($N_S = 3$) or squares ($N_S = 4$) are chosen to approximate the cell boundary. Hereby, we follow the methods proposed in [1], to model this as a square surrounding the cell, with at each edge of the square a point force directed towards the cell: see Figure 5.1. Consider a square with side lengths $2 \cdot r_s$ surrounding the (myo)fibroblast. The value of r_s is chosen in such a way that the area of the square-shaped cell is equal to the area of the original circle-shaped cell. This indicates that

$$r_s = \frac{\sqrt{\pi}R}{2}, \tag{5.1.3}$$

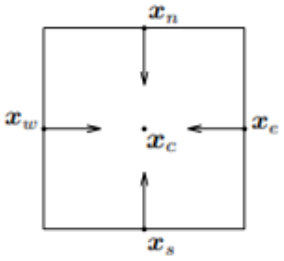

Figure 5.1: Cellular point forces exerted on a square curve towards the cell center. Image source: [1]

where R is the radius of the circle-shaped cell. The midpoint of each side is given by

$$\begin{aligned} \boldsymbol{x}_n &= (x_c, y_c + r_s)^T, \\ \boldsymbol{x}_e &= (x_c + r_s, y_c)^T, \\ \boldsymbol{x}_s &= (x_c, y_c - r_s)^T, \\ \boldsymbol{x}_w &= (x_c - r_s, y_c)^T. \end{aligned} \tag{5.1.4}$$

For the square-shaped cell as shown in Figure 5.1, using Equation (5.1.1), the cell traction force becomes

$$\boldsymbol{f}_p(\boldsymbol{x}) = 2r_s P\left(\boldsymbol{n}_n \delta(\boldsymbol{x} - \boldsymbol{x}_n) + \boldsymbol{n}_e \delta(\boldsymbol{x} - \boldsymbol{x}_e) + \boldsymbol{n}_s \delta(\boldsymbol{x} - \boldsymbol{x}_s) + \boldsymbol{n}_w \delta(\boldsymbol{x} - \boldsymbol{x}_w)\right), \tag{5.1.5}$$

where P is the force magnitude per length unit and $\boldsymbol{n}_n, \boldsymbol{n}_e, \boldsymbol{n}_s$ and $\boldsymbol{n}_w$ are the unit vectors pointing towards $\boldsymbol{x}_c$ (out of the northern, eastern, southern and western boundary respectively). This is an approximation of the contracting point force at $\boldsymbol{x}_c$, as $r_s \to 0$. Equation (5.1.1) defines the force for a (myo)fibroblast with fixed location and time-independent force. We can generalize the equation for a moving (myo)fibroblast with time-dependent traction force by

$$\boldsymbol{f}_p(\boldsymbol{x}, t) = \sum_{j=1}^{N_S} P(t) \cdot \boldsymbol{n}(\boldsymbol{x}, t) \delta(\boldsymbol{x} - \boldsymbol{x}_j(t)) \Delta\Gamma_j. \tag{5.1.6}$$

In this chapter, $P(t)$ was defined in the same way as in Equation (5.1.8), with $P(t) = P \cdot T(t)$, where $T(t)$ is defined as

$$T(t) := \begin{cases} 1 - \exp\left(-3 \cdot t / t_f\right), & \text{if } 0 \le t < t_f, \\ \left(1 - \exp\left(-3 \cdot t / t_f\right)\right) \exp\left(-\left(t - t_f\right)\right), & \text{if } t \ge t_f. \end{cases} \tag{5.1.7}$$

Furthermore, if there are multiple cells, the total force equals the sum of the cell traction forces of each cell:

$$\boldsymbol{f}(\boldsymbol{x}, t) = \sum_{i=1}^{N_c(t)} \boldsymbol{f}_p^i(\boldsymbol{x}, t), \tag{5.1.8}$$

where $N_c(t)$ is the number of cells at time t and $\boldsymbol{f}_p^i(\boldsymbol{x}, t)$ denotes the cell traction force belonging to cell i at location $\boldsymbol{x}$ and time t, as defined in Equation (5.1.6). Hence, we obtain following model:

$$(IBVP_7): \begin{cases} \frac{\mathrm{D}(\rho \boldsymbol{v})}{\mathrm{D}t} + \boldsymbol{v}\rho(\nabla \cdot \boldsymbol{v}) = \nabla \cdot \underline{\underline{\sigma}} + \boldsymbol{f}(\boldsymbol{x}, t), & \boldsymbol{x} \in \Omega, t > 0, \\ \underline{\underline{\sigma}} = \frac{\mu_1}{2}\left(\nabla \boldsymbol{v} + (\nabla \boldsymbol{v})^T\right) + \mu_2 (\nabla \cdot \boldsymbol{v})\, \underline{\underline{I}} + \frac{E_s\sqrt{\rho}}{1+\eta}\left(\underline{\underline{\varepsilon}} + \frac{\eta}{1-2\eta}\mathrm{Tr}(\underline{\underline{\varepsilon}})\underline{\underline{I}}\right), & \boldsymbol{x} \in \Omega, t > 0, \\ \frac{\mathrm{D}\underline{\underline{\varepsilon}}}{\mathrm{D}t} + \underline{\underline{\varepsilon}}\ \mathrm{skew}\left(\frac{\partial \boldsymbol{v}}{\partial \boldsymbol{x}}\right) - \mathrm{skew}\left(\frac{\partial \boldsymbol{v}}{\partial \boldsymbol{x}}\right)\underline{\underline{\varepsilon}} + \left(\mathrm{Tr}\left(\underline{\underline{\varepsilon}}\right) - 1\right) \mathrm{sym}\left(\frac{\partial \boldsymbol{v}}{\partial \boldsymbol{x}}\right) = -\underline{\underline{g}}, & \boldsymbol{x} \in \Omega, t > 0, \\ \underline{\underline{\sigma}} \cdot \boldsymbol{n} + a\boldsymbol{u} = \boldsymbol{0}, & \boldsymbol{x} \in \partial\Omega, t > 0, \\ \boldsymbol{u}(\boldsymbol{x}, 0) = \boldsymbol{0}, & \boldsymbol{x} \in \Omega, \\ \boldsymbol{v}(\boldsymbol{x}, 0) = \boldsymbol{0}, & \boldsymbol{x} \in \Omega. \end{cases}$$

where

$$\boldsymbol{f}(\boldsymbol{x},t) = \sum_{i=1}^{N_c(t)} \sum_{j=1}^{N_S^i} P(t)\cdot \boldsymbol{n}_j(\boldsymbol{x},t)\delta(\boldsymbol{x}-\boldsymbol{x}_j(t))\Delta\Gamma_j. \tag{5.1.9}$$

The weak form will be the same as (W6) in Chapter 4. However, in this weak form, the expression $\int_{\Omega(t)} f_d\phi_d \,\mathrm{d}\Omega$, $(d = 1,2)$ can now be simplified a little further. We have:

$$\begin{aligned}
\int_\Omega \boldsymbol{f}\circ\boldsymbol{\phi}\,\mathrm{d}\Omega &= \sum_{i=1}^{N_c(t)}\sum_{j=1}^{N_S^i}\int_\Omega 2r_sP\boldsymbol{n}_j(\boldsymbol{x},t)\delta(\boldsymbol{x}-\boldsymbol{x}_j(t)\circ\boldsymbol{\phi}\,\mathrm{d}\Omega \\
&= \sum_{i=1}^{N_c(t)}\int_\Omega 2r_sP\begin{pmatrix}\delta(\boldsymbol{x}-\boldsymbol{x}_e^i(t))-\delta(\boldsymbol{x}-\boldsymbol{x}_w^i(t))\\ \delta(\boldsymbol{x}-\boldsymbol{x}_s^i(t))-\delta(\boldsymbol{x}-\boldsymbol{x}_n^i(t))\end{pmatrix}\circ\boldsymbol{\phi}\,\mathrm{d}\Omega \\
&= \sum_{i=1}^{N_c(t)} 2r_sP\begin{pmatrix}\phi_1(\boldsymbol{x}_e^i(t),t)-\phi_1(\boldsymbol{x}_w^i(t),t)\\ \phi_2(\boldsymbol{x}_s^i(t),t)-\phi_2(\boldsymbol{x}_n^i(t),t)\end{pmatrix},
\end{aligned} \tag{5.1.10}$$

where $\boldsymbol{f}\circ\boldsymbol{\phi} := (f_1\phi_1, f_2\phi_2)^T$.

5.2. Numerical Result

In this section, the numerical results are shown for $(IBVP_7)$ with traction force function as defined in Section 5.1. We start with the simulation in which there is only one relatively big cell centered at the origin, then we consider multiple smaller cells, of which the size is comparable to the size of the mesh elements. In Figure

Description	**Parameter**	**Value**	**Unit**
Length of the domain in x-direction	Lx	0.2	cm
Length of the domain in y-direction	Ly	0.2	cm
Length of the wound in x-direction	Bx	0.04	cm
Length of the wound in y-direction	By	0.04	cm
Number of nodes in x-direction	nX	32	-
Number of nodes in y-direction	nY	32	-
Time step	Δt	0.03	day
Half of the sides of the cells (one cell simulation)	r_s	0.0222	cm
Half of the sides of the cells (multiple cells simulation)	r_s	0.001	cm
Young's modulus	E	31.0	N·cm^{-2}
Density	ρ	1.02	g·cm^{-3}
Shear viscosity	μ_1	100.0	N·day·cm^{-2}
Bulk viscosity	μ_2	100.0	N·day·cm^{-2}
Poisson's ratio	η	0.48	-
Degree of permanent deformation	ξ	0.15	-
Constant in Robin bnd. condition	a	1000.0	-
Magnitude of point forces (one cell simulation)	P	10.0	N
Magnitude of point forces (multiple cells simulation)	P	210.0	N
Moment at which force reaches maximum value	t_f	10.0	day
Duration of simulated time	T	18.0	day

Table 5.1: Overview of used parameters in Section 5.2

5.2, the results are shown for the one big cell. We assume the cells have no active displacement but only passive convections. In other words, the displacements of cells are only caused by the displacement of the enviroment, that is, the displacement of the grid points. Furthermore, this indicates that throughout the entire simulation, the cells will stay in the same triangular mesh element. The parameter values used in the simulations are shown in Table 5.1. For r_s and P, two values are shown in the table, since they are different for the simulation with one big cell and the simulation with multiple small cells.

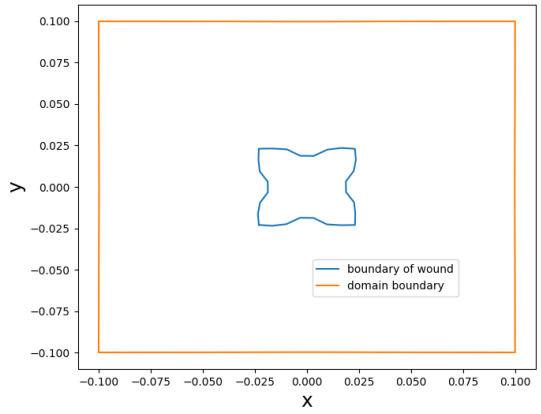

A. Plot of domain and wound boundary in x,y-plane at $t = 10$ days

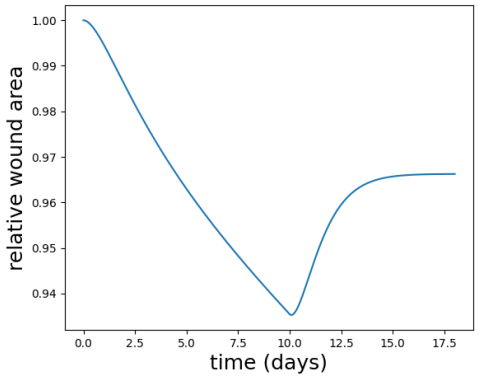

B. Plot of wound area as function of time

Figure 5.2: Morphoelastic model with traction force induced by one cell

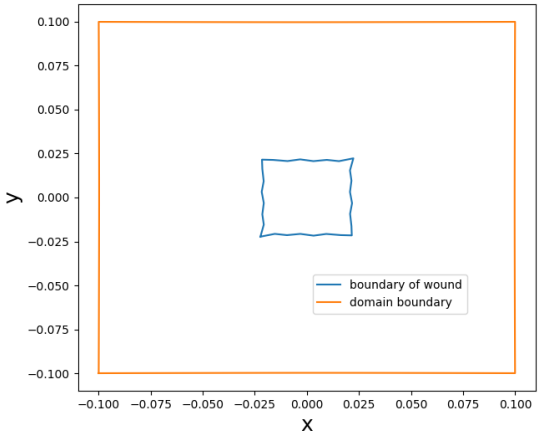

A. Plot of domain and wound boundary in the x,y-plane at $t = 10$ days

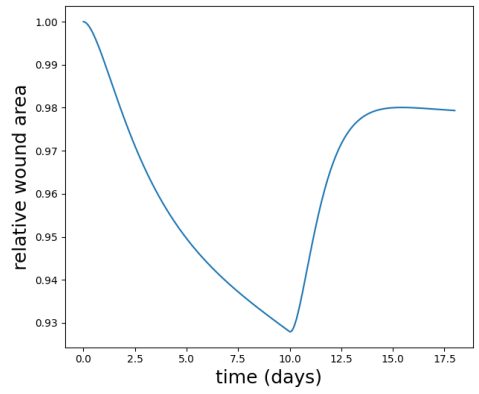

B. Plot of wound area as function of time

Figure 5.3: Morphoelastic model with traction force induced by multiple cells

In Figure 5.3, the results are shown for multiple cells. The total number of cells is 49 and they located uniformly over the wound area, that is, for $i \in \{0,..,48\}$:

$$\boldsymbol{x}_c^i = (-0.5 \cdot Bx + (0.5 + i_1) \cdot Bx/7, -0.5 \cdot By + (0.5 + i_2) \cdot By/7)^T, \tag{5.2.1}$$

where $\boldsymbol{x}_c^i$ denotes the location of the cell center of cell i, $i_1 := i\%7$ and $i_2 = \text{floor}(i/7)$ with floor denoting the function which rounds the number down to an integer, Bx and By are the length of the wound in x-direction and y-direction.

The traction forces are visible in the plots of the wound in the x,y-plane. In Figure 5.2A, the deformation of the wound area is mainly present in the midpoint of the cell sides, where the point forces are exerted. In Figure 5.3A, the deformation is more spread out along the sides of the wound since the cells are distributed uniformly in the entire wound. Figure 5.2B and Figure 5.3B both show that the area of the wound decreases due to the traction forces and that a permanent deformation occurs.

5.3. Parameter analysis

Mathematical modelling suffers from the fact of lacking the parameter values. Besides the complicated nature of wound healing model, different patients have different characteristics of skin, which results into different healing processes. Hence, it is essential to have sensitivity tests regarding parameters to validate the model, and to have a better insight into the wound healing. To investigate the behaviour of the models, several parameter sensitivity tests were done. In a parameter sensitivity test, computational simulations are carried out with all parameters fixed, except for one parameter, which is varied among the simulations. Without specific declaration, the parameter values used in the model are shown in Table 5.2. Furthermore, in Table 5.3, the ranges of the varied parameters are shown. The wound area is defined to be a square in the center of

Description	**Parameter**	**Value**
Length of the domain in x-direction	Lx	0.2
Length of the domain in y-direction	Ly	0.2
Length of the wound in x-direction	Bx	0.04
Length of the wound in y-direction	By	0.04
Number of nodes in x-direction	nX	31
Number of nodes in y-direction	nY	31
Time step	Δt	0.03
Young's modulus	E	31.0
Density	ρ	1.02
Shear viscosity	μ_1	100.0
Bulk viscosity	μ_2	100.0
Poisson's ratio	η	0.48
Degree of the permanent deformation	ξ	0.15
Spring constant in Robin boundary condition	a	1000.0
Magnitude of the point forces	P	210.0
Half of the sides of the square-shaped cells	r_s	0.001
Moment at which force reaches maximum value	t_f	3.0
Number of cells in the wound	N_c	49

Table 5.2: Overview of used parameters in the parameter sensitivity tests

the domain. Most of the parameters are taken from [18] or estimated in this study.

5.3.1. Gridsize and time step

At first, we analyze some numerical parameters, namely the gridsize and the time step. As for the grid size, a plot is shown with ${}^{10}\log(h)$ on the horizontal axis , where h denotes the distance between the grid nodes. On the vertical axis, the relative area of the wound is shown. For example, if the relative area has a value of 0.95, then this means that the area is 95% of the original area. The values for h on the horizontal axis vary from $h = 0.02$ to $h = 0.004$, which in our domain corresponds to 10 and 50 grid nodes respectively, in each direction. The corresponding values of ${}^{10}\log(h)$ are from -1.699 to -2.398 respectively. The results area

Description	Parameter	Range of values
Distance between the (equidistant) gridnodes	h	$[0.0040, 0.020]$
Time step	Δt	$[0.0032, 0.0]$
Young's modulus	E	$[0.0, 100.0]$
Shear viscosity	μ_1	$[10, 400]$
Bulk viscosity	μ_2	$[10, 400]$
Degree of the permanent deformation	ξ	$[0.0, 0.5]$
Poisson's ratio	η	$[0.0, 0.495]$
Magnitude of the point forces	P	$[0.0, 500.0]$
Spring constant in Robin boundary condition	a	$[1.78, 316228]$

Table 5.3: Overview of ranges in the parameter sensitivity tests

shown for several moments of time. The number of iterations is 200, which means that the simulation runs from $t = 0$ till $t = 6.0$, with the time step given in Table 5.2. In Figure 5.4, the curves at $t = 1.5$, $t = 3.0$, $t = 4.5$ and $t = 6.0$ are shown in one figure, as well as the curve of the minimal values of the relative area throughout the entire simulation. The curve for the minimal area mostly overlaps with the curve for $t = 3$, since the force started decreasing at $t = 3$ (that is, $t_f = 3$). It is not necessary to show all the plots in a separate figure, since, although quantitatively different, they are qualitatively the same. Therefore, only the minimal area is shown in a separate plot. The convergence of the solution can be seen in Figure 5.4, since with smaller mesh

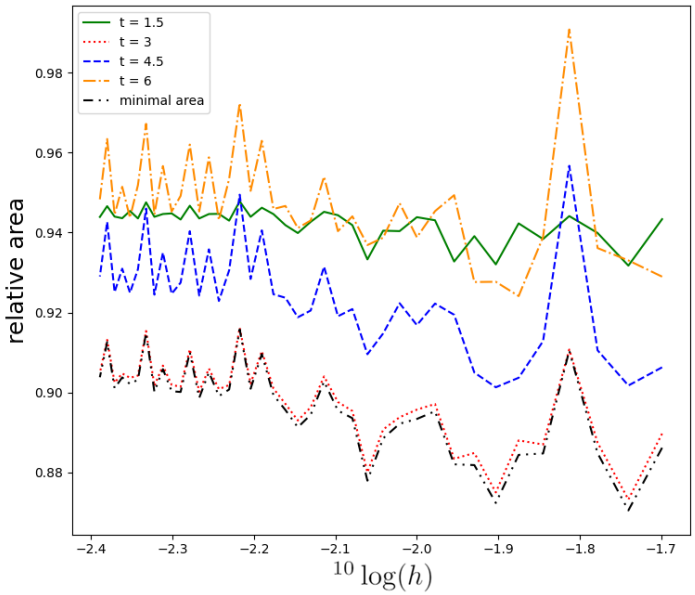

Figure 5.4: Relative wound area at moments as function of grid size

size, the wound area ratio at the same time point is getting more stable and less fluctuated. From around $h = 10^{-2.15}$, the wound area stays relatively stable as the size of mesh elements decreases. Therefore, we select 31 gridnodes in each coordinate of which the corresponding mesh size h is around $10^{-2.176}$, for the sake of the balance between the accuracy of the solution and the computational cost. Hence, in other simulations in this section, $h = 10^{-2.176}$ is selected as the size of the mesh elements. As for the time step, we show the results for time steps varying from $\Delta t = 10^0 = 1.0$ to $\Delta t = 10^{-2.5} \approx 0.00316$. On the horizontal axis, ${}^{10}\log(\Delta t)$ is shown, ranged from 0 to -2.5 (see Figure 5.5). Here, the results are clearly converging for values smaller than $\Delta t = 10^{-1.5} \approx 0.032$. Hence, in the rest of the simulations, a time step of 0.03 is maintained.

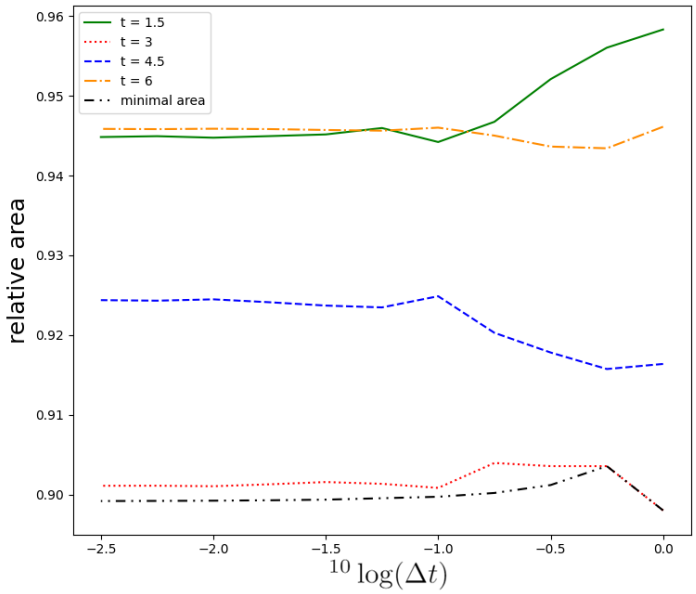

Figure 5.5: Relative wound area at moments as function of time step

5.3.2. Elasticity parameter

The next parameter that is to be analysed, is the elasticity parameter E, which is also called the Young's modulus. This parameter determines how stiff the computational domain is. It is varied from 0.0 to 100.0. The curves show a type of hyperbolic behaviour in Figure 5.6. This could be explained as follows. The same effect is visible when doing the parameter analysis for the one-dimensional model. Using the equations

$$\frac{\mathrm{d}\sigma}{\mathrm{d}x} + f = 0, \tag{5.3.1}$$

and

$$\sigma = \frac{\mathrm{d}u}{\mathrm{d}x}. \tag{5.3.2}$$

Multiplying Equation (5.3.1) with $\frac{1}{E}$, and combining the two equations, we obtain,

$$\frac{\mathrm{d}^2u}{\mathrm{d}x^2} = -\frac{1}{E}f, \tag{5.3.3}$$

Since the (contracting) force now is multiplied by $\frac{1}{E}$, which increases hyperbolically as $E \downarrow 0$, this indicates that the solution will increase hyperbolically as well. Hence, the relative area (or, in case of one dimension: the length) will show hyperbolic decrease as $E \downarrow 0$. In the one dimensional purely elastic model that was mentioned, for $E = 0$, the contraction becomes infinitely large, which results in a singular matrix to be solved. However, with viscoelasticity involved, this effect is cancelled. Although the model in $(IBVP_7)$ is more complex, the elasticity principle is the same. The elastic part of the stress tensor reads

$$\underline{\underline{\sigma}}_{elas} = \frac{E}{1+\eta}\left(\underline{\underline{\varepsilon}} + \frac{\eta}{1-2\eta}\mathrm{Tr}(\underline{\underline{\varepsilon}})\underline{\underline{I}}\right) \tag{5.3.4}$$

$$= \frac{E}{1+\eta}\left(\frac{1}{2}\left(\nabla \boldsymbol{u} + (\nabla \boldsymbol{u})^T\right) + \frac{\eta}{1-2\eta}\left(\frac{\partial u_1}{\partial x} + \frac{\partial u_2}{\partial y}\right)\underline{\underline{I}}\right). \tag{5.3.5}$$

The elastic part of the stress tensor is linearly related with E. Hence, varying the elasticity parameter E shows the same behaviour qualitatively.

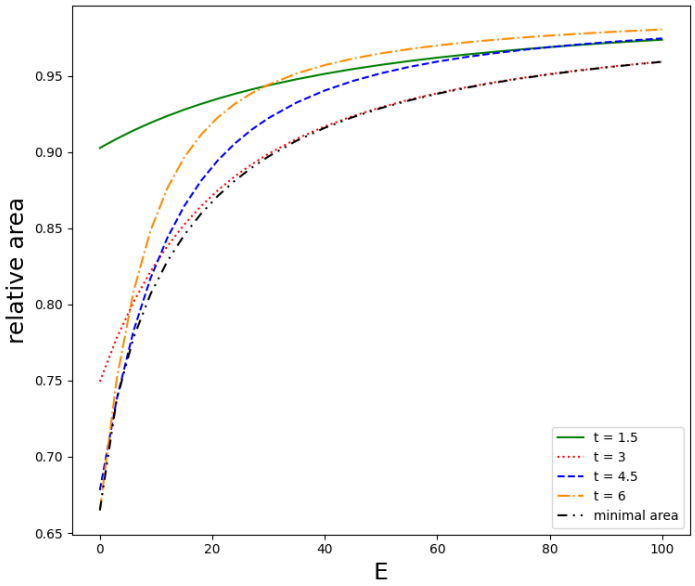

Figure 5.6: Relative wound area at moments as function of elasticity parameter

5.3.3. Viscoelasticity parameter

There are two viscosity parameters, μ_1 and μ_2, which determines the damping effect of the domain. In the simulations, we combined these two parameters and varied them both. The parameter μ in Figure 5.7 denotes a the scaling factor of μ_1 and μ_2: $\mu = 1$ corresponds to $\mu_1 = \mu_2 = 40$ and $\mu = 2$ corresponds to $\mu_1 = \mu_2 = 80$ etc. There is a gap between the graph for $t = 3$ and the graph for the minimal area for high μ. This is due to the fact that the viscoelasticity causes a delay in the effect of the forces, so that the minimal area is reached later when viscoelasticity parameter is large. Furthermore, the curves show slightly hyperbolic behaviour, which can be explained in a similar way as is done for the elasticity parameter. In Figure 5.7, the curves for $t = 4.5$ and $t = 6$ show little different behaviour near $\mu = 0$. This is due to numerical instability as the portion of viscoelasticity becomes small. Therefore, it could be recommended to use a purely elastic model rather as soon as viscoelasticity is negligible.

5.3.4. Morphoelasticity parameter

In $(IBVP_6)$, the parameter ξ determines the degree of the permanent deformation. Figure 5.8 shows the results of the parameter analysis for the morphoelasticity parameter ξ. Varying ξ does not influence the relative area at $t = 1.5$ that much, since, the permanent deformation is not yet developed at that time point. However, the influence of ξ increases for later time points, which is in accordance with the fact that ξ determines the degree of permanent deformation.

5.3.5. Poisson's ratio

In Figure 5.9, the results are shown for Poisson's ratio η (see Subsection 2.2.5). Poisson's ratio indicates how much a material will deform in the direction perpendicular to the force direction. If $\eta = 0.5$, the material is incompressible. In Figure 5.9, we can see that area$(\Omega) \uparrow 1.0$ as $\eta \uparrow 0.5$. In that case, the total area decreases not so much, because compression in one direction cause a in other directions (see Figure 2.5 in Section 2.2.5). Furthermore, the curves in Figure 5.9 show a hyperbolic behaviour. This can be explained by analyzing the elastic part of the equation for the stress tensor, which was already defined in Equation (2.3.8). As $\eta \uparrow 0.5$ (that is, the material gradually becomes incompressible), we have that $1 - 2\eta \downarrow 0$, causing a singularity at $\eta = 0.5$ and causing $\frac{1}{1-2\eta}$ to grow hyperbolic as $\eta \uparrow 0.5$.

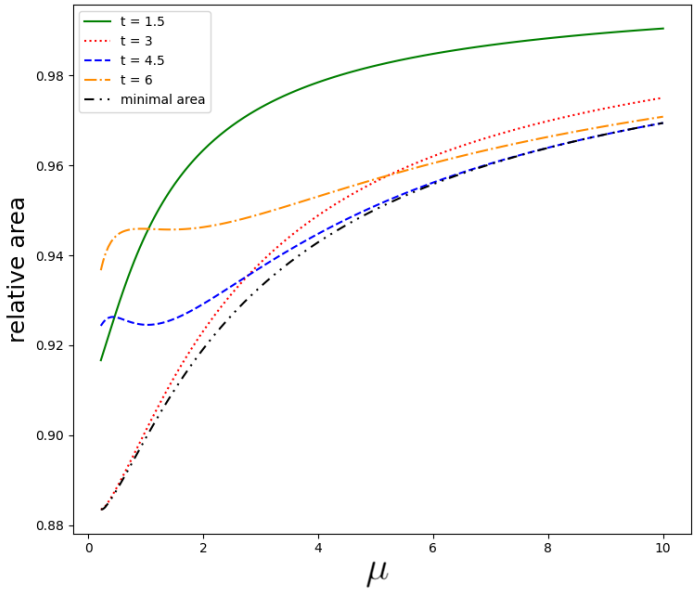

Figure 5.7: Relative wound area at moments as function of viscoelasticity parameter

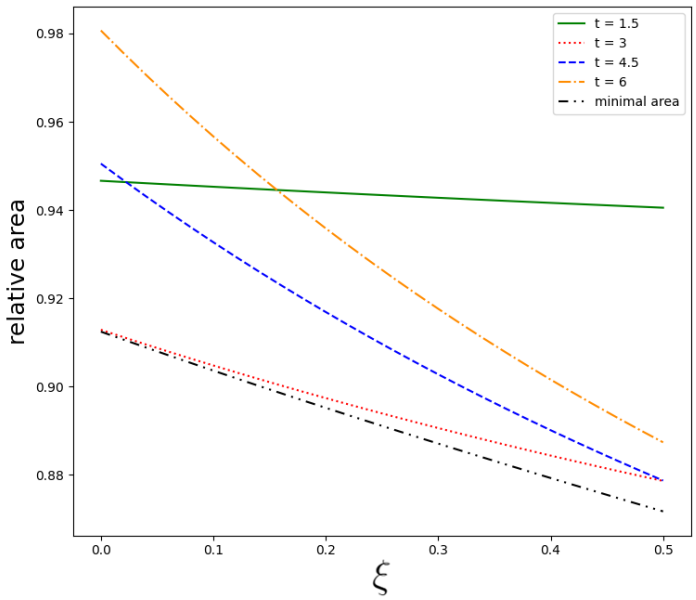

Figure 5.8: Relative wound area at moments as function of morphoelasticity parameter

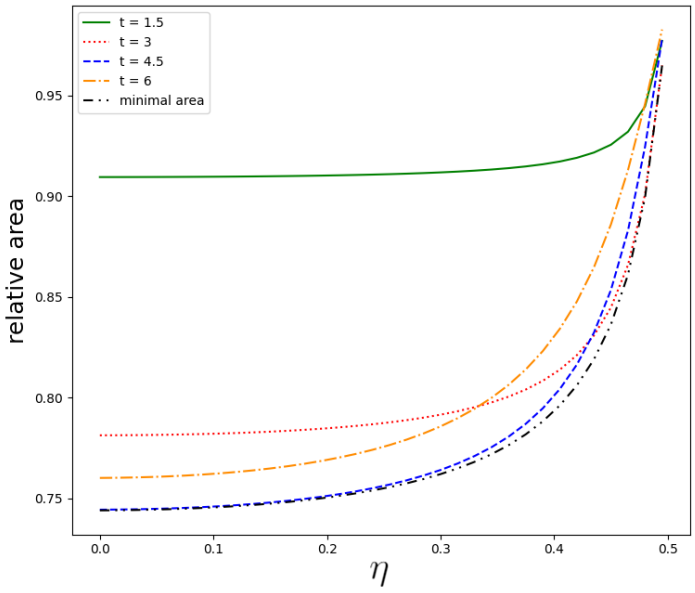

Figure 5.9: Relative wound area at moments as function of Poisson's ratio

5.3.6. Magnitude of cell traction forces

In Figure 5.10, the results are represented for the force that is exerted by the (myo)fibroblasts in the wound area. Here, P is defined as in Equation (5.1.1). The result is as expected: the minimal area shrinks (linearly) as the force increases.

5.3.7. Boundary condition value

In this subsection, we look into the spring constant a the Robin boundary condition in $(IBVP_7)$. Robin's boundary condition benefits from the flexibility of the value of a. If a is relatively small, the boundary is more free and hence, it is closer to a Neumann boundary condition. However, as $a \to \infty$ a Dirichlet boundary condition is considered. In Figure 5.11 the results of the sensitivity test are shown. On the horizontal axis, $^{10}\log(a)$ is put instead of a, since an exponential scale is to have a wide range of values. Since the behaviour of the individual curves is not so clearly visible in Figure 5.11, the curve of the minimal area is shown seperately in Figure 5.12 The curves show that, as expected, the relative area is closer to 1 as the boundary becomes more fixed. However, it appears that the relative area of the wound is not affected significantly from a. That can be explained by the fact that the wound area is far away from the boundary of the computational domain.

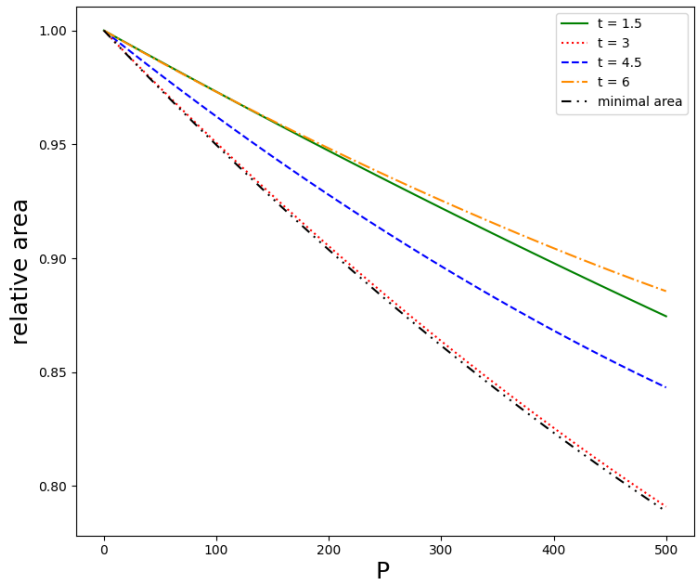

Figure 5.10: Relative wound area at moments as function of cellular force

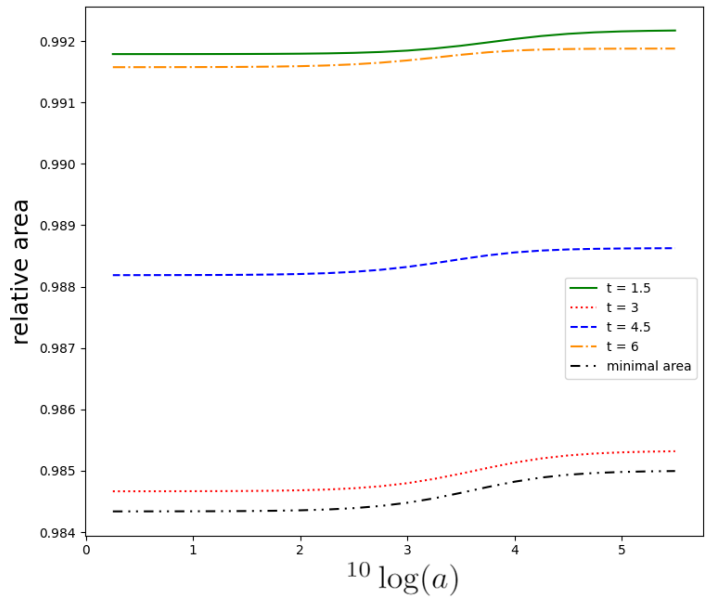

Figure 5.11: Relative wound area at moments as function of the spring constant in the boundary condition

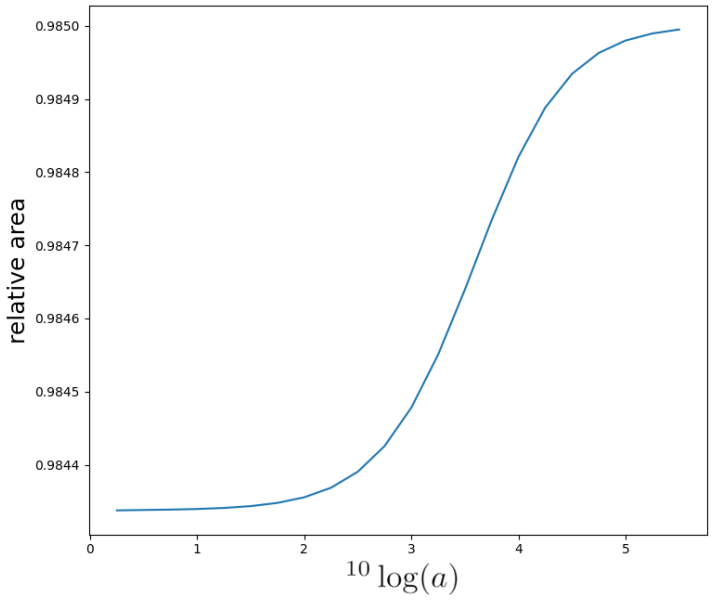

Figure 5.12: Minimal relative wound area as function of the spring constant in the boundary condition

6

Agent-based model for wound healing in burn injuries

One of the main goals of the project is, to combine the morphoelasticity model with the agent-based model that was developed in [12]. We start with the description of the combined model, followed by the results from our simulations. In the last section, Monte Carlo simulations are run to obtain more insights into the behaviour of the model and the influence of parameters on the outcome of the model.

6.1. Description of the model

Skin contains various components, which cannot all be incorporated into the model. With necessary simplifications, we consider the following skin components in our model: cells, cytokines and extracellular matrix (ECM). Hence, the model carries out the following calculations:

- Computation of the location and movements of three phenotypes of cells (regular fibroblasts, myofibroblasts and macrophages);
- Cellular proliferation (division), apoptosis (programmed death) and differentiation;
- Computation of the concentration of two chemokines (PDGF and TGF-β);
- Computation of the substrate contraction due to cellular traction forces.

Since it is impossible to incorporate every aspect of activities in the skin, we make some simplifications in the biological system (see [12] and [16]):

- The division of myofibroblasts and macrophages is neglected;
- The cell geometry is assumed to be constant;
- When a fibroblast proliferates, the cell centers of the daughter cells are assumed to move into opposite directions with a distance of half the cell radius. The directions are determined randomly;
- Cell division, death and differentiation are determined from an exponential distribution.

In the following subsections, the model will be explained in more detail.

6.1.1. Cell displacements

Cell displacement is determined by a series of mechanisms, regardless of the cell phenotype:

- The presence of other cells in the neighbourhood of the cell, which can attract other cells within a certain distance or on the other hand repel against others if it collides other cells;
- Chemotaxis, that is, cells move towards (or in some cases: away from) high concentrations of chemokines;
- Passive convections, caused by contraction of the wound as computed in the morphoelasticity model;

- Random walk, which is modelled by a Wiener process.

Hence, the displacement of the cells can be determined by

$$\mathrm{d}\boldsymbol{x}_i(t) = \kappa_i M(\boldsymbol{x}_i)\boldsymbol{z}_i \,\mathrm{d}t + s_c^i \frac{\nabla c(\boldsymbol{x}_i, t)}{||\nabla c||_2} \,\mathrm{d}t + \boldsymbol{v}(\boldsymbol{x}_i(t), t) \,\mathrm{d}t + \sqrt{2D}\,\mathrm{d}\boldsymbol{W}(t), \tag{6.1.1}$$

where $\mathrm{d}\boldsymbol{x}_i$ denotes the displacement of cell i at time t and κ_i is a measure that is dependent of several properties of the cells, $M(\boldsymbol{x}_i)$ is the magnitude of the total strain energy, (i.e. attraction and repulsion between cells) experienced by the cell and $\boldsymbol{z}_i$ represents the direction of movement caused by the strain energies. Furthermore, $\boldsymbol{v}(\boldsymbol{x}_i(t), t)$ denotes the velocity of the passive convection at the location $\boldsymbol{x}_i(t)$ of the cell center and $\sqrt{2D}\,\mathrm{d}\boldsymbol{W}(t)$ is a Wiener process, where D is a cell diffusivity parameter. Additionally, s_c^i is a measure of chemotaxis and ∇c denotes the gradient of the concentration of the chemokine by which the cell is attracted. In the case of fibroblasts, this is TGF-β, whereas the macrophages are attracted by large gradients of the PDGF concentration. If $||\nabla c||_2 = 0$, the quotient $\frac{\nabla c(t,x_i)}{||\nabla c||_2}$ is set to zero.

A brief description of the mechanisms in Equation (6.1.1) will be given. More details can be found in [12], [16] and Chapter 5. For chemotaxis, in the case of (myo)fibroblasts, the triggering chemokine is TGF-β, whereas for macrophages, it is PDGF. The displacements from chemotaxis are determined by the normalized gradient. This is done to avoid extreme displacements caused from high gradients. The parameter s_c^i in Equation (6.1.1) is determined in the following way:

$$s_c^i := \nu \cdot S(r^i) \cdot (1 - S(r^i)), \tag{6.1.2}$$

where

$$S(r) := \frac{1}{2}\left(1 + \sin\left(\left(r - \frac{1}{2}\right)\pi\right)\right), \tag{6.1.3}$$

and r^i denotes the number of receptors bound to cell i and ν is a chemotaxis constant, which differs per phenotype of cells. The number of receptors bound to a cell changes over time, dependent of the concentration of chemokines:

$$\frac{\mathrm{d}r^i}{\mathrm{d}t} = \begin{cases} -d^u r^i + d^b c_P(\boldsymbol{x}_i, t)(1 - r^i), & \text{if } i \text{ is a fibroblast,} \\ -d^u r^i + d^b c_\beta(\boldsymbol{x}_i, t)(1 - r^i), & \text{if } i \text{ is a macrophage,} \end{cases} \tag{6.1.4}$$

where d^u and d^b denote the unbinding rate and binding rate respectively.

For the strain energy densities, each individual cell has a minimal native strain energy density, independent from the presence of other cells, which we denote with M_j^0 for cell j. The total magnitude of the strain energy densitiy belonging to a cell i is computed in the following way:

$$M_i(\boldsymbol{x}_i) = M_{i,attr} - M_{i,col}, \tag{6.1.5}$$

where M_{attr} is the attracting energy and M_{col} is the repelling or collision energy. The attracting energy is defined as

$$M_{i,attr} = \sum_{j=1}^{N_c(t,d_i)} M_j^0 \exp\left(\frac{E_s}{E_c} \cdot \frac{||\boldsymbol{x}_i - \boldsymbol{x}_j||}{R}\right), \tag{6.1.6}$$

where $N_c(t, d_i)$ is the number of cells that is located within the detection range d_i of cell i, $\boldsymbol{x}_i$ and $\boldsymbol{x}_j$ are the locations of the cell centers, R is the cell radius, E_s and E_c are the elasticity modulus of the substrate and of the cell and the M_j^0 are the native strain energy densities. The collision energy is defined as

$$M_{i,col} = \sum_{j=1, j\neq i}^{N_c(t)} \frac{4E_c \cdot (Rh_{ij})^{2.5}}{15\sqrt{2}\pi}, \tag{6.1.7}$$

where $N_c(t)$ denotes the total number of cells in the domain and h_{ij} is the overlapping distance between cells i and j, defined as

$$h_{ij} = \max\left(2R - \left|\left|\boldsymbol{x}_i - \boldsymbol{x}_j\right|\right|, 0\right). \tag{6.1.8}$$

Note that $M_{i,col} = 0$ if cell i does not collide any other cells. The direction $\boldsymbol{z}_i$ of the displacement caused by strain energy is a normalized weighed average of the vectors connecting cell i with the surrounding cells, that is:

$$\boldsymbol{z}_i = \frac{\bar{\boldsymbol{z}}_i}{||\bar{\boldsymbol{z}}_i||}, \tag{6.1.9}$$

where

$$\bar{\boldsymbol{z}}_i = \sum_{j=1, j\neq i}^{N_c(t,d_i)} M_j^0 \exp\left(\frac{E_s}{E_c} \cdot \frac{||\boldsymbol{x}_i - \boldsymbol{x}_j||}{R}\right) \frac{\boldsymbol{x}_j - \boldsymbol{x}_i}{||\boldsymbol{x}_j - \boldsymbol{x}_i||}. \tag{6.1.10}$$

The measure κ_i in Equation (6.1.1) is determined in the following way:

$$\frac{\mathrm{d}r^i}{\mathrm{d}t} = \begin{cases} \kappa_i = K_i \cdot (0.5 \cdot s_c^i + 0.1 \cdot v), & \text{if } i \text{ is a fibroblast,} \\ \kappa_i = K_i \cdot s_c^i, & \text{if } i \text{ is a macrophage,} \end{cases} \tag{6.1.11}$$

where K_i is a positive constant. The mechanism in Equation (6.1.11) was not original in the model of strain energies [22], but was added in [12] to avoid the displacements caused by strain energies to dominate the displacements caused by chemotaxis.

For passive convections, the velocity is determined by the velocities as defined in the morphoelastic model (see Subsection 4.1.3 and Subsection 6.1.4).

If a fibroblast crosses the boundary of the computational domain, it is removed from the model and a new fibroblast is initiated at a random location on the opposite boundary.

6.1.2. Cell division, apoptosis and differentation

Cellular proliferation, apoptosis (programmed death) and differentiation are incorporated in the model. We assume that all phenotypes of cells are able to die, however, only regular fibroblasts are allowed to profliferate or to differentiate into myofibroblasts. The proliferation of macrophages and myofibroblasts is neglected. Furthermore, fibroblasts need to be matured sufficiently to proliferate or differentiate. A large number of cells in the domain will increase the apoptosis rate and decrease the proliferation rate. According to [12] and [16], we define the proliferation, differentiation and apoptosis rates by:

$$\lambda_p = \max\left(K_p \cdot c_\beta^2 - d_p \cdot (1.0 - 0.333 \cdot M_{col}), 0.0\right), \tag{6.1.12}$$

$$\lambda_{myo} = \begin{cases} \max\left(K_{myo} \cdot c_\beta^2(\boldsymbol{x}_f) + d_{myo} \cdot (1.0 - 0.962 \cdot M_{col}), 0.0\right), & \text{if } c_\beta > 1 \cdot 10^{-8}, \\ 0.0, & \text{if } c_\beta \leq 1 \cdot 10^{-8}, \end{cases} \tag{6.1.13}$$

$$\lambda_{a,f} = d_f \cdot (1.0 + 0.667 \cdot M_{col}), \tag{6.1.14}$$

$$\lambda_{a,m} = \frac{K_{mp}}{(c_P(\boldsymbol{x}_m) + 10^{-9})} + 0.667 \cdot d_f \cdot M_{col}, \tag{6.1.15}$$

where λ_p denotes the proliferation rate of fibroblasts, $\lambda_{a,f}$ is the apoptosis rate for fibroblasts (holding for both regular and myofibroblasts) and $\lambda_{a,m}$ is the apoptosis rate for macrophages, d_p, d_f and d_{mp} are parameters to fine-tune the proliferation rate and death rates, c_P and c_β are the concentrations of PDGF and TGF-β respectively, $\boldsymbol{x}_f$ and $\boldsymbol{x}_m$ are the locations of the cell center of the fibroblast and macrophage respectively. Furthermore, M_{col} denotes the collision energy experienced by the cell as defined in Equation (6.1.7), K_p, K_f and K_a are positive constants relating the rates to the collision energy, K_{myo} is a constant relating the differentation rate to the concentration of TGF-β. It is very difficult to balance the proliferation and apoptosis rates in such a way that the correct cell density is reached in the end. Therefore, the apoptosis rate is adapted slightly for special cases, to make sure the correct density of fibroblasts is reached again. At first, we define the average number of cells in the neighbourhood of a fibroblast, based on the normal cell density:

$$N_{need} = \pi r_n^2 \rho_{cell}, \tag{6.1.16}$$

where r_n is an effective radius around the fibroblast and ρ_{cell} denotes the fibroblasts density. Furthermore, the actual number of fibroblasts within a radius of r_n around the fibroblast is computed, which we will denote by N_{sur}. The adapted apoptosis rates are different for myofibroblasts and regular fibroblasts:

$$\lambda_{a,myof}^i = \begin{cases} \lambda_{a,f}(1.0 + A^i/43200), & \text{if } c_\beta < 10^{-9}, \\ \lambda_{a,f} \text{ if } c_\beta \geq 10^{-9}, & \text{if } c_\beta \geq 10^{-9}, \end{cases} \tag{6.1.17}$$

where $\lambda^i_{a,myof}$ denotes the apoptotis rate of myofibroblast i and A^i denotes the age of myofibroblasts i. In this way, it is reassured that all the myofibroblasts die soon after the concentration of TGF-β drops. Furthermore,

$$\lambda_{a,reg.f} = \begin{cases} \lambda_{a,f} \cdot \frac{N_{sur}}{N_{need}}, & \text{if } c_\beta < 10^{-9} \text{ and } N_{sur} \geq N_{need}, \\ \lambda_{a,f}, & \text{if } c_\beta \geq 10^{-9} \text{ and } N_{sur} \geq N_{need}, \\ 0.0, & \text{if } N_{sur} < N_{need}. \end{cases} \tag{6.1.18}$$

According to the exponential distribution, the probability with given parameter λ is determined by:

$$\mathbb{P}(E_i^k) = 1.0 - \exp(-\lambda_E \cdot \Delta t), \tag{6.1.19}$$

where Δt is the time step and E_i^k denotes the event that cell i proliferates, dies or differentiates at iteration k. A random number $\zeta \in (0,1)$ will be generated, and the event E_i^k only takes place if $\zeta < \mathbb{P}(E_i^k)$.

If the concentration of TGF-β is large enough, additional fibroblasts are initiated at the boundary of the computational domain. A Poisson distribution with parameter $\beta_f \cdot c_\beta \cdot l \cdot \Delta t$ is used to determine how many macrophages enter the wound at each time step. Here, l denotes the perimeter of the domain and β_f a positive constant. Fibroblasts only enter the domain if the TGF-β concentration transcends a threshold value β_f^{min}.

6.1.3. Concentration of chemokines

The concentration of PDGF and TGF-β is determined by the following transport-reaction equations, respectively ([12]):

$$(IBVP_P) = \begin{cases} \frac{\partial c_P}{\partial t} - D_P \Delta c_P = 0, & \boldsymbol{x} \in \Omega, t > 0, \\ D_P \frac{\partial c_P}{\partial \boldsymbol{n}} + K c_P = 0, & \boldsymbol{x} \in \partial\Omega, t > 0, \\ c_P(\boldsymbol{x}, 0) = c_P^0(\boldsymbol{x}), & \boldsymbol{x} \in \Omega. \end{cases}$$

and

$$(IBVP_\beta) = \begin{cases} \frac{\partial c_\beta}{\partial t} - D_\beta \Delta c_\beta = s(\boldsymbol{x}, t), & \boldsymbol{x} \in \Omega, t > 0, \\ D_\beta \frac{\partial c_\beta}{\partial \boldsymbol{n}} + K c_\beta = 0, & \boldsymbol{x} \in \partial\Omega, t > 0, \\ c_\beta(\boldsymbol{x}, 0) = 0, & \boldsymbol{x} \in \Omega, \end{cases}$$

where c_P and c_β denote the concentrations of PDGF and TGF-β respectively, D_P and D_β are the corresponding diffusion parameters and K is the rate with which the molecules leave the domain. Since TGF-β is secreted by macrophages, the source term $s(\boldsymbol{x})$ is a function of the position of macrophages:

$$s(\boldsymbol{x}, t) = \kappa_\beta \sum_{i=1}^{N_m(t)} \delta(\boldsymbol{x} - \boldsymbol{x}_i(t)), \tag{6.1.20}$$

where κ_β is the magnitude of secreted TGF-β by one cell per second, N_m denotes the number of macrophages at time t and $\boldsymbol{x}_i(t)$ is the location of the center of cell i at time t.

6.1.4. Wound contraction

In order to compute wound contractions caused by cellular traction forces, the morphoelastic model as defined in Chapter 5 is used. It has been widely documented that myofibroblasts play an important role in wound healing and contraction [16]. Since myofibroblasts exert much stronger traction forces, P (as defined in Equation (5.1.1)) is set to be twice as large as the traction force for regular fibroblasts [1]. Hence, the initial

boundary value problem modelling the contraction of the wound becomes:

$$(IBVP_8): \begin{cases} \frac{\mathrm{D}(\rho \boldsymbol{v})}{\mathrm{D}t} + \boldsymbol{v}\rho(\nabla \cdot \boldsymbol{v}) = \nabla \cdot \underline{\underline{\sigma}} + \boldsymbol{f}, & \boldsymbol{x} \in \Omega, t > 0, \\ \underline{\underline{\sigma}} = \frac{\mu_1}{2}\left(\nabla \boldsymbol{v} + (\nabla \boldsymbol{v})^T\right) + \mu_2 (\nabla \cdot \boldsymbol{v})\, \underline{\underline{I}} + \frac{E_s\sqrt{\rho}}{1+\eta}\left(\underline{\underline{\varepsilon}} + \frac{\eta}{1-2\eta}\mathrm{Tr}(\underline{\underline{\varepsilon}})\underline{\underline{I}}\right), & \boldsymbol{x} \in \Omega, t > 0, \\ \frac{\mathrm{D}\underline{\underline{\varepsilon}}}{\mathrm{D}t} + \underline{\underline{\varepsilon}}\ \mathrm{skew}\left(\frac{\partial \boldsymbol{v}}{\partial \boldsymbol{x}}\right) - \mathrm{skew}\left(\frac{\partial \boldsymbol{v}}{\partial \boldsymbol{x}}\right)\underline{\underline{\varepsilon}} + \left(\mathrm{Tr}\left(\underline{\underline{\varepsilon}}\right) - 1\right)\ \mathrm{sym}\left(\frac{\partial \boldsymbol{v}}{\partial \boldsymbol{x}}\right) = -\underline{\underline{g}}, & \boldsymbol{x} \in \Omega, t > 0, \\ \underline{\underline{\sigma}} \cdot \boldsymbol{n} + a\boldsymbol{u} = \boldsymbol{0} \quad , & \boldsymbol{x} \in \partial\Omega, t > 0, \\ \boldsymbol{u}(\boldsymbol{x}, 0) = \boldsymbol{0}, & \boldsymbol{x} \in \Omega, \\ \boldsymbol{v}(\boldsymbol{x}, 0) = \boldsymbol{0}, & \boldsymbol{x} \in \Omega. \end{cases}$$

where

$$\begin{aligned} \boldsymbol{f}(\boldsymbol{x}, t) &= \sum_{i=1}^{N_f(t)} \sum_{j=1}^{N_S^i} P_f \boldsymbol{n}_j(\boldsymbol{x}, t)\delta(\boldsymbol{x} - \boldsymbol{x}_j(t))\Delta\Gamma_{i,j} \\ &+ \sum_{i=1}^{N_{myo}(t)} \sum_{j=1}^{N_S^i} P_{myo} \boldsymbol{n}_j(\boldsymbol{x}, t)\delta(\boldsymbol{x} - \boldsymbol{x}_j(t))\Delta\Gamma_{i,j}, \end{aligned} \tag{6.1.21}$$

where $N_f(t)$ is the number of fibroblasts at time t, $N_{myo}(t)$ is the number of myofibroblasts at time t, P_f and P_{myo} is the magnitude of traction force per space unit for fibroblasts and myofibroblasts respectively, N_S^i is the number of segments with which the cell boundary of cell i is modelled (see Section 5.1), $\boldsymbol{n}_j$ is the inward pointing unit normal vector of cell boundary segment j, $\boldsymbol{x}_j(t)$ is the midpoint of segment j and $\Delta\Gamma_{i,j}$ is the length of line segment j of cell i.

In Section 5.1, $N_S = 4$ chosen, (i.e. the curve modelling the cell boundary is a square). However, according to [15], using $N_S = 3$ would decrease the computational cost while it would not harm the accuracy of the results. Hence, in this model $N_S = 3$ is used. The orientation of the segments is determined randomly for every (myo)fibroblast.

6.1.5. Initial settings of the model

The initial number of fibroblasts is determined on the basis of an initial density of fibroblasts. The fibroblasts are randomly distributed over the non-wounded area. Furthermore, at $t = 0$, there are no macrophages in the domain. A Poisson distribution with parameter $\beta_{mp} \cdot c_P \cdot l \cdot \Delta t$ is used to determine how many macrophages enter the wound at each time step. Here, l denotes the perimeter of the wound and β_{mp} a positive constant. Macrophages only enter the wound if the PDGF concentration transcends a threshold value β_{mp}^{min}. The initial concentration of PDGF is set with the function $c_P^0(\boldsymbol{x})$, which is defined in such a way that the concentration is high in the wound area and (almost) zero in the non-wounded area, with a smooth transition at the wound boundary [12]. The initial concentration of TGF-β is set to zero. The initial domain is a square with side length L_d. The wound is modelled to be a square in the center of the domain with side length $L_w = 0.2 \cdot L_d$.

6.2. Simulation results

In this section, the numerical results are shown for the model in Section 6.1. The parameter values used in the simulations are shown in Table 6.1. All the used units are now SI base units.

In Figures 6.1 - 6.6, the state of the domain is shown for several moments in time. The boundary of the wound is indicated in the red. The initial boundary of the wound is indicated by black. The red dots are macrophages, the blue dots are regular fibroblasts and the black dots are myofibroblasts.

Figure 6.1 displays the intital condition of the model, as it is describe in Subsection **??**.

After 7 hours and 12 minutes (0.3 days, Figure 6.2), macrophages triggered by the high gradients of PDGF, are entering the wound. Since macrophages come from the injured vessels, we assumed that they enter the wound via the edge between injured and uninjured region. Furthermore, the macrophages immediately start to secrete TGF-β, causing the TGF-β concentration to increase.

At $t = 3$ days (Figure 6.3), the macrophages have migrated further towards the center of the wound. In the meantime, the concentration of PDGF has been decreasing in the wound by diffusion. Hence, the entry of macrophages has stopped, since the PDGF concentration does not exceed the lower limit anymore. More

Description	**Parameter**	**Value**	**Unit**
Length of the domain in x-direction	Lx	$1.5 \cdot 10^{-3}$	m
Length of the domain in y-direction	Ly	$1.5 \cdot 10^{-3}$	m
Length of the wound in x-direction	Bx	$6.708 \cdot 10^{-4}$	m
Length of the wound in y-direction	By	$6.708 \cdot 10^{-4}$	m
Number of nodes in x-direction	nX	31	-
Number of nodes in y-direction	nY	31	-
Time step	Δt	2592	s
Radius of the triangle-shaped curve around cells	r_s	$5.387 \cdot 10^{-6}$	m
Substrate Elasticity (Young's modulus)	E_s	$1 \cdot 10^{3}$	$\mathrm{N \cdot m^{-2}}$
Density	ρ	$5 \cdot 10^{3}$	$\mathrm{g \cdot m^{-3}}$
Shear viscosity	μ_1	$1 \cdot 10^{4}$	$\mathrm{N \cdot s \cdot m^{-2}}$
Bulk viscosity	μ_2	$1 \cdot 10^{4}$	$\mathrm{N \cdot s \cdot m^{-2}}$
Poisson's ratio	η	0.48	-
Degree of permanent deformation	ξ	$1 \cdot 10^{-6}$	-
Spring constant in $(IVBP_8)$	a	$1 \cdot 10^{-4}$	-
Magnitude of point forces (regular fibroblasts)	P_f	0.2	N
Magnitude of point forces (myofibroblasts)	P_{myo}	0.8	N
Duration of simulated time	T	28	day
Cell radius	R	$2 \cdot 10^{-6}$	m
Cell Elasticity	E_c	60	$\mathrm{kg \cdot m^{-1} \cdot s^{-2}}$
Basic strain energy of cells	M^0	8.144	$\mathrm{kg \cdot m^{-1} \cdot s^{-2}}$
Maximal detectable range (for all cells)	d_i	$29.5 \cdot 10^{-6}$	m
Strain energy constant	K_i	$4.0 \cdot 10^{-14}$	$\mathrm{m \cdot s^3 \cdot kg^{-2}}$
Detection range of cells	d	$2.95 \cdot 10^{-5}$	m
Diffusion rate PDGF	D_P	$2.3 \cdot 10^{-12}$	$\mathrm{m^2 \cdot s^{-1}}$
Diffusion rate TGF-β	D_β	$2.3 \cdot 10^{-11}$	$\mathrm{m^2 \cdot s^{-1}}$
Constant in Robin bnd. condition in $(IBVP_P)$ and $(IBVP_\beta)$	K	10^{3}	$\mathrm{m^{-1}}$
Diffusion parameter for random walk	D	$9 \cdot 10^{-18}$	$\mathrm{m^2 \cdot s^{-1}}$
Magnitude of TGF-β secretion	κ_β	$6.246 \cdot 10^{-20}$	$\mathrm{kg \cdot s^{-1} cell^{-1}}$
Maximal initial concentration of PDGF	c^w	10^{-5}	$\mathrm{kg \cdot m^{-3}}$
TGF-β dependent proliferation rate of fibroblasts	K_p	$8.8659 \cdot 10^{4}$	-
TGF-β independent proliferation rate of fibroblasts	d_p	$8.02 \cdot 10^{-7}$	-
TGF-β dependent differentation rate of fibroblasts	K_{myo}	$0.4 \cdot 10^{7}$	-
TGF-β independent differentation rate of fibroblasts	d_{myo}	$1 \cdot 10^{-3}$	-
Apoptosis rate of fibroblasts and macrophages	d_f	$4.01 \cdot 10^{-7}$	-
PDGF dependent apoptosis rate of macrophages	K_{mp}	$5.57 \cdot 10^{-14}$	-
Receptor unbinding rate	d^u	$2.78 \cdot 10^{-4}$	$\mathrm{s^{-1}}$
Receptor binding rate of fibrobalsts	d^b	$1.39 \cdot 10^{2}$	$\mathrm{m^3 \cdot kg^{-1} \cdot s^{-1}}$
Chemotaxis constant of fibroblasts	ν_f	$1.2 \cdot 10^{-6}$	$\mathrm{m \cdot s^{-1}}$
Chemotaxis constant of macrophages	ν_{mp}	$1.0 \cdot 10^{-8}$	$\mathrm{m \cdot s^{-1}}$
Threshold value for entry of fibroblasts in domain	β_f^{min}	$3.0 \cdot 10^{-10}$	$\mathrm{kg \cdot m^{-3}}$
Constant for entry of fibroblasts in domain	β_f	$3.5 \cdot 10^{-5}$	$\mathrm{m^2 \cdot kg^{-1} \cdot s^{-1}}$
Threshold value for entry of macrophages in wound	β_{mp}^{min}	$3.33 \cdot 10^{-9}$	$\mathrm{kg \cdot m^{-3}}$
Constant for entry of macrophages in wound	β_{mp}	$1.67 \cdot 10^{5}$	$\mathrm{m^2 \cdot kg^{-1} \cdot s^{-1}}$

Table 6.1: Overview of used parameters in Section 6.2

TGF-β is secreted by the macrophages, causing fibroblasts migrating into the wound and proliferating. More importantly, differentiation from fibroblasts to myofibroblasts is induced. The wound starts to deform as a result of the large number of fibroblasts in the wound which exert traction forces.

After 4.5 days (Figure 6.4), the number of (myo)fibroblasts has increased further and the wound is more contracted. The fibroblasts are clumping together in the direct neighbourhood of the macrophages by chemotaxis. This effect is increased by the contraction of the skin. In addition, the number of macrophages is decreasing by apoptosis, resulting in the TGF-β concentrations dropping.

At $t = 6$ days (Figure 6.5), all macrophages are dead and the concentration of TGF-β is very low. Hence, the proliferation rate of fibroblasts decreases, differentiation has stopped and the apoptosis rate increases. This causes the number of (myo)fibroblasts to decrease gradually.

After 12 days (Figure 6.6), the cell density is average again and most myofibroblasts have died. Furthermore, the wound area has recovered partially. However, because of morphoelasticity, the wound will not recover completely.

To measure the degree of contraction of the wound, the (relative) wound area is an important index. In Figure 6.7, the relative wound area is shown as a function of time. Initially, the wound area increases a little bit, because the fibroblasts are initially in the uninjured region and in the simulation, the wound is surrounded by the healthy skin. After a while, the wound area decreases rapidly by the larger number of fibroblasts in the wound. As the number of fibroblasts decreases again, the wound area increases again, until a dynamic equilibrium is reached.

In Figure 6.8, the number of several phenotypes of cells is illustrated against time. At first, the number of macrophages increases. Subsequently, the number of (myo)fibroblasts increases rapidly. As the macrophages are dead, the number of (myo)fibroblasts decreases again. Eventually, all myofibroblasts are dead and the number of regular fibroblasts is stable again, although it is slightly more than it is initially, because the gap at the wound area is filled with fibroblasts now. In Figure 6.9, the number of macrophages against time is illustrated separately to make the differences clearly visible.

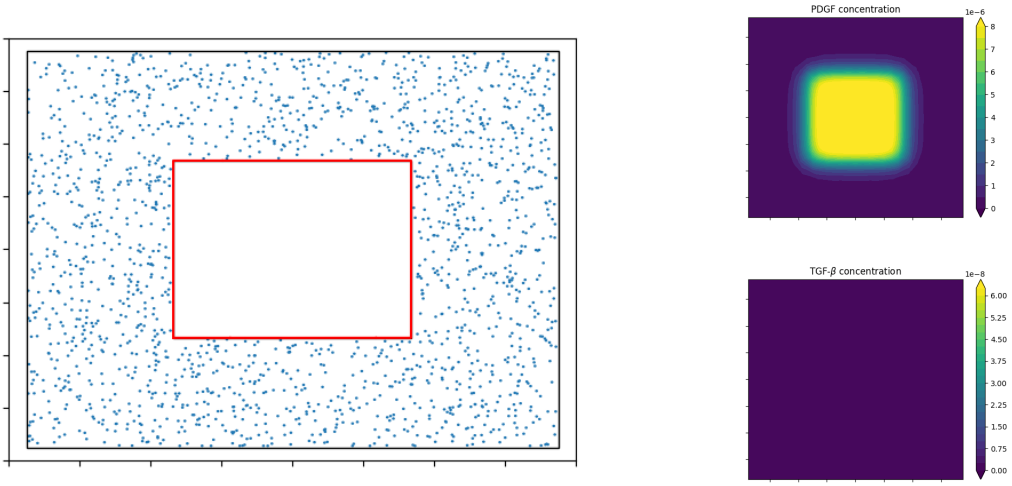

Figure 6.1: State of the domain at $t = 0$ days

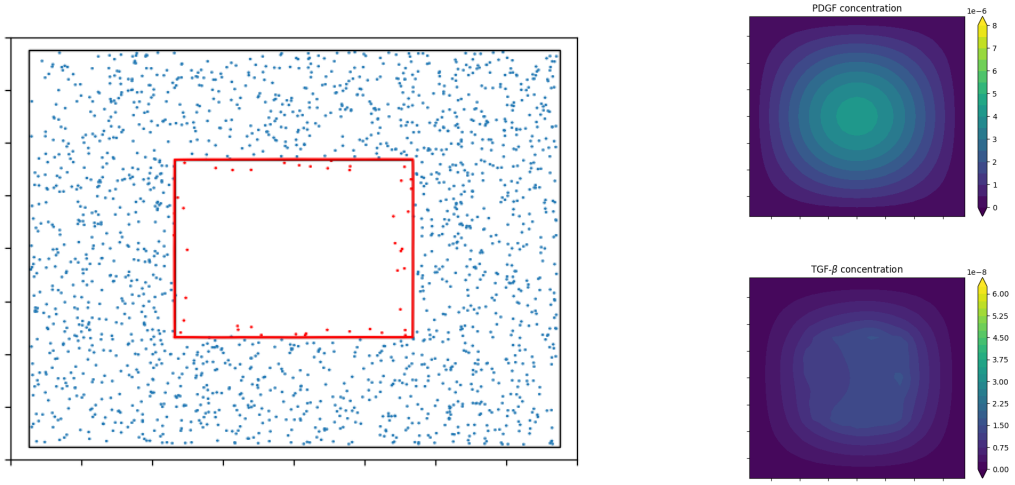

Figure 6.2: State of the domain at $t = 0.3$ days

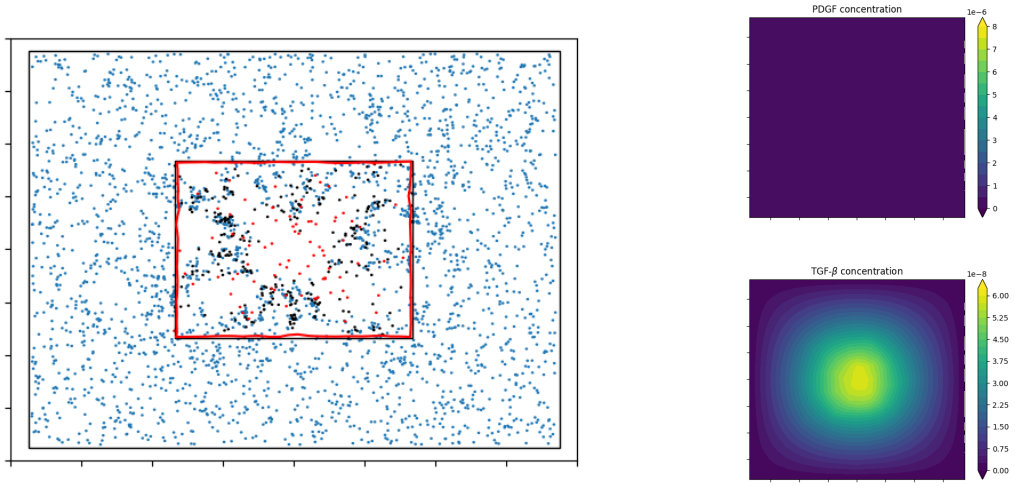

Figure 6.3: State of the domain at $t = 3$ days

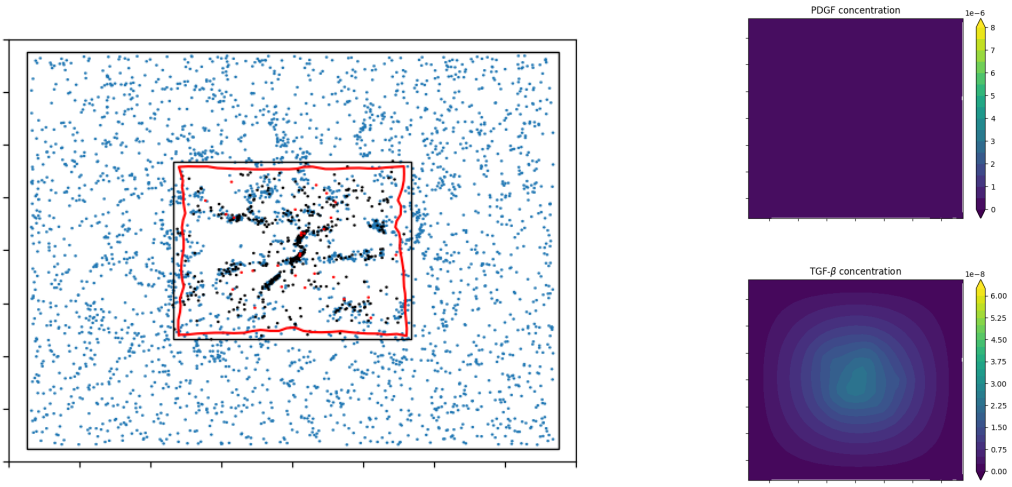

Figure 6.4: State of the domain at $t = 4.5$ days

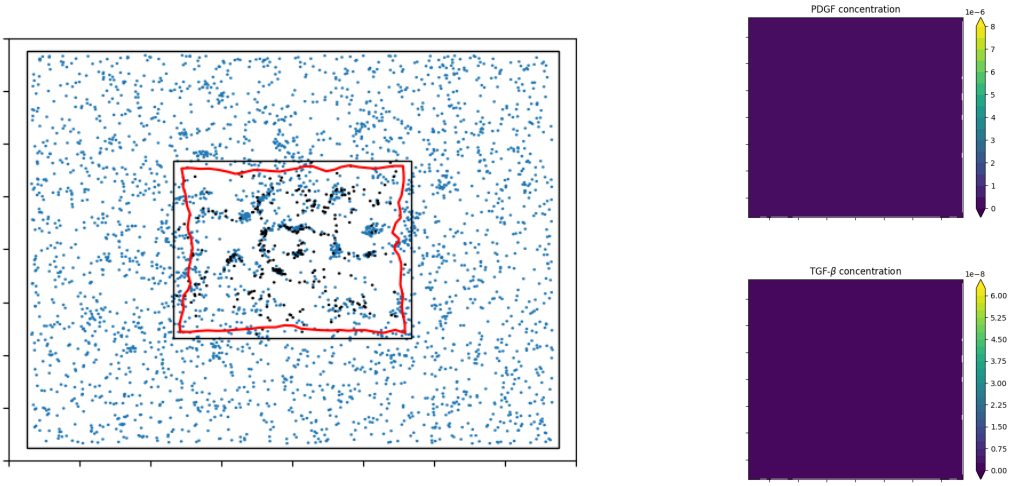

Figure 6.5: State of the domain at $t = 6$ days

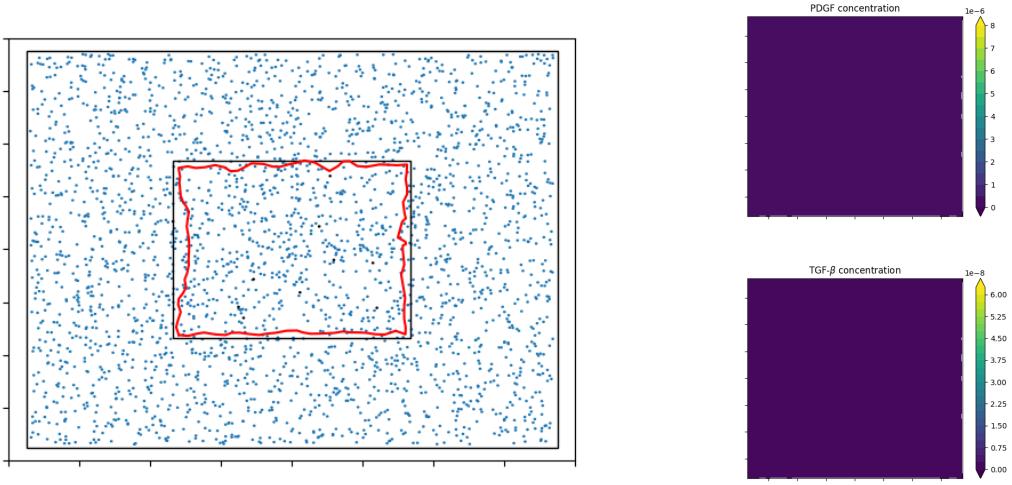

Figure 6.6: State of the domain at $t = 12$ days

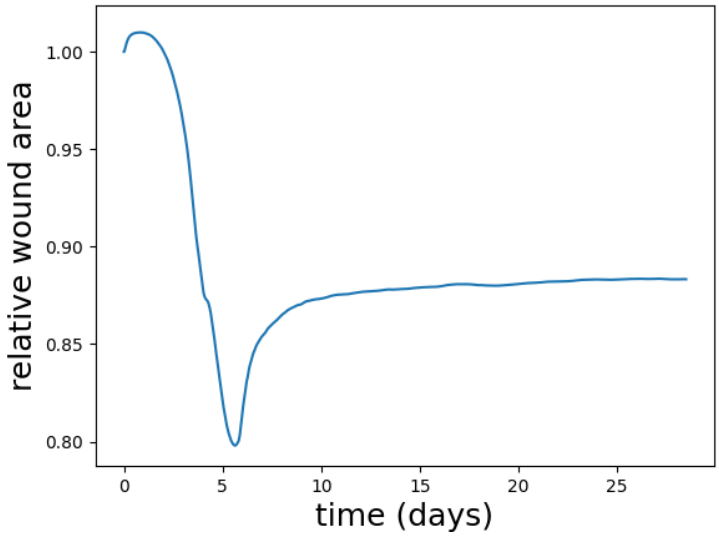

Figure 6.7: Relative wound area against time

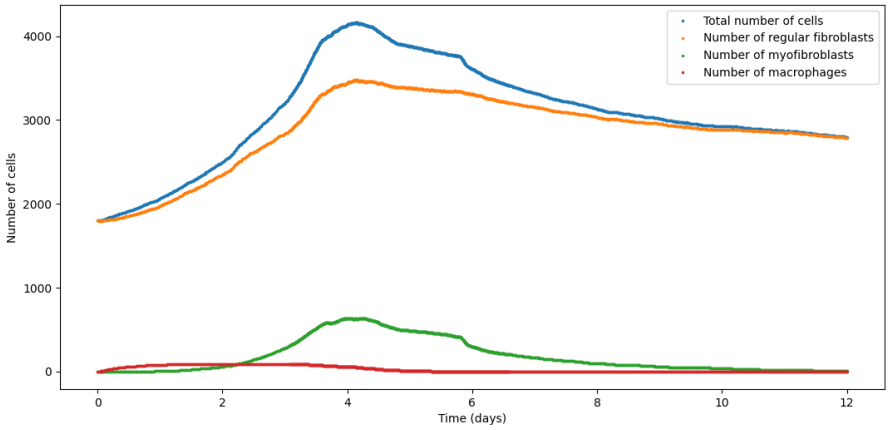

Figure 6.8: Number of cells against time. Blue indicates the total number of cells, orange indicates the number of regular fibroblasts, green indicates the number of myofibroblasts and red indicates the number of macrophages.

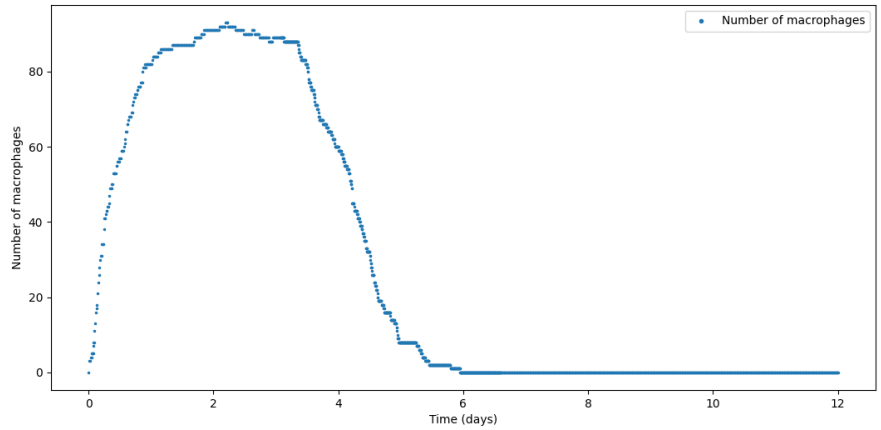

Figure 6.9: Number of macrophages against time

6.3. Monte Carlo simulations

The model described in Section 6.1 contains many input parameters. Several of these parameters are not exactly measured in the laboratory experiments, or differ from case to case. To investigate relations between input parameters and output parameters or between output parameters mutually, Monte Carlo simulations were carried out. Six input parameters were chosen to be varied in these simulations. For each simulation, the values of these parameters were determined randomly by a uniform distribution over a certain interval. The varied parameters were: Substrate Elasticity, Magnitude of Point Forces, Viscosity, Apoptosis Rate, Proliferation Rate and Differentiation Rate. In Table 6.2, the uniform distributions of the variables are displayed. The magnitude of point forces P_f of regular fibroblasts and the magnitude of point forces P_{myo} of myofibroblasts were varied simultaneously by letting P_{myo} be defined as $P_{myo} := 4 \cdot P_f$, similarly to Section 6.2. The shear viscosity and bulk viscosity were varied simultaneously: $\mu_1 = \mu_2 =: \mu$. As for the Apoptosis Rate, only d_f was varied, while d_{mp} was fixed. Furthermore, K_p and d_p, the proliferation rates, were varied simultaneously. A variation factor A_p was added for the simultaneous variation of K_p and d_p:

$$K_p = A_p \cdot K_p^0 \text{ and } d_p = A_p \cdot d_p^0,$$

where K_p^0 and d_p^0 were defined as in Table 6.1. As for the differentiation rates K_{myo} and d_{myo}, this was done analogously with a factor A_{myo}. All the other input parameters were defined as in Table 6.1.

The following quantities were considered as output parameters: the relative area of the wound at $t = 3.5$ days, the minimal relative area of the wound, the final relative area of the wound, the moment at which the minimal area is reached and the moment at which the final area is reached. A strictly final wound area does not exist, since there always remain some small fluctuations in the area, even when the situation is apparently stable. This is due to small movements of the fibroblasts by strain energies and random walk. Hence, the final area is defined by the following steps:

1. Define $M = 1.0 - A_{min}^{rel}$, where A_{min}^{rel} is the minimal relative wound area. The quantity M can be viewed as the maximal shrinkage of the wound.
2. If $|A_{k_0} - A_{k_0-1}| < 0.03 \cdot \Delta t^{k_0} \cdot M$, where A_{k_0} denotes the relative wound area at iteration k_0 and Δt^{k_0} is the time step at iteration k_0, then a test is started at iteration k_0.
3. For iteration $k > k_0$, if $|A_k - A_{k_0}| \leq 0.03 \cdot M$, the test continues. If $|A_k - A_{k_0}| > 0.03 \cdot M$, then the test failed and it is interrupted. A new test is then started at iteration k, that is, $k_0 := k$.
4. If $t^{k_1} - t^{k_0} \geq 2.0$ days and for all iterations k such that $k_0 < k \leq k_1$, the condition in item (3) is satisfied, then the following is checked: define the average relative wound area as $A_{av} := \frac{\sum_{k=k_0}^{k_1} A_k}{k_1 - k_0}$. If for all $k_0 \leq k < k_1$, the condition $|A_k - A_{av}| \leq 0.03 \cdot \Delta t^k \cdot M$ is satisfied, the test is passed and the moment of the final relative wound area is set to be t^{k_1} and the value is set to be A_{k_1}.

This procedure means that the final wound area is defined to be reached as soon as the fluctuations of the area are less than 6% of the maximal shrinkage of the wound.

Description	**Parameter**	**Interval**	**Unit**
Substrate Elasticity (Young's modulus)	E_s	$[1 \cdot 10^2, 5 \cdot 10^3]$	$\text{N}\cdot\text{m}^{-2}$
Viscosity	μ	$[1 \cdot 10^3, 1 \cdot 10^5]$	$\text{N}\cdot\text{s}\cdot\text{m}^{-2}$
Magnitude of point forces (regular fibroblasts)	P_f	$[0.1, 0.4]$	N
Magnitude of point forces (myofibroblasts)	P_{myo}	$[0.4, 0.16]$	N
Apoptosis rate of fibroblasts and macrophages	d_f	$[1.20 \cdot 10^{-7}, 6.82 \cdot 10^{-7}$	-
Variation factor for Proliferation rate	A_p	$[0.3, 1.7]$	-
Variation factor for Differentiation rate	A_{myo}	$[0.3, 1.7]$	-

Table 6.2: Overview of used parameters in Section 6.2

In Figure 6.10, the relations between the relative area at $t = 3.5$ days, the minimal area and the final area are shown. It appears that the parameters have a strongly linear relationship to each other. This means that the condition of the wound in an early phase, is a strong indicator for the condition of the wound in a later phase.

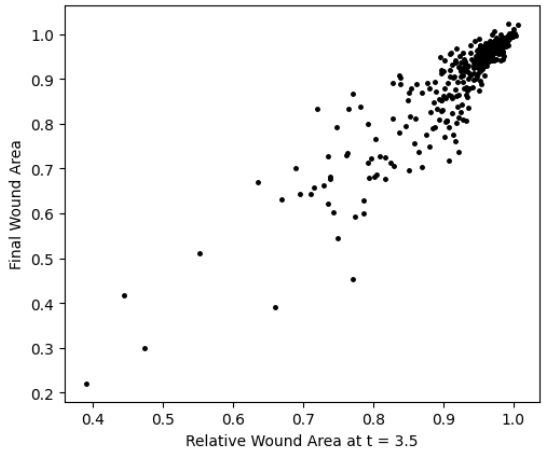

A. Area at 3.5 days against Minimal Area

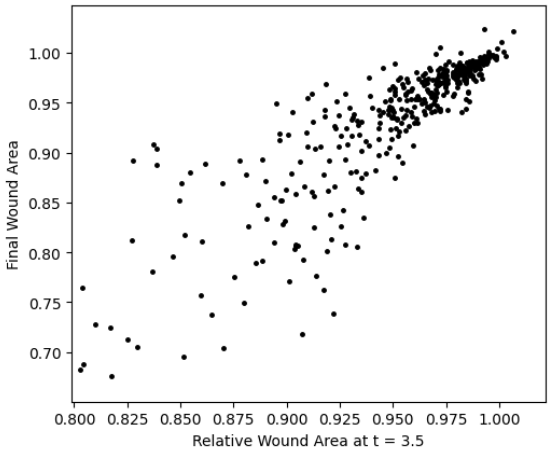

B. Area at 3.5 days against Minimal Area (zoomed)

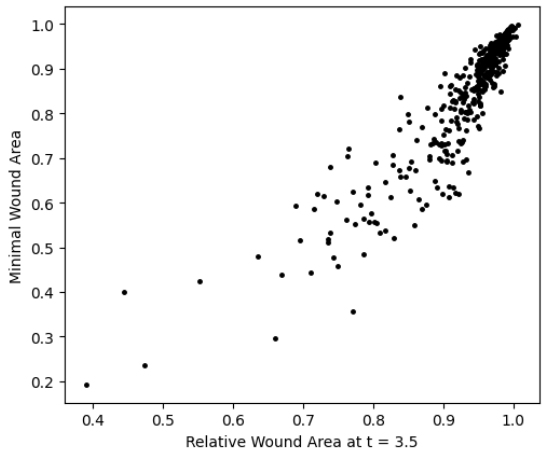

C. Area at 3.5 days against Final Area

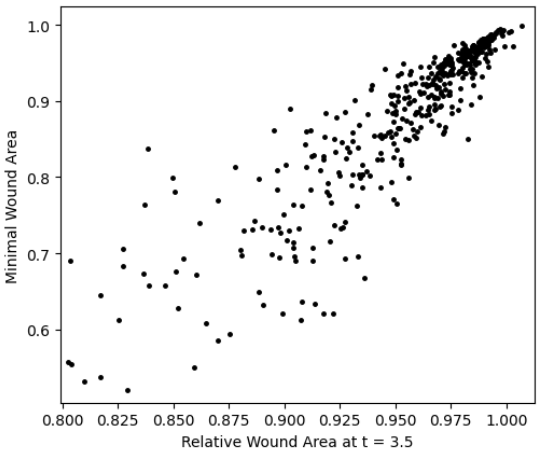

D. Area at 3.5 days against Final Area (zoomed)

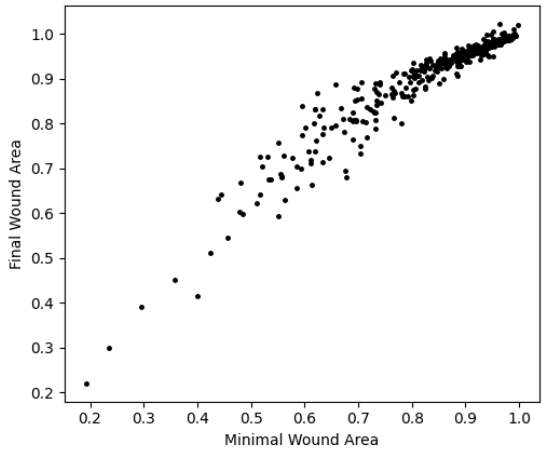

E. Minimal Area against Final Area

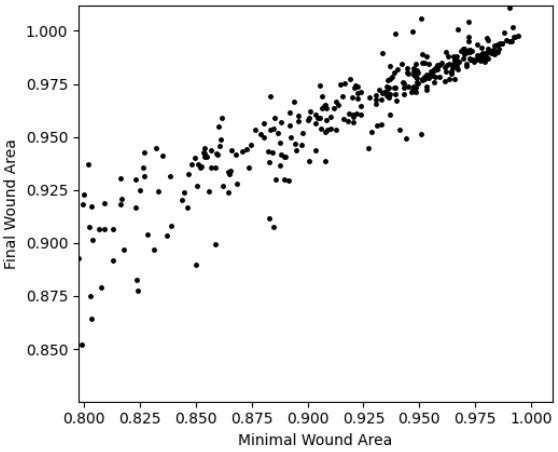

F. Minimal Area against Final Area (zoomed)

Figure 6.10: Scatter plots of relative wound area at different moments

Table 6.3 presents the Pearson correlation coefficients for the parameters in Figure 6.10. All the correlations are larger than 0.9, which indicates a strong linearity in the data. Furthermore, the p-values, are of order 10^{-3} or smaller.

	Area at $t = 3.5$ days	**Minimal Area**	**Final Area**
Area at $t = 3.5$ days	1.0	0.904055	0.918347
Minimal Area	0.904055	1.0	0.955016
Final Area	0.918347	0.955016	1.0

Table 6.3: Pearson Correlation Matrix for wound area at three moments

7

Implementation and Programming Work on Agent-Based Model

One of the long-term objectives of this project is to develop an efficient software, so that the model can produce the results in a few minutes. In this chapter, the implementation and improvement of the computational perspective are discussed. We compared the computational cost for different programming languages as well.

7.1. Implementation of Agent-Based Model

7.1.1. Structure of the code

The agent-based model [12] was implemented in C++. The code was available during this thesis project for the model in Chapter 6. The code consisted of mainly two classes, named 'Scenario' and 'FEM'. In 'FEM', the Finite Element computations are carried out and in 'Scenario', which uses 'FEM', the other aspects of the model are implemented.

The purely elastic, viscoelastic and morphoelastic models in Chapters 3 and 4 were at first implemented in Python and subsequently implemented in C++. The results of the Python code and the C++-code were compared with each other, to confirm that there are no implementational errors. In C++, the implementation consisted of a class 'Elasticity' using two subclasses: 'FEM-elast' for pure elasticity and viscoelasticity and 'FEM-morpho' for morphoelasticity. For the final model in Chapter 6, a class 'ElastScen' (in which 'Elasticity' and 'Scenario' were combined) was constructed. In this class, the general computations are carried out, while the Finite Elements parts are carried out in FEM and FEM-morpho.

A user-friendly API in Python already existed for the model [12]. It is suitable for users to run simulations with the option to insert some parameters and to visualize the results. This API was extended to make it suitable for the new model.

7.1.2. Moving mesh

In the implementation, a moving mesh is used, which is the easiest way to solve the differential equations, since they are formulated in an Eulerian framework. Furthermore, the mesh that is used is a structured mesh (see Figure 7.1).

An advantage of this mesh is the structured numbering, which made it possible to write some algorithms to make the computations more efficient (see Subsection 7.1.3). A disadvantage of the structured mesh is the fact that the angles of the triangles are not optimal. For an optimal situation, all the angles should be as close as possible to $\frac{1}{3}\pi$. However, in the structured mesh one angles is $\frac{1}{2}\pi$ and two angles are $\frac{1}{4}\pi$. As the nodal points are going to move as a consequence of displacements, the triangles can easily become ill-shaped in the sense of very obtuse or acute angles, as it is shown in Figure 7.2. Therefore, we developed an algorithm to remesh the domain. This means that new nodal points are chosen, and that the values of the several quantities in the model at node i are approximated by linear interpolation:

$$q(\boldsymbol{x}_i^N, t) \approx \sum_{j \in \{p_i^1, p_i^2, p_i^3\}} q(\boldsymbol{x}_j^O, t) \phi_j^O(\boldsymbol{x}_i^N), \tag{7.1.1}$$

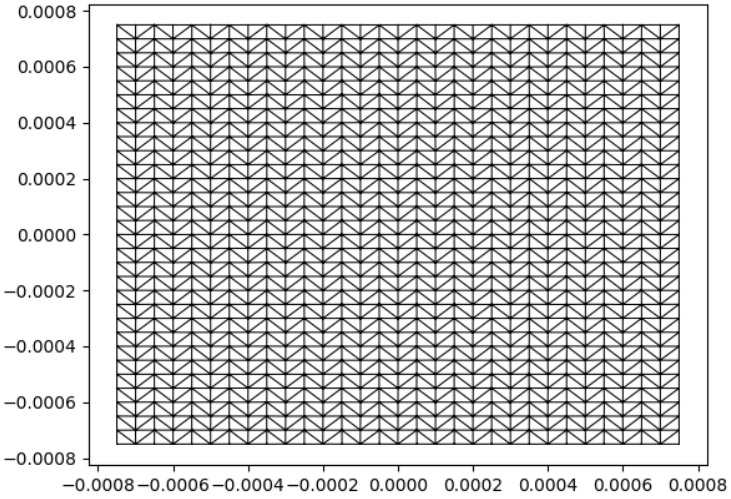

Figure 7.1: Structured mesh which was used for the Finite Element computations, $t = 0$

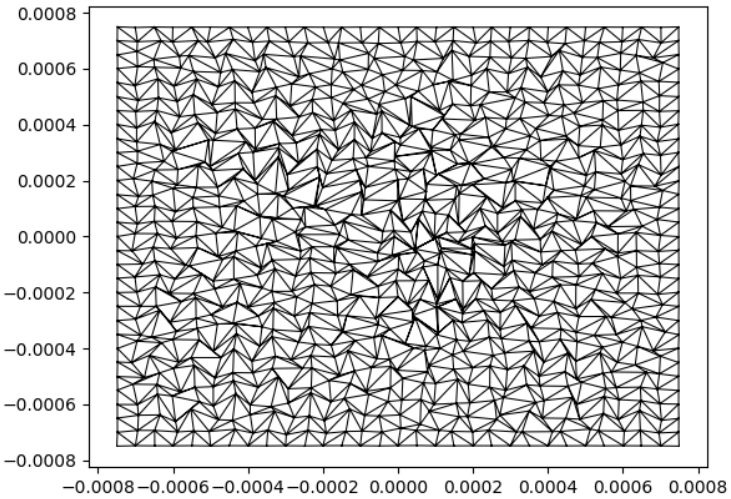

Figure 7.2: Deformed mesh with several ill-shaped triangles

where $\boldsymbol{x}_i^N$ denotes the coordinates of node i in the new mesh, $\boldsymbol{x}_j^O$ denotes the coordinates of node j in the old mesh and ϕ_j^O is the test function belonging to node j in the old mesh. Furthermore, p_i^1, p_i^2 and p_i^3 are the nodes of the triangle in the old mesh which contains $\boldsymbol{x}_i^N$ and q denotes a certain quantity in the model (for example concentration of a certain chemokine). Besides for remeshing, this method is also used to approximate the values of quantities at the location of cells if necessary:

$$q(\boldsymbol{x}_c, t) \approx \sum_{j \in \{p_c^1, p_c^2, p_c^3\}} q(\boldsymbol{x}_j, t)\phi_j(\boldsymbol{x}_c), \tag{7.1.2}$$

where $\boldsymbol{x}_c$ denotes the location of the cell center.

To determine whether remeshing is necessary at a certain time step, an angle criterion was set. We define θ_{min} to be the minimal allowed angle and θ_{max} to be the maximal allowed angle. If all angles in the mesh at time t are larger than θ_{min} and smaller than θ_{max}, then the angle criterion is satisfied. Otherwise, a remesh is carried out.

Let $\{\boldsymbol{x}_1, \boldsymbol{x}_2, \boldsymbol{x}_3\}$ denote the nodal points of a triangular mesh element $e_k \in \Omega(t) \subset \mathbb{R}^2$ with corresponding angles θ_1, θ_2 and θ_3. Let ϕ_i ($i \in \{1,2,3\}$) be piecewise linear basis functions with $\phi_i(\boldsymbol{x}) := \alpha_i + \beta_i x + \gamma_i y$ such that $\phi_i(\boldsymbol{x}_j) = \delta_{ij}$, where δ_{ij} is defined as in Equation (3.3.6). Then we have

$$\cos\theta_3 = -\frac{\langle \boldsymbol{\omega}_1, \boldsymbol{\omega}_2 \rangle}{||\boldsymbol{\omega}_1|| \cdot ||\boldsymbol{\omega}_2||}, \tag{7.1.3}$$

where

$$\boldsymbol{\omega}_i := \begin{pmatrix} \beta_i \\ \gamma_i \end{pmatrix},$$

and $\langle ., . \rangle$ denotes the vectorial dot product in $\mathbb{R}^2$. Analogously,

$$\cos\theta_2 = -\frac{\langle \boldsymbol{\omega}_1, \boldsymbol{\omega}_3 \rangle}{||\boldsymbol{\omega}_1|| \cdot ||\boldsymbol{\omega}_3||}, \tag{7.1.4}$$

and

$$\cos\theta_1 = -\frac{\langle \boldsymbol{\omega}_2, \boldsymbol{\omega}_3 \rangle}{||\boldsymbol{\omega}_2|| \cdot ||\boldsymbol{\omega}_3||}, \tag{7.1.5}$$

Proof. We define

$$\boldsymbol{z}_1 := \boldsymbol{x}_1 - \boldsymbol{x}_3 \quad \text{and} \quad \boldsymbol{z}_2 := \boldsymbol{x}_2 - \boldsymbol{x}_3.$$

Then

$$\cos\,\theta_3 = \frac{\langle \boldsymbol{z}_1, \boldsymbol{z}_2 \rangle}{||\boldsymbol{z}_1|| \cdot ||\boldsymbol{z}_2||}.$$

Furthermore, since $\phi_i(\boldsymbol{x}_j) = \delta_{ij}$ ($i, j \in \{1,2,3\}$), we have

$$\begin{aligned} \langle \boldsymbol{\omega}_1, \boldsymbol{z}_1 \rangle &= \beta_1(x_1 - x_3) + \gamma_1(y_1 - y_3) \\ &= \alpha_1 + \beta_1 x_1 + \gamma_1 y_1 - \big(\alpha_1 + \beta_1 x_3 + \gamma_1 y_3\big) \\ &= \phi_1(\boldsymbol{x}_1) - \phi_1(\boldsymbol{x}_3) = 1 - 0 \\ &= 1, \end{aligned} \tag{7.1.6}$$

and

$$\begin{aligned} \langle \boldsymbol{\omega}_1, \boldsymbol{z}_2 \rangle &= \beta_1(x_2 - x_3) + \gamma_1(y_2 - y_3) \\ &= \alpha_1 + \beta_1 x_2 + \gamma_1 y_2 - \big(\alpha_1 + \beta_1 x_3 + \gamma_1 y_3\big) \\ &= \phi_1(\boldsymbol{x}_2) - \phi_1(\boldsymbol{x}_3) = 0 - 0 \\ &= 0. \end{aligned} \tag{7.1.7}$$

Analogously, we can show

$$\langle \boldsymbol{\omega}_2, \boldsymbol{z}_2 \rangle = 1, \tag{7.1.8}$$

and

$$\langle \boldsymbol{\omega}_2, \boldsymbol{z}_1 \rangle = 0. \tag{7.1.9}$$

From Equations (7.1.7) and (7.1.9) it follows that

$$\boldsymbol{z}_1^{\perp} = K_1 \boldsymbol{\omega}_2,$$

and

$$\boldsymbol{z}_2^{\perp} = K_2 \boldsymbol{\omega}_1,$$

where

$$|K_1| = \frac{||\boldsymbol{z}_1||}{||\boldsymbol{\omega}_2||},$$

and

$$|K_2| = \frac{||\boldsymbol{z}_2||}{||\boldsymbol{\omega}_1||}.$$

Furthermore, using Equations (7.1.6) and (7.1.8), we obtain

$$K_1 = K_1 \cdot 1 = K_1 \langle \boldsymbol{\omega}_2, \boldsymbol{z}_2 \rangle = \langle K_1 \boldsymbol{\omega}_2, \boldsymbol{z}_2 \rangle = \langle \boldsymbol{z}_1^{\perp}, \boldsymbol{z}_2 \rangle,$$

and

$$K_2 = K_2 \cdot 1 = K_2 \langle \boldsymbol{\omega}_1, \boldsymbol{z}_1 \rangle = \langle K_2 \boldsymbol{\omega}_1, \boldsymbol{z}_1 \rangle = \langle \boldsymbol{z}_2^{\perp}, \boldsymbol{z}_1 \rangle = -\langle \boldsymbol{z}_1^{\perp}, \boldsymbol{z}_2 \rangle.$$

This yields

$$K_1 \cdot K_2 = -\langle \boldsymbol{z}_1^{\perp}, \boldsymbol{z}_2 \rangle^2 < 0,$$

from which we can conclude

$$K_1 \cdot K_2 = -|K_1||K_2| = -\frac{||\boldsymbol{z}_1||}{||\boldsymbol{\omega}_2||} \cdot \frac{||\boldsymbol{z}_2||}{||\boldsymbol{\omega}_1||}.$$

Combining this with Equation (7.1.6), it follows

$$\begin{aligned} \cos\theta_3 &= \frac{\langle \boldsymbol{z}_1, \boldsymbol{z}_2 \rangle}{||\boldsymbol{z}_1|| \cdot ||\boldsymbol{z}_2||} \\ &= \frac{\langle \boldsymbol{z}_1^{\perp}, \boldsymbol{z}_2^{\perp} \rangle}{||\boldsymbol{z}_1|| \cdot ||\boldsymbol{z}_2||} \\ &= \frac{\langle K_2 \boldsymbol{\omega}_2, K_1 \boldsymbol{\omega}_1 \rangle}{||\boldsymbol{z}_1|| \cdot ||\boldsymbol{z}_2||} \\ &= -\frac{||\boldsymbol{z}_1||}{||\boldsymbol{\omega}_2||} \cdot \frac{||\boldsymbol{z}_2||}{||\boldsymbol{\omega}_1||} \cdot \frac{\langle \boldsymbol{\omega}_1, \boldsymbol{\omega}_2 \rangle}{||\boldsymbol{z}_1|| \cdot ||\boldsymbol{z}_2||} \\ &= -\frac{\langle \boldsymbol{\omega}_1, \boldsymbol{\omega}_2 \rangle}{||\boldsymbol{\omega}_1|| \cdot ||\boldsymbol{\omega}_2||}. \end{aligned} \tag{7.1.10}$$

This concludes the proof for Equation (7.1.3). The proofs of Equations (7.1.4) and (7.1.5) are similar. □

In the code, Theorem 7.1.2 is used to compute the cosines of the angles of a mesh element. The element satisfies the angle criterion if for all angles θ_i ($i = 1, 2, 3$),

$$\cos(\theta_{max}) \leq \cos(\theta_i) \leq \cos(\theta_{min}),$$

holds true.

7.1.3. Working with two time steps

In [12], a stability criterion was given for displacements of cells per iteration:

$$\max_{c \in \{1,\ldots,N_c(t_k)\}} ||\mathrm{d}\boldsymbol{x}_c(t_k)|| \leq 2R, \tag{7.1.11}$$

where $N_c(t_k)$ is the number of cells at time t_k and $||\mathrm{d}\boldsymbol{x}_c(t)||$ is the norm of the computed displacement at iteration k for cell c. In other words, the maximal distance that is travelled by a cell during one time step is not allowed to be larger then twice the radius of the cells. If the time step is small enough, the mechanical

energy as defined in the model will prevent the cells from moving through each other. On the other hand, if the time step is so large that the norms of the displacement become twice the radius of the cells, the cells can move through each other without noting this. However, it turned out that the stability criterion was already violated for a time step larger than 12 seconds. For a simulated time of, for example 80 days, the computational cost would then rise to approximately half a week, which is not a desirable duration. Although using the GPU would increase the efficiency, a GPU is not always available and hence an algorithm was implemented to avoid this scenario in the CPU-computations. The algorithm splits the model in two parts: for the computation of the cell displacements, a smaller time step Δt_s is used, and for the other components of the model (such as the FEM computations), a regular larger time step Δt is used. In other words, during each time iteration, a number of sub-iterations with time step Δt_s is carried out, in which the cell displacements are computed. Hence, the stability condition is satisfied while the other parts of the model (such as the Finite Element computations) are not carried out during every sub-iteration. Furthermore, the magnitude of Δt_s is estimated before every time iteration, based on the displacements in former iterations, so that Δt_s will not be smaller than strictly necessary.

This procedure is not likely to influence the result to a large extent. The displacements from chemotaxis and random walk are similar as when the global time step Δt would be used for the whole model. They are only corrected by the collision energy to avoid cells moving through each other.

7.1.4. Trianglechecks

For a number of features in the model, it is necessary to know in which triangular element certain coordinates are located. For example, the triangles in which macrophages are contained are needed to solve for the TGF-β concentrations. Furthermore, to compute the cellular forces, the triangles containing (myo)fibroblasts are needed. In the code of [12], a function called 'Trianglecheck' was implemented, which used the barycentric coordinate system to determine if a triangle contains a certain point. This function is also used in the current model, however, it is a modified and extended. We established a list, which stores the indices of the triangular mesh elements in which the cells are located. If it is not yet known in which element a cell is located (for example in the case of new cells), this is indicated by the number -1. Suppose cell i is contained in triangular element $T(i,t_k)$ at time t_k and suppose the maximum of the displacements of cells during iteration $k+1$ is $\max_c ||\mathrm{d}\boldsymbol{x}_i||$. Then at time t_{k+1}, cell c_1 can only be located in triangles that are within a radius of $\max_c ||\mathrm{d}\boldsymbol{x}_i||$ from $T(i,t_k)$. Based on the structured numbering of the mesh, it is easy to determine which triangles have to be detected, saving some computational cost (see Section 7.2).

Suppose the distance in x-direction between two gridnodes in the structured mesh is Δx. Then a $T(i,t_{k+1})$ cannot be more than ceil($\frac{\max_c ||\mathrm{d}\boldsymbol{x}_i||}{\Delta x}$) triangle columns away from the column in which $T(i,t_k)$ is located. Here, ceil denotes the function which rounds the number up to an integer. Analogously, in y-direction, the $T(i,t_{k+1})$ cannot be more than ceil($\frac{\max_c ||\mathrm{d}\boldsymbol{x}_i||}{\Delta y}$) triangle rows away from the row in which $T(i,t_k)$ is located. As the grid being deformed by traction forces, the maximal displacement of gridnodes has to be added to $\max_c ||\mathrm{d}\boldsymbol{x}_i||$, since Δx and Δy can become smaller.

A similar algorithm is used for the calculation of the strain energies. As defined in Equation (6.1.6), the strain energy of cell i is only increased by cell j if cell j is located within the detection range d_i of cell i. If $T(i,t_k)$ is known, then, based on the structured numbering of the mesh, all the cells that are located within a radius of d_i can be found by checking the triangles in that range.

7.1.5. Adapting time step during simulation

During the proliferation phase, the number of fibroblasts and myofibroblasts increases significantly. When carrying out simulations, it turned out that the results of ($IBVP_8$) often became unstable as a result of the larger magnitude of traction forces. A smaller time step is then needed to avoid unstable results. However, the computational cost increase linearly with the decrease of the time step. During the proliferation phase, the velocities in the substrate can be around 100 times larger than usual, which means that making the time step sufficiently small would cause the simulations to last around 100 times longer. An algorithm was implemented to adjust the time step automatically in the course of the simulation.

After each iteration, the maximum of the norms of the displacements during the iteration is calculated:

$$u^k_{max} := \max_{0\leq i\leq N} (||\Delta t^k \boldsymbol{v}^k_i||_2), \tag{7.1.12}$$

where N is the number of grid nodes, Δt^k is the time step at iteration k and $\boldsymbol{v}^k_i$ is the velocity at grid node i during iteration k. Subsequently, u^k_{max} is compared with the average of maximal displacements during the

previous iterations:

$$u_{av}^{k-1} := \sum_{j=0}^{k-1} \left(\frac{u_{max}^{j}}{k-1} \right). \tag{7.1.13}$$

If it turns out that

$$u_{max}^{k} > 2.5 \cdot u_{av}^{k-1}, \tag{7.1.14}$$

then a new time step is defined by

$$\Delta t^{k+1} := \frac{u_{av}^{k}}{u_{max}^{k}} \Delta t^{k}. \tag{7.1.15}$$

To avoid the average maximal displacement to be influenced too much by a sudden increase of the velocity, the new time step is already used to adapt the average of maximal displacements for the next iteration:

$$u_{av}^{k} = \frac{(k+1)\, u_{av}^{k-1} + \max_{i=0}^{N} ||\Delta t^{k+1} \boldsymbol{v}_i^k||_2}{k}. \tag{7.1.16}$$

Furthermore, to avoid an unnecessarily small time step, the time step is increased if the displacements become small again as a results of cellular apoptosis: if

$$u_{max}^{k} < 0.8 \cdot u_{av}^{k-1}, \tag{7.1.17}$$

then

$$\Delta t^{k+1} := f_r \Delta t^{k}, \tag{7.1.18}$$

where

$$f_r := \min \left(\frac{u_{av}^{k}}{u_{max}^{k}}, \frac{\Delta t^{0}}{\Delta t^{k}} \right).$$

7.2. Computational analysis

At first, we state the hardware details for the sake of reproducibility. The computations were carried out with an Intel(R) Core(TM) i7-1065G7 CPU with 8 GB of memory. As compiler, gcc (Ubuntu 9.3.0-17ubuntu1 20.04) 9.3.0 was used.

The models in Chapter 3 and 4 were implemented in Python at first and later on, they were implemented in C++. As expected, the computational cost decreased significantly in C++. In Figure 7.3, the computational cost of the two-dimensional morphoelastic model ($IBVP_6$) from Subsection 4.1.3 are shown respectively in Python and C++. The C++ program turns out to be approximately 30 times faster than the Python program.

Next, we investigate the computational cost of certain components in the model. Figure 7.4 shows the computational cost per iteration of the computation of cell displacements, the Finite Element computations for the elasticity part of the model, and other computations. In the simulation, the same parameter values were used as in Section 6.2 (see Table 6.1). The cell displacements part includes proliferation, apoptosis and differentiation. The graph has the same shape as the graph of the total number of cells in Figure 6.8, which means that there is a more or less linear relationship between the number of cells and the computational work of calculating the cell displacements and states. Hence, for larger numbers of cells, the computational work is much more.

Figure 7.5 presents the Finite Element computations for the chemokine concentration, the trianglechecks (as described in Subsection 7.1.4) and the adaptation of cell location by convective displacement. As described in Subsection 7.1.1, the Finite Element computations for the concentrations are carried out in the class FEM, while for the displacements, they are carried out in FEM-morpho. In Figure 7.5, the category "Adapt mesh" refers to the fact that the mesh in FEM has to be updated once the displacements have been computed in FEM-morpho. This strategy was the easiest way to combine the code for both the agent-based model and the morphoelastic model. However, in the computational perspective, it is not the most efficient way since FEM and FEM-morpho both contain their own mesh and state. Consequently, there have to be many communications between them in order to synchronize with each other. From the results in Figures

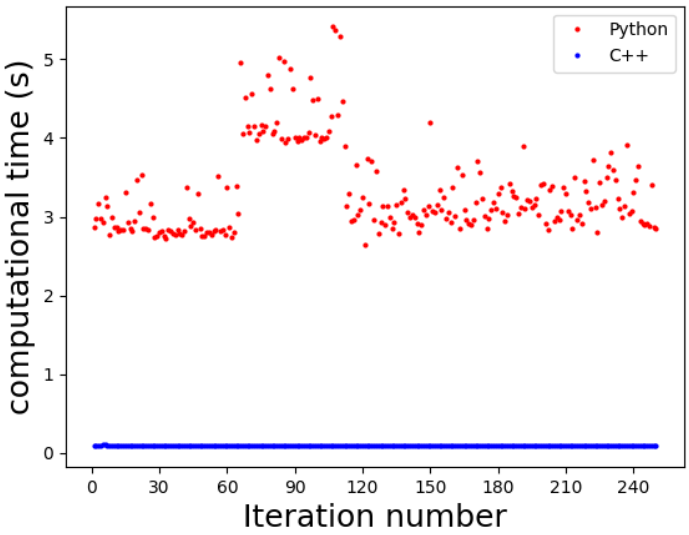

Figure 7.3: Computational cost of simulations of ($IBVP_6$) in Python and C++. The red graph indicates the simulation in Python and the blue graph indicates the simulation in C++

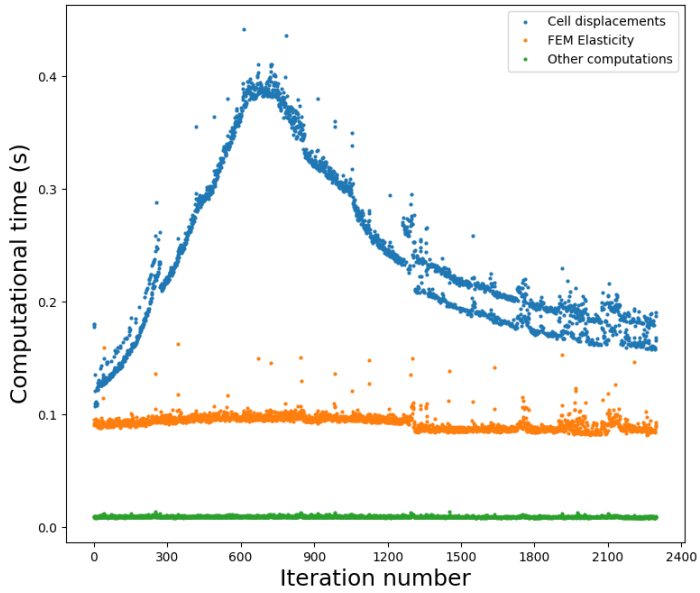

Figure 7.4: Computational cost of several components of the model in Chapter 6. Blue indicates the cell displacement computations, orange indicates the FEM computations for elasticity and green indicates the other computations.

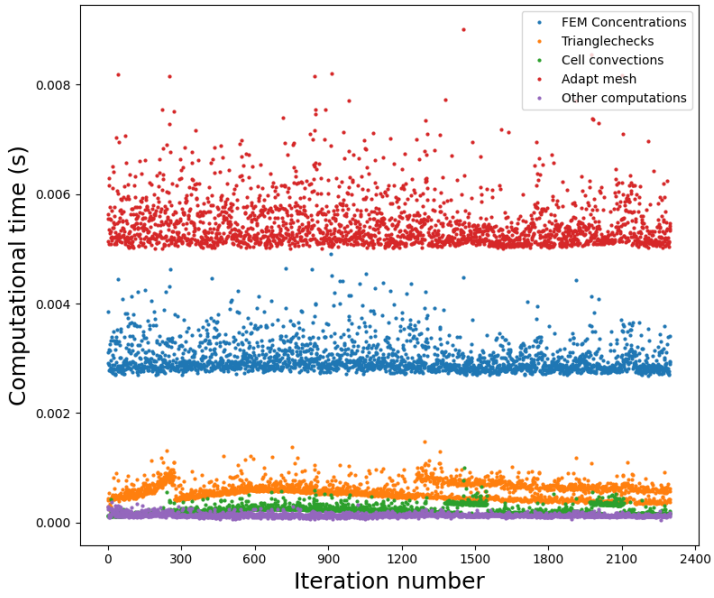

Figure 7.5: Computational cost of other components of the model. Blue indicates the FEM computations for chemokine concentrations, orange indicates the trianglechecks, green indicates computations of convective cell displacements, red indicates the adaptation of the mesh in the FEM class and purple indicates the other computations.

7.4 and 7.5, it appears that the FEM computations for elasticity need much more time than for the concentrations of chemokines. The reason is that for $(IBVP_8)$, the numerical system is five times as large as the numerical systems for $(IBVP_P)$ and $(IBVP_\beta)$.

From the figures, it is clear that the computational cost per iteration mainly consist of the computation of the cell displacements and the FEM computations for elasticity. In [12], for the CPU computations, the computational cost per iteration for computing the strain energy densities with 1800 cells in the domain was around 0.06 seconds. Currently, by using the improved trianglecheck functions, it is around 0.01 seconds, which is six times faster. Although this improvement has not yet been implemented on the GPU, it is promising to improve the computational efficiency further. However, in Figure 7.4, the computational work for cell displacements is around 0.12 seconds per iteration (at $t = 0$, when there are 1800 cells in the domain). This is much larger than the aforementioned 0.01 seconds. However, this is caused by the fact that the strain energies are computed multiple times during one iteration, by the algorithm of 'subiterations' described in Subsection 7.1.3. Although this causes the workload per iteration to increase, the global time step is approximately 200 times larger than when the stability condition in Equation (7.1.11) has to be satisfied. Hence, effectively, the computational cost has decreased.

The computational cost for remeshing is not displayed in the figures, since remeshing only happens a few times during the simulation. However, from measurements, it turn out that the computational cost for remeshing varied from 0.02 to 0.06 seconds.

As for the Monte Carlo simulations in Section 6.3, the module Multiprocessing in Python, which makes it possible to run four simulations at the same time without increasing the computational cost per simulation. Averagely, a single simulations needed approximately eight minutes to run. Consequently, when running multiple simulations with multiprocessing, the average computation time per simulations is approximately two minutes.

8

Conclusion and discussion

8.1. Conclusion

In this project, at first we developed several elastic models to describe the deformation of an elastic material, so that later they could be used to model the deformation of the ECM. Further, they were developed in both one and two dimensions and with gradually increasing complexity. The models were compared in various aspects and in particular analyzed from numerical perspective. The two-dimensional morphoelastic model was extended with the addition of point forces. Several parameter sensitivity tests were carried out with the morphoelastic model with point forces, some of which confirmed biological observations.

We extended the agent-based model for wound healing developed in [12] by incorporating the morphoelastic model with point forces and by making a separation between regular fibroblasts and myofibroblasts. To avoid the numerical results becoming unstable for certain parameter values, an algorithm was implemented to adapt the time step automatically if the velocities are too large. Monte Carlo simulations were carried out with the model to investigate relations between several input and output parameters. From the results, it could be concluded that there is a strong relationship between the state of the wound in early phases and later phases of the healing. In other words, it would be helpful for the physicians and surgeons to foresee the healing process if they know certain data in the early stage of the healing.

One of the long-term objectives of the model is to provide a simulation tool, so that the model can compute the probability and the degree of the contraction of the wound by inputting patient-characteristic data, such as age, gender and race. Therefore, it is important to decrease the computational cost of the simulations, to which end the model was implemented in C++. Currently, Monte Carlo simulations for a domain with approximately 2000 cells on average can be carried out with a computational cost of approximately two minutes per simulation averagely.

8.2. Discussion and future work

In this section, we suggest a few research directions and display some remarks of the current agent-based model for wound healing.

The agent-based model was expanded with morphoelasticity and differentiation to myofibroblasts. Hence, the model is more complete and suitable to obtain more insights into the interaction between cellular behaviour and the deformation of the ECM.

The agent-based model has the advantage that some parameters are measurable and can be used directly. However, currently the correct value of some parameters is unknown, and the values also differ from the location of the wound in the body. In the literature, one can find several different values for the same parameter used in various models or measured with different techniques in the laboratories [3]. Furthermore, when the numerical settings of the model are modified, (for example if the scale of the computational domain is changed), several parameters have to be adjusted. The possibility of Monte Carlo simulations now makes it easier to investigate the effect of the parameter values on the results of the model, which is promising to fine-tune the parameter values further.

By implementing the model in C++ and improving the computational efficiency of several components of the model, it is now possible to carry out Monte Carlo simulations. This makes the model more valuable and potential for practical use. There are many possibilities to increase the computational efficiency further.

Parts of the model are already implemented on the GPU with CUDA [12]. If this code is updated for the new model, the computational efficiency can become even higher. Furthermore, the code can still be optimized further, for example by combining the classes FEM and FEM-morpho (see Chapter 7).

The angles of the triangles in the used mesh at $t = 0$ were equal to $\frac{1}{2}\pi$, $\frac{1}{4}\pi$ and $\frac{1}{4}\pi$. This mesh was not generated automatically with the help of a software module, but it was manually constructed in the code. The structured mesh has the advantage that the knowledge an logic in the ordering and numbering, helps to make computations more efficient. On the other side, the angles of the mesh are not optimal, in particular because in the moving mesh, triangles are easy to become ill-shaped, which indicates that some angles are so small, that the triangle is nearly degenerate. This problem was solved by remeshing, which works fine if the domain boundary is more or less fixed (that is, if the spring constant a in the Robin boundary condition is large enough). As the displacements near the domain boundary become larger, it is difficult to maintain a structured mesh without angles becoming too small or too large, even if remeshing is carried out. Hence, further options for triangulation to improve this, could be investigated: for example, in [12], the Triangle software was used to generate an unstructured mesh with angles that are close to $\frac{1}{3}\pi$, which is the ideal angle magnitude. Furthermore, at the end of this thesis, a structured mesh was written with most of the angles close to $\frac{1}{3}\pi$. Although this mesh was not tested extensively, it is promising for later use.

In future work, more aspects could be incorporated in the model, such as the presence of fibrin bundles and the orientation of collagen [16]. Furthermore, the model could be extended to three dimension. As the computational efficiency is more and more improving, the model becomes more suitable for further extension.

A

Derivations of Weak Forms and Galerkin Equations

A.1. One-dimensional purely elastic model

In order to derive the weak form, we multiply the differential equation with the test function ϕ and integrate over the domain:

$$\begin{aligned}
\int_0^L -E_s u''(x)\phi(x)\,\mathrm{d}x &= \int_0^L f(x)\phi(x)\,\mathrm{d}x,\\
-E_s\int_0^L \left[u'(x)\phi(x)\right]' - u'(x)\phi'(x)\,\mathrm{d}x &= \int_0^L f(x)\phi(x)\,\mathrm{d}x,\\
-E_s\left(u'(L)\phi(L) - u'(0)\phi(0)\right) + E_s\int_0^L u'(x)\phi(x)\,\mathrm{d}x &= \int_0^L f(x)\phi(x)\,\mathrm{d}x,\\
E_s\int_0^L u'(x)\phi(x)\,\mathrm{d}x &= \int_0^L f(x)\phi(x)\,\mathrm{d}x.
\end{aligned}$$

This yields the following weak form:

$$(W): \begin{cases} \text{Find } u \in H^1(\Omega) \text{ such that} \\ E_s\int_0^L u'(x)\phi(x)\,\mathrm{d}x = \int_0^L f(x)\phi(x)\,\mathrm{d}x, \\ \text{for all } \phi(x) \in H^1(\Omega). \end{cases}$$

A.2. One-dimensional viscoelastic model

We now proceed to derive the weak form of the Cauchy Momentum Equation:

$$\frac{\mathrm{D}(\rho v)}{\mathrm{D}t} + \rho v\frac{\partial v}{\partial x} = \frac{\partial \sigma}{\partial x} + f. \tag{A.2.1}$$

In order to derive the weak forms of the equations, we multiply by a test function ϕ, and integrate over the domain $\Omega(t) = [0, l(t)]$:

$$\int_0^{l(t)} \left(\frac{\mathrm{D}\left(\rho v\right)}{\mathrm{D}t} + \rho v\frac{\partial v}{\partial x}\right)\phi\,\mathrm{d}x = \int_0^{l(t)} \left(\frac{\partial \sigma}{\partial x} + f\right)\phi\,\mathrm{d}x \tag{A.2.2}$$

For the test function ϕ we will use piecewise linear basis functions. According to **Theorem 3.3.2**, it can be derived that

$$\frac{\mathrm{D}(\rho v)}{\mathrm{D}t}\phi = \frac{\mathrm{D}(\rho v\phi)}{\mathrm{D}t} - \rho v\frac{\mathrm{D}\phi}{\mathrm{D}t} = \frac{\mathrm{D}(\rho v\phi)}{\mathrm{D}t}. \tag{A.2.3}$$

Using the former result and the Product Rule twice, we obtain that

$$\int_0^{l(t)} \frac{\mathrm{D}(\rho v\phi)}{\mathrm{D}t} + \rho\frac{\partial(v^2\phi)}{\partial x} - \rho v\frac{\partial(v\phi)}{\partial x}\,\mathrm{d}x = \int_0^{l(t)} \frac{\partial(\sigma\phi)}{\partial x} - \sigma\frac{\partial\phi}{\partial x} + f\phi\,\mathrm{d}x. \tag{A.2.4}$$

Now using the fact that

$$\frac{\mathrm{D}(\rho v\phi)}{\mathrm{D}t} = \rho\frac{\partial(v\phi)}{\partial t} + \rho v\frac{\partial(v\phi)}{\partial x}, \tag{A.2.5}$$

we obtain

$$\int_0^{l(t)} \rho\frac{\partial(v\phi)}{\partial t} + \rho\frac{\partial(v^2\phi)}{\partial x}\,\mathrm{d}x = \int_0^{l(t)} \frac{\partial(\sigma\phi)}{\partial x} - \sigma\frac{\partial\phi}{\partial x} + f\phi\,\mathrm{d}x. \tag{A.2.6}$$

Applying Leibniz' Rule and Gauß's Theorem twice, respectively, yields

$$\frac{\mathrm{d}}{\mathrm{d}t}\left(\int_0^{l(t)} \rho v\phi\,\mathrm{d}x\right) - [\rho v\phi]^{x=l(t)} l'(t) + \int_0^{l(t)} \rho\frac{\partial(v^2\phi)}{\partial x}\,\mathrm{d}x = \int_0^{l(t)} \frac{\partial(\sigma\phi)}{\partial x} - \sigma\frac{\partial\phi}{\partial x} + f\phi\,\mathrm{d}x, \tag{A.2.7}$$

$$\frac{\mathrm{d}}{\mathrm{d}t}\left(\int_0^{l(t)} \rho v\phi\,\mathrm{d}x\right) - [\rho v\phi]^{x=l(t)} l'(t) + [\rho v^2\phi]_{x=0}^{x=l(t)} = \int_0^{l(t)} \frac{\partial(\sigma\phi)}{\partial x} - \sigma\frac{\partial\phi}{\partial x} + f\phi\,\mathrm{d}x. \tag{A.2.8}$$

Noting that $l'(t) = v(l(t), t)$ and applying the boundary condition $v(0, t) = 0$, we obtain

$$\frac{\mathrm{d}}{\mathrm{d}t}\left(\int_0^{l(t)} \rho v\phi\,\mathrm{d}x\right) = \int_0^{l(t)} \frac{\partial(\sigma\phi)}{\partial x} - \sigma\frac{\partial\phi}{\partial x} + f\phi\,\mathrm{d}x. \tag{A.2.9}$$

We apply Gauß's Theorem to the right-hand side and apply the boundary condition $\sigma(l(t), t) = 0$ and $\phi(0, t) = 0$, which yields

$$\frac{\mathrm{d}}{\mathrm{d}t}\left(\int_0^{l(t)} \rho v\phi\,\mathrm{d}x\right) = [\sigma\phi]_{x=0}^{x=l(t)} + \int_0^{l(t)} -\sigma\frac{\partial\phi}{\partial x} + f\phi\,\mathrm{d}x, \tag{A.2.10}$$

$$\frac{\mathrm{d}}{\mathrm{d}t}\left(\int_0^{l(t)} \rho v\phi\,\mathrm{d}x\right) = -\int_0^{l(t)} \sigma\frac{\partial\phi}{\partial x} - f\phi\,\mathrm{d}x. \tag{A.2.11}$$

Substituting $\sigma = \mu\frac{\partial v}{\partial x} + E_s\varepsilon = \mu\frac{\partial v}{\partial x} + E_s\frac{\partial u}{\partial x}$, this yields the weak form:

$$\frac{\mathrm{d}}{\mathrm{d}t}\left(\int_0^{l(t)} \rho v\phi\,\mathrm{d}x\right) + \int_0^{l(t)} \mu\frac{\partial v}{\partial x}\frac{\partial\phi}{\partial x} + E_s\frac{\partial u}{\partial x}\frac{\partial\phi}{\partial x}\,\mathrm{d}x = \int_0^{l(t)} f\phi\,\mathrm{d}x. \tag{A.2.12}$$

A.3. One-dimensional morphoelastic model

Now we will derive the weak form of the strain evoluation equation

$$\frac{\mathrm{D}\varepsilon}{\mathrm{D}t} + (\varepsilon - 1)\frac{\partial v}{\partial x} = -g. \tag{A.3.1}$$

We multiply by the test function $\psi \in L^2(H^1(\Omega(t)), (0, T))$ and integrate over $(0, l(t))$:

$$\int_0^{l(t)} \left(\frac{\mathrm{D}\varepsilon}{\mathrm{D}t} + (\varepsilon - 1)\frac{\partial v}{\partial x}\right)\psi\,\mathrm{d}x = -\int_0^{l(t)} g\psi\,\mathrm{d}x \tag{A.3.2}$$

By **Theorem 3.3.2**, we obtain

$$\int_0^{l(t)} \frac{\mathrm{D}(\varepsilon\psi)}{\mathrm{D}t} + (\varepsilon - 1)\frac{\partial v}{\partial x}\psi\,\mathrm{d}x = -\int_0^{l(t)} g\psi\,\mathrm{d}x, \tag{A.3.3}$$

$$\int_0^{l(t)} \frac{\partial(\varepsilon\psi)}{\partial t} + v\frac{\partial(\varepsilon\psi)}{\partial x} + \varepsilon\psi\frac{\partial v}{\partial x} - \frac{\partial v}{\partial x}\psi\,\mathrm{d}x = -\int_0^{l(t)} g\psi\,\mathrm{d}x. \tag{A.3.4}$$

Applying the Product Rule yields

$$\int_0^{l(t)} \frac{\partial(\varepsilon\psi)}{\partial t} + \frac{\partial(v\varepsilon\psi)}{\partial x} - \frac{\partial v}{\partial x}\psi\,\mathrm{d}x = -\int_0^{l(t)} g\psi\,\mathrm{d}x. \tag{A.3.5}$$

Now we apply Leibniz' Rule and Gauß's Theorem, obtaining

$$\frac{\mathrm{d}}{\mathrm{d}t}\left(\int_0^{l(t)} \varepsilon\psi \,\mathrm{d}x\right) + \left[\varepsilon\psi\right]^{x=l(t)} l'(t) + \left[v\varepsilon\psi\right]_{x=0}^{x=l(t)} - \int_0^{l(t)} \frac{\partial v}{\partial x}\psi \,\mathrm{d}x \quad = \quad -\int_0^{l(t)} g\psi \,\mathrm{d}x. \tag{A.3.6}$$

Now using that $l'(t) = v(l(t))$ and the boundary condition $v(0) = 0$, we obtain as a weak form

$$\frac{\mathrm{d}}{\mathrm{d}t}\left(\int_0^{l(t)} \varepsilon\psi \,\mathrm{d}x\right) - \int_0^{l(t)} \frac{\partial v}{\partial x}\psi \,\mathrm{d}x \quad = \quad -\int_0^{l(t)} g\psi \,\mathrm{d}x. \tag{A.3.7}$$

Substituting $g = \xi\varepsilon$, as it was discussed in Subsection 3.4.1, we obtain

$$\frac{\mathrm{d}}{\mathrm{d}t}\left(\int_0^{l(t)} \varepsilon\psi \,\mathrm{d}x\right) + \int_0^{l(t)} \xi\varepsilon\psi - \frac{\partial v}{\partial x}\psi \,\mathrm{d}x \quad = \quad 0. \tag{A.3.8}$$

A.4. Two-dimensional Purely elastic model

In order to obtain the weak form of the Cauchy Momentum Equation, we multiply by the test function and integrate over Ω. We have for $d = 1,2$:

$$\int_{\Omega(t)} \left(\frac{\mathrm{D}(\rho v_d)}{\mathrm{D}t} + \rho v_d \nabla\cdot\boldsymbol{v}\right)\phi \,\mathrm{d}\Omega = \int_{\Omega(t)} \left(\nabla\cdot\boldsymbol{\sigma}_{\cdot d} + f_d\right)\phi \,\mathrm{d}\Omega. \tag{A.4.1}$$

According to Theorem 4.2, this yields

$$\int_{\Omega(t)} \frac{\mathrm{D}(\rho v_d\phi)}{\mathrm{D}t} + \rho v_d\phi\nabla\cdot\boldsymbol{v} \,\mathrm{d}\Omega \quad = \quad \int_{\Omega(t)} (\nabla\cdot\boldsymbol{\sigma}_{\cdot d})\phi + f_d\phi \,\mathrm{d}\Omega. \tag{A.4.2}$$

Now note that

$$\begin{aligned}
&\int_{\Omega(t)} \frac{\mathrm{D}(\rho v_d\phi)}{\mathrm{D}t} + \rho v_d\phi\nabla\cdot\boldsymbol{v} \,\mathrm{d}\Omega && (A.4.3)\\
= \quad &\rho\int_{\Omega(t)} \frac{\partial(v_d\phi)}{\partial t} + \boldsymbol{v}\cdot\nabla(v_d\phi) + v_d\phi\nabla\cdot\boldsymbol{v} \,\mathrm{d}\Omega && (A.4.4)\\
= \quad &\rho\frac{\mathrm{d}}{\mathrm{d}t}\left(\int_{\Omega(t)} v_d\phi \,\mathrm{d}\Omega\right) - \oint_{\partial\Omega(t)} v_d\phi\boldsymbol{v}\cdot\boldsymbol{n} \,\mathrm{d}\Gamma + \int_{\Omega(t)} \boldsymbol{v}\cdot\nabla(v_d\phi) + v_d\phi\nabla\cdot\boldsymbol{v} \,\mathrm{d}\Omega && (A.4.5)\\
= \quad &\rho\frac{\mathrm{d}}{\mathrm{d}t}\left(\int_{\Omega(t)} v_d\phi \,\mathrm{d}\Omega\right) + \int_{\Omega(t)} -\nabla\cdot(v_d\phi\boldsymbol{v}) + \boldsymbol{v}\cdot\nabla(v_d\phi) + v_d\phi\nabla\cdot\boldsymbol{v} \,\mathrm{d}\Omega && (A.4.6)\\
= \quad &\rho\frac{\mathrm{d}}{\mathrm{d}t}\left(\int_{\Omega(t)} v_d\phi \,\mathrm{d}\Omega\right) + \int_{\Omega(t)} -v_d\phi\nabla\cdot\boldsymbol{v} - \boldsymbol{v}\cdot\nabla(v_d\phi) + \boldsymbol{v}\cdot\nabla(v_d\phi) + v_d\phi\nabla\cdot\boldsymbol{v} \,\mathrm{d}\Omega && (A.4.7)\\
= \quad &\rho\frac{\mathrm{d}}{\mathrm{d}t}\left(\int_{\Omega(t)} v_d\phi \,\mathrm{d}\Omega\right). && (A.4.8)
\end{aligned}$$

Hence, we have

$$\rho\frac{\mathrm{d}}{\mathrm{d}t}\left(\int_{\Omega(t)} v_d\phi \,\mathrm{d}\Omega\right) \quad = \quad \int_{\Omega(t)} (\nabla\cdot\boldsymbol{\sigma}_{\cdot d})\phi + f_d\phi \,\mathrm{d}\Omega. \tag{A.4.9}$$

Furthermore, using Leibniz' Rule and the Product Rule,

$$\begin{aligned}
\rho\frac{\mathrm{d}}{\mathrm{d}t}\left(\int_{\Omega(t)} v_d\phi \,\mathrm{d}\Omega\right) \quad &= \quad \int_{\Omega(t)} \nabla\cdot(\boldsymbol{\sigma}_{\cdot d}\phi) - \boldsymbol{\sigma}_{\cdot d}\cdot\nabla\phi + f_d\phi \,\mathrm{d}\Omega, && (A.4.10)\\
\rho\frac{\mathrm{d}}{\mathrm{d}t}\left(\int_{\Omega(t)} v_d\phi \,\mathrm{d}\Omega\right) \quad &= \quad \oint_{\partial\Omega(t)} \boldsymbol{\sigma}_{\cdot d}\cdot\boldsymbol{n}\phi \,\mathrm{d}\Gamma + \int_{\Omega(t)} -\boldsymbol{\sigma}_{\cdot d}\cdot\nabla\phi + f_d\phi \,\mathrm{d}\Omega. && (A.4.11)
\end{aligned}$$

For now, we will omit the part

$$\oint_{\partial\Omega(t)} \boldsymbol{\sigma}_{\cdot d}\cdot\boldsymbol{n}\phi \,\mathrm{d}\Gamma, \tag{A.4.12}$$

since we will handle the boundary conditions separately, namely in Subsection A.7 In the purely elastic model, we substitute

$$\sigma_{11} = \frac{E_s\sqrt{\rho}}{1+\eta}\left(\varepsilon_{11} + \frac{\eta}{1-2\eta}(\varepsilon_{11}+\varepsilon_{22})\right), \tag{A.4.13}$$

$$\sigma_{12} = \sigma_{21} = \frac{E_s\sqrt{\rho}}{1+\eta}\varepsilon_{12}, \tag{A.4.14}$$

$$\sigma_{22} = \frac{E_s\sqrt{\rho}}{1+\eta}\left(\varepsilon_{22} + \frac{\eta}{1-2\eta}(\varepsilon_{11}+\varepsilon_{22})\right). \tag{A.4.15}$$

This yields

$$\begin{aligned}\rho\frac{\mathrm{d}}{\mathrm{d}t}\left(\int_{\Omega(t)} v_1\phi \,\mathrm{d}\Omega\right) &= -\frac{E_s\sqrt{\rho}}{1+\eta}\int_{\Omega(t)}\left(\varepsilon_{11} + \frac{\eta}{1-2\eta}(\varepsilon_{11}+\varepsilon_{22})\right)\frac{\partial\phi}{\partial x} + \varepsilon_{12}\frac{\partial\phi}{\partial y}\mathrm{d}\Omega \\ &+ \int_{\Omega(t)} f_1\phi \,\mathrm{d}\Omega\end{aligned} \tag{A.4.16}$$

and

$$\begin{aligned}\rho\frac{\mathrm{d}}{\mathrm{d}t}\left(\int_{\Omega(t)} v_2\phi \,\mathrm{d}\Omega\right) &= -\frac{E_s\sqrt{\rho}}{1+\eta}\int_{\Omega(t)}\varepsilon_{12}\frac{\partial\phi}{\partial x} + \left(\varepsilon_{22} + \frac{\eta}{1-2\eta}(\varepsilon_{11}+\varepsilon_{22})\right)\frac{\partial\phi}{\partial y}\mathrm{d}\Omega \\ &+ \int_{\Omega(t)} f_2\phi \,\mathrm{d}\Omega.\end{aligned} \tag{A.4.17}$$

For the elastic and viscoelastic model, we will express the weak forms in terms of the displacement $\boldsymbol{u}$. Using the definitions of strain from the elastic model, we have:

$$\varepsilon_{11} = \frac{\partial u_1}{\partial x}, \tag{A.4.18}$$

$$\varepsilon_{12} = \varepsilon_{21} = \frac{1}{2}\left(\frac{\partial u_1}{\partial y} + \frac{\partial u_2}{\partial x}\right), \tag{A.4.19}$$

$$\varepsilon_{22} = \frac{\partial u_2}{\partial y}. \tag{A.4.20}$$

This yields weak forms

$$\begin{aligned}\rho\frac{\mathrm{d}}{\mathrm{d}t}\left(\int_{\Omega(t)} v_1\phi \,\mathrm{d}\Omega\right) &= -\frac{E_s\sqrt{\rho}}{1+\eta}\int_{\Omega(t)}\left(\frac{1-\eta}{1-2\eta}\frac{\partial u_1}{\partial x} + \frac{\eta}{1-2\eta}\frac{\partial u_2}{\partial y}\right)\frac{\partial\phi}{\partial x} + \frac{1}{2}\left(\frac{\partial u_1}{\partial y} + \frac{\partial u_2}{\partial x}\right)\frac{\partial\phi}{\partial y}\mathrm{d}\Omega \\ &+ \int_{\Omega(t)} f_1\phi \,\mathrm{d}\Omega\end{aligned} \tag{A.4.21}$$

and

$$\begin{aligned}\rho\frac{\mathrm{d}}{\mathrm{d}t}\left(\int_{\Omega(t)} v_2\phi \,\mathrm{d}\Omega\right) &= -\frac{E_s\sqrt{\rho}}{1+\eta}\int_{\Omega(t)}\frac{1}{2}\left(\frac{\partial u_1}{\partial y} + \frac{\partial u_2}{\partial x}\right)\frac{\partial\phi}{\partial x} + \left(\frac{\eta}{1-2\eta}\frac{\partial u_1}{\partial x} + \frac{1-\eta}{1-2\eta}\frac{\partial u_2}{\partial y}\right)\frac{\partial\phi}{\partial y}\mathrm{d}\Omega \\ &+ \int_{\Omega(t)} f_2\phi \,\mathrm{d}\Omega.\end{aligned} \tag{A.4.22}$$

Defining $N := (n_x+1)\cdot(n_y+1)-1$ (which is the number of nodes in Ω minus one), this yields the following Galerkin equations:

$$\begin{aligned}\rho\sum_{j=0}^{N}(v_1)_j^+\int_{\Omega^+}\phi_i^+\phi_j^+ \,\mathrm{d}\Omega &= \rho\sum_{j=0}^{N}(v_1)_j\int_{\Omega(t)}\phi_i\phi_j \,\mathrm{d}\Omega \\ &+ \Delta t\frac{E_s\sqrt{\rho}}{1+\eta}\sum_{j=0}^{N}(u_1)_j^+\left(-\int_{\Omega^+}\frac{1-\eta}{1-2\eta}\frac{\partial\phi_i^+}{\partial x}\frac{\partial\phi_j^+}{\partial x} + \frac{1}{2}\frac{\partial\phi_i^+}{\partial y}\frac{\partial\phi_j^+}{\partial y}\mathrm{d}\Omega\right) \\ &+ \Delta t\frac{E_s\sqrt{\rho}}{1+\eta}\sum_{j=0}^{N}(u_2)_j^+\left(-\int_{\Omega^+}\frac{\eta}{1-2\eta}\frac{\partial\phi_i^+}{\partial x}\frac{\partial\phi_j^+}{\partial y} + \frac{1}{2}\frac{\partial\phi_i^+}{\partial y}\frac{\partial\phi_j^+}{\partial x}\mathrm{d}\Omega\right) \\ &+ \Delta t\int_{\Omega^+} f_1^+\phi_i^+ \,\mathrm{d}\Omega\end{aligned} \tag{A.4.23}$$

and

$$\begin{aligned}\rho\sum_{j=0}^{N}(v_2)_j^+\int_{\Omega^+}\phi_i^+\phi_j^+\,\mathrm{d}\Omega &= \rho\sum_{j=0}^{N}(v_2)_j\int_{\Omega(t)}\phi_i\phi_j\,\mathrm{d}\Omega\\ &+ \Delta t\frac{E_s\sqrt{\rho}}{1+\eta}\sum_{j=0}^{N}(u_1)_j^+\left(-\int_{\Omega^+}\frac{1}{2}\frac{\partial\phi_i^+}{\partial x}\frac{\partial\phi_j^+}{\partial y}+\frac{\eta}{1-2\eta}\frac{\partial\phi_i^+}{\partial y}\frac{\partial\phi_j^+}{\partial x}\mathrm{d}\Omega\right)\\ &+ \Delta t\frac{E_s\sqrt{\rho}}{1+\eta}\sum_{j=0}^{N}(u_2)_j^+\left(-\int_{\Omega^+}\frac{1}{2}\frac{\partial\phi_i^+}{\partial x}\frac{\partial\phi_j^+}{\partial x}+\frac{1-\eta}{1-2\eta}\frac{\partial\phi_i^+}{\partial y}\frac{\partial\phi_j^+}{\partial y}\mathrm{d}\Omega\right)\\ &+ \Delta t\int_{\Omega^+}f_2^+\phi_i^+\,\mathrm{d}\Omega. \end{aligned}\tag{A.4.24}$$

Here, $\Omega^+ := \Omega(t+\Delta t)$. Furthermore, all variables with a superscript + should be evaluated at $t = t+\Delta t$. We can write these two equations as systems

$$\begin{aligned}\rho M_1^{k+1}\boldsymbol{v}_1^{k+1} &= \rho M_1^k\boldsymbol{v}_1^k\\ &+ \Delta t\frac{E_s\sqrt{\rho}}{1+\eta}\left(\left(\frac{1-\eta}{1-2\eta}S_1^{k+1}+\frac{1}{2}S_2^{k+1}\right)\boldsymbol{u}_1^{k+1}+\left(\frac{\eta}{1-2\eta}S_3^{k+1}+\frac{1}{2}S_4^{k+1}\right)\boldsymbol{u}_2^{k+1}\right)\\ &+ \Delta t\boldsymbol{f}_1^{k+1}\end{aligned}\tag{A.4.25}$$

and

$$\begin{aligned}\rho M_1^{k+1}\boldsymbol{v}_2^{k+1} &= \rho M_1^k\boldsymbol{v}_2^k\\ &+ \Delta t\frac{E_s\sqrt{\rho}}{1+\eta}\left(\left(\frac{\eta}{1-2\eta}S_4^{k+1}+\frac{1}{2}S_3^{k+1}\right)\boldsymbol{u}_1^{k+1}+\left(\frac{1-\eta}{1-2\eta}S_2^{k+1}+\frac{1}{2}S_1^{k+1}\right)\boldsymbol{u}_2^{k+1}\right)\\ &+ \Delta t\boldsymbol{f}_2^{k+1}.\end{aligned}\tag{A.4.26}$$

The matrices M_1^k and S_l^k ($l = 1,\ldots 4$), are $(N+1)\times(N+1)$-matrices and $\boldsymbol{f}_1^k$, $\boldsymbol{f}_2^k$ vectors of length $N+1$ with the following element matrices and element vector:

$$(M_1^k)_e = \frac{|\Delta|_e^k}{24}\begin{pmatrix}2&1&1\\1&2&1\\1&1&2\end{pmatrix},\tag{A.4.27}$$

$$(S_1^k)_e = -\frac{|\Delta|_e^k}{2}\begin{pmatrix}\beta_1\beta_1&\beta_1\beta_2&\beta_1\beta_3\\\beta_2\beta_1&\beta_2\beta_2&\beta_2\beta_3\\\beta_3\beta_1&\beta_3\beta_2&\beta_3\beta_3\end{pmatrix},\tag{A.4.28}$$

$$(S_2^k)_e = -\frac{|\Delta|_e^k}{2}\begin{pmatrix}\gamma_1\gamma_1&\gamma_1\gamma_2&\gamma_1\gamma_3\\\gamma_2\gamma_1&\gamma_2\gamma_2&\gamma_2\gamma_3\\\gamma_3\gamma_1&\gamma_3\gamma_2&\gamma_3\gamma_3\end{pmatrix},\tag{A.4.29}$$

$$(S_3^k)_e = -\frac{|\Delta|_e^k}{2}\begin{pmatrix}\beta_1\gamma_1&\beta_1\gamma_2&\beta_1\gamma_3\\\beta_2\gamma_1&\beta_2\gamma_2&\beta_2\gamma_3\\\beta_3\gamma_1&\beta_3\gamma_2&\beta_3\gamma_3\end{pmatrix},\tag{A.4.30}$$

$$(S_4^k)_e = -\frac{|\Delta|_e^k}{2}\begin{pmatrix}\gamma_1\beta_1&\gamma_1\beta_2&\gamma_1\beta_3\\\gamma_2\beta_1&\gamma_2\beta_2&\gamma_2\beta_3\\\gamma_3\beta_1&\gamma_3\beta_2&\gamma_3\beta_3\end{pmatrix},\tag{A.4.31}$$

$$(\boldsymbol{f}_d^k)_e = \frac{|\Delta|_e^k}{6}\begin{pmatrix}f_d(p_1^k,k\Delta t)\\f_d(p_2^k,k\Delta t)\\f_d(p_3^k,k\Delta t)\end{pmatrix},\tag{A.4.32}$$

where $|\Delta|_e^k$ denotes twice the area of the element $e = (p_1^k, p_2^k, p_3^k)$ at time step k. Furthermore,

$$\beta_i := \beta_{p_i},\qquad \gamma_i := \gamma_{p_i},\qquad (i = 1,2,3)$$

and

$$\boldsymbol{v}_d^k := \left((v_d)_0^k,\ldots,(v_d)_N^k\right)^T,\ \boldsymbol{u}_d^k := \left((u_d)_0^k,\ldots,(u_d)_N^k\right)^T \text{ and } \boldsymbol{f}_d^k := \left((f_d)_0^k,\ldots,(f_d)_N^k\right)^T,\ (d = 1,2).$$

Same as in the one-dimensional case, $\boldsymbol{u}_d^{k+1}$ is approximated by:

$$\boldsymbol{u}_d^{k+1} \approx \boldsymbol{u}_d^k + \Delta t \boldsymbol{v}_d^k, \qquad (d = 1,2). \tag{A.4.33}$$

The above element matrices only hold for internal elements. However, we will deal with the boundary elements separately in Subsection A.7.

A.5. Two-dimensional viscoelastic model

In the viscoelastic model, all the equations are the same as in the elastic model, except for the definitions of stress:

$$\begin{cases} \sigma_{11} = \mu_1 \frac{\partial v_1}{\partial x} + \mu_2 \nabla \cdot \boldsymbol{v} + \frac{E_s\sqrt{\rho}}{1+\eta}\left(\varepsilon_{11} + \frac{\eta}{1-2\eta}(\varepsilon_{11}+\varepsilon_{22})\right), & (\boldsymbol{x} \in \Omega, t > 0) \\ \sigma_{12} = \frac{1}{2}\mu_1\left(\frac{\partial v_1}{\partial y} + \frac{\partial v_2}{\partial x}\right) + \frac{E_s\sqrt{\rho}}{1+\eta}\varepsilon_{12}, & (\boldsymbol{x} \in \Omega, t > 0) \\ \sigma_{22} = \mu_1 \frac{\partial v_2}{\partial y} + \mu_2 \nabla \cdot \boldsymbol{v} + \frac{E_s\sqrt{\rho}}{1+\eta}\left(\varepsilon_{22} + \frac{\eta}{1-2\eta}(\varepsilon_{11}+\varepsilon_{22})\right), & (\boldsymbol{x} \in \Omega, t > 0), \end{cases} \tag{A.5.1}$$

We see that the expressions

$$\overline{\sigma}_{11} = \mu_1 \frac{\partial v_1}{\partial x} + \mu_2 \nabla \cdot \boldsymbol{v}, \tag{A.5.2}$$

$$\overline{\sigma}_{12} = \frac{1}{2}\mu_1\left(\frac{\partial v_1}{\partial y} + \frac{\partial v_2}{\partial x}\right), \tag{A.5.3}$$

$$\overline{\sigma}_{22} = \mu_1 \frac{\partial v_2}{\partial y} + \mu_2 \nabla \cdot \boldsymbol{v} \tag{A.5.4}$$

are added to σ_{11}, σ_{12} and σ_{22} respectively. This means that, according to Equation (A.4.11), we should add the following to the right-hand side of Equation (A.4.21):

$$\begin{aligned} & \oint_{\partial\Omega(t)} \overline{\boldsymbol{\sigma}}_{\cdot 1} \cdot \boldsymbol{n}\phi \, \mathrm{d}\Gamma + \int_{\Omega(t)} -\overline{\boldsymbol{\sigma}}_{\cdot 1} \cdot \nabla\phi \, \mathrm{d}\Omega \\ = & \oint_{\partial\Omega(t)} \left(n_1\overline{\sigma}_{11} + n_2\overline{\sigma}_{21}\right)\phi \, \mathrm{d}\Gamma + \int_{\Omega(t)} -\overline{\sigma}_{11}\frac{\partial\phi}{\partial x} - \overline{\sigma}_{21}\frac{\partial\phi}{\partial y} \, \mathrm{d}\Omega \\ = & \oint_{\partial\Omega(t)} n_1\left(\left(\mu_1+\mu_2\right)\frac{\partial v_1}{\partial x} + \mu_2\frac{\partial v_2}{\partial y}\right)\phi + n_2\frac{\mu_1}{2}\left(\frac{\partial v_1}{\partial y} + \frac{\partial v_2}{\partial x}\right)\phi \, \mathrm{d}\Gamma \\ + & \int_{\Omega(t)} -\left(\left(\mu_1+\mu_2\right)\frac{\partial v_1}{\partial x} + \mu_2\frac{\partial v_2}{\partial y}\right)\frac{\partial\phi}{\partial x} - \frac{\mu_1}{2}\left(\frac{\partial v_1}{\partial y} + \frac{\partial v_2}{\partial x}\right)\frac{\partial\phi}{\partial y} \, \mathrm{d}\Omega. \end{aligned} \tag{A.5.5}$$

Furthermore, according to Equation (A.4.11), we should add the following to the right-hand side of Equation (A.4.22):

$$\begin{aligned} & \oint_{\partial\Omega(t)} \overline{\boldsymbol{\sigma}}_{\cdot 2} \cdot \boldsymbol{n}\phi \, \mathrm{d}\Gamma + \int_{\Omega(t)} -\overline{\boldsymbol{\sigma}}_{\cdot 2} \cdot \nabla\phi \, \mathrm{d}\Omega \\ = & \oint_{\partial\Omega(t)} \left(n_1\overline{\sigma}_{12} + n_2\overline{\sigma}_{22}\right)\phi \, \mathrm{d}\Gamma + \int_{\Omega(t)} -\overline{\sigma}_{12}\frac{\partial\phi}{\partial x} - \overline{\sigma}_{22}\frac{\partial\phi}{\partial y} \, \mathrm{d}\Omega \\ = & \oint_{\partial\Omega(t)} n_1\frac{\mu_1}{2}\left(\frac{\partial v_1}{\partial y} + \frac{\partial v_2}{\partial x}\right)\phi + n_2\left(\mu_2\frac{\partial v_1}{\partial x} + \left(\mu_1+\mu_2\right)\frac{\partial v_2}{\partial y}\right)\phi \mathrm{d}\Gamma \\ + & \int_{\Omega(t)} -\frac{\mu_1}{2}\left(\frac{\partial v_1}{\partial y} + \frac{\partial v_2}{\partial x}\right)\frac{\partial\phi}{\partial x} - \left(\mu_2\frac{\partial v_1}{\partial x} + \left(\mu_1+\mu_2\right)\frac{\partial v_2}{\partial y}\right)\frac{\partial\phi}{\partial y}\mathrm{d}\Omega. \end{aligned} \tag{A.5.6}$$

This means that we have to add the following to the right-hand side of Equation (A.4.23):

$$\begin{aligned} & \Delta t \sum_{i=0}^{N} (v_1)_j^+ \left(\oint_{\partial\Omega^+} n_1^+ \left(\mu_1+\mu_2\right)\phi_i^+ \frac{\partial\phi_j^+}{\partial x} + n_2^+\frac{\mu_1}{2}\phi_i^+\frac{\partial\phi_j^+}{\partial y}\mathrm{d}\Gamma \right) \\ + & \Delta t \sum_{i=0}^{N} (v_1)_j^+ \left(-\int_{\Omega^+} \left(\mu_1+\mu_2\right)\frac{\partial\phi_i^+}{\partial x}\frac{\partial\phi_j^+}{\partial x} + \frac{\mu_1}{2}\frac{\partial\phi_i^+}{\partial y}\frac{\partial\phi_j^+}{\partial y}\mathrm{d}\Omega \right) \\ + & \Delta t \sum_{i=0}^{N} (v_2)_j^+ \left(\oint_{\partial\Omega^+} n_1^+\mu_2\phi_i^+\frac{\partial\phi_j^+}{\partial y} + n_2^+\frac{\mu_1}{2}\phi_i^+\frac{\partial\phi_j^+}{\partial x}\mathrm{d}\Gamma \right) \\ + & \Delta t \sum_{i=0}^{N} (v_2)_j^+ \left(-\int_{\Omega^+} \mu_2\frac{\partial\phi_i^+}{\partial x}\frac{\partial\phi_j^+}{\partial y} + \frac{\mu_1}{2}\frac{\partial\phi_i^+}{\partial y}\frac{\partial\phi_j^+}{\partial x}\mathrm{d}\Omega \right) \end{aligned} \tag{A.5.7}$$

and the following to the right-hand side of Equation (A.4.24):

$$\begin{aligned}
& \Delta t \sum_{i=0}^{N} (v_1)_j^+ \left(\oint_{\partial\Omega^+} n_1^+ \frac{\mu_1}{2} \phi_i^+ \frac{\partial \phi_j^+}{\partial y} + n_2^+ \mu_2 \phi_i^+ \frac{\partial \phi_j^+}{\partial x} \mathrm{d}\Gamma \right) \\
+ \quad & \Delta t \sum_{i=0}^{N} (v_1)_j^+ \left(- \int_{\Omega^+} \frac{\mu_1}{2} \frac{\partial \phi_i^+}{\partial x} \frac{\partial \phi_j^+}{\partial y} + \mu_2 \frac{\partial \phi_i^+}{\partial y} \frac{\partial \phi_j^+}{\partial x} \mathrm{d}\Omega \right) \\
+ \quad & \Delta t \sum_{i=0}^{N} (v_2)_j^+ \left(\oint_{\partial\Omega^+} n_1^+ \frac{\mu_1}{2} \phi_i^+ \frac{\partial \phi_j^+}{\partial x} + n_2^+ \left(\mu_1 + \mu_2\right) \phi_i^+ \frac{\partial \phi_j^+}{\partial y} \mathrm{d}\Gamma \right) \\
+ \quad & \Delta t \sum_{i=0}^{N} (v_2)_j^+ \left(- \int_{\Omega^+} \frac{\mu_1}{2} \frac{\partial \phi_i^+}{\partial x} \frac{\partial \phi_j^+}{\partial x} + \left(\mu_1 + \mu_2\right) \frac{\partial \phi_i^+}{\partial y} \frac{\partial \phi_j^+}{\partial y} \mathrm{d}\Omega \right).
\end{aligned} \tag{A.5.8}$$

This means that Equation (4.2.9) becomes:

$$\begin{aligned}
\rho M_1^{k+1} \boldsymbol{v}_1^{k+1} &= \rho M_1^k \boldsymbol{v}_1^k \\
&+ \Delta t \frac{E_s \sqrt{\rho}}{1+\eta} \left(\left(\frac{1-\eta}{1-2\eta} S_1^{k+1} + \frac{1}{2} S_2^{k+1} \right) \boldsymbol{u}_1^{k+1} + \left(\frac{\eta}{1-2\eta} S_3^{k+1} + \frac{1}{2} S_4^{k+1} \right) \boldsymbol{u}_2^{k+1} \right) \\
&+ \Delta t \left(\left(\left(\mu_1 + \mu_2\right) S_1^{k+1} + \frac{\mu_1}{2} S_2^{k+1} \right) \boldsymbol{v}_1^{k+1} + \left(\mu_2 S_3^{k+1} + \frac{\mu_1}{2} S_4^{k+1} \right) \boldsymbol{v}_2^{k+1} \right) \\
&+ \Delta t \boldsymbol{f}_1^{k+1}
\end{aligned} \tag{A.5.9}$$

and Equation (4.2.10) becomes:

$$\begin{aligned}
\rho M_1^{k+1} \boldsymbol{v}_2^{k+1} &= \rho M_1^k \boldsymbol{v}_2^k \\
&+ \Delta t \frac{E_s \sqrt{\rho}}{1+\eta} \left(\left(\frac{\eta}{1-2\eta} S_4^{k+1} + \frac{1}{2} S_3^{k+1} \right) \boldsymbol{u}_1^{k+1} + \left(\frac{1-\eta}{1-2\eta} S_2^{k+1} + \frac{1}{2} S_1^{k+1} \right) \boldsymbol{u}_2^{k+1} \right) \\
&+ \Delta t \left(\left(\frac{\mu_1}{2} S_3^{k+1} + \mu_2 S_4^{k+1} \right) \boldsymbol{v}_1^{k+1} + \left(\frac{\mu_1}{2} S_1^{k+1} + \left(\mu_1 + \mu_2\right) S_2^{k+1} \right) \boldsymbol{v}_2^{k+1} \right) \\
&+ \Delta t \boldsymbol{f}_2^{k+1}.
\end{aligned} \tag{A.5.10}$$

A.6. Two-dimensional Morphoelastic model

In the morphoelastic model, the Strain Evolution Equations are added:

$$\frac{\mathrm{D}\varepsilon_{11}}{\mathrm{D}t} + \varepsilon_{11} \nabla \cdot \boldsymbol{v} = (1-\varepsilon_{22}) \frac{\partial v_1}{\partial x} + \varepsilon_{11} \frac{\partial v_2}{\partial y} + \frac{1}{2} (\varepsilon_{21} + \varepsilon_{12}) \left(\frac{\partial v_1}{\partial y} - \frac{\partial v_2}{\partial x} \right) - g_{11}, \tag{A.6.1}$$

$$\frac{\mathrm{D}\varepsilon_{12}}{\mathrm{D}t} + \varepsilon_{12} \nabla \cdot \boldsymbol{v} = \varepsilon_{12} \nabla \cdot \boldsymbol{v} + \frac{1}{2} \left((1-2\varepsilon_{11}) \frac{\partial v_1}{\partial y} + (1-2\varepsilon_{22}) \frac{\partial v_2}{\partial x} \right) - g_{12}, \tag{A.6.2}$$

$$\frac{\mathrm{D}\varepsilon_{22}}{\mathrm{D}t} + \varepsilon_{22} \nabla \cdot \boldsymbol{v} = (1-\varepsilon_{11}) \frac{\partial v_2}{\partial y} + \varepsilon_{22} \frac{\partial v_1}{\partial x} - \frac{1}{2} (\varepsilon_{12} + \varepsilon_{21}) \left(\frac{\partial v_1}{\partial y} - \frac{\partial v_2}{\partial x} \right) - g_{22}. \tag{A.6.3}$$

We derive the weak form of these equations, as usual. For the left-hand side of Equation (A.6.10), we have:

$$\begin{aligned}
\int_{\Omega(t)} \left(\frac{\mathrm{D}\varepsilon_{11}}{\mathrm{D}t} + \varepsilon_{11} \nabla \cdot \boldsymbol{v} \right) \phi \mathrm{d}\Omega &= \int_{\Omega(t)} \frac{\mathrm{D}(\varepsilon_{11}\phi)}{\mathrm{D}t} + \varepsilon_{11} \phi \nabla \cdot \boldsymbol{v} \, \mathrm{d}\Omega \\
&= \int_{\Omega(t)} \frac{\partial (\varepsilon_{11}\phi)}{\partial t} + \boldsymbol{v} \cdot \nabla (\varepsilon_{11}\phi) + \varepsilon_{11} \phi \nabla \cdot \boldsymbol{v} \, \mathrm{d}\Omega \\
&= \int_{\Omega(t)} \frac{\partial (\varepsilon_{11}\phi)}{\partial t} + \nabla \cdot (\varepsilon_{11} \phi \boldsymbol{v}) \, \mathrm{d}\Omega.
\end{aligned} \tag{A.6.4}$$

Note that

$$\begin{aligned}
\int_{\Omega(t)} \frac{\partial (\varepsilon_{11}\phi)}{\partial t} \mathrm{d}\Omega &= \frac{\mathrm{d}}{\mathrm{d}t} \left(\int_{\Omega(t)} \varepsilon_{11} \phi \mathrm{d}\Omega \right) - \oint_{\partial\Omega(t)} \varepsilon_{11} \phi \boldsymbol{v} \cdot \boldsymbol{n} \, \mathrm{d}\Gamma \\
&= \frac{\mathrm{d}}{\mathrm{d}t} \left(\int_{\Omega(t)} \varepsilon_{11} \phi \mathrm{d}\Omega \right) - \int_{\Omega(t)} \nabla \cdot (\varepsilon_{11} \phi \boldsymbol{v}) \, \mathrm{d}\Omega.
\end{aligned} \tag{A.6.5}$$

Combining Equation (A.6.4) and (A.6.5) yields

$$\int_{\Omega(t)} \left(\frac{\mathrm{D}\varepsilon_{11}}{\mathrm{D}t} + \varepsilon_{11} \nabla \cdot \boldsymbol{v} \right) \phi \, \mathrm{d}\Omega = \frac{\mathrm{d}}{\mathrm{d}t} \left(\int_{\Omega(t)} \varepsilon_{11} \phi \mathrm{d}\Omega \right). \tag{A.6.6}$$

The same can be done for the left-hand side of Equation (A.6.11) and (A.6.12). Hence, we have weak forms

$$\begin{aligned}
&\frac{\mathrm{d}}{\mathrm{d}t} \left(\int_{\Omega(t)} \varepsilon_{11} \phi \, \mathrm{d}\Omega \right) = \\
&\qquad \int_{\Omega(t)} \left((1 - \varepsilon_{22}) \frac{\partial v_1}{\partial x} + \varepsilon_{11} \frac{\partial v_2}{\partial y} + \frac{1}{2} (\varepsilon_{21} + \varepsilon_{12}) \left(\frac{\partial v_1}{\partial y} - \frac{\partial v_2}{\partial x} \right) - g_{11} \right) \phi \, \mathrm{d}\Omega, \qquad \text{(A.6.7)} \\
&\frac{\mathrm{d}}{\mathrm{d}t} \left(\int_{\Omega(t)} \varepsilon_{12} \phi \, \mathrm{d}\Omega \right) = \\
&\qquad \int_{\Omega(t)} \left(\varepsilon_{12} \nabla \cdot \boldsymbol{v} + \frac{1}{2} \left((1 - 2\varepsilon_{11}) \frac{\partial v_1}{\partial y} + (1 - 2\varepsilon_{22}) \frac{\partial v_2}{\partial x} \right) - g_{12} \right) \phi \, \mathrm{d}\Omega, \qquad \text{(A.6.8)} \\
&\frac{\mathrm{d}}{\mathrm{d}t} \left(\int_{\Omega(t)} \varepsilon_{22} \phi \, \mathrm{d}\Omega \right) = \\
&\qquad \int_{\Omega(t)} \left((1 - \varepsilon_{11}) \frac{\partial v_2}{\partial y} + \varepsilon_{22} \frac{\partial v_1}{\partial x} - \frac{1}{2} (\varepsilon_{12} + \varepsilon_{21}) \left(\frac{\partial v_1}{\partial y} - \frac{\partial v_2}{\partial x} \right) - g_{22} \right) \phi \, \mathrm{d}\Omega. \qquad \text{(A.6.9)}
\end{aligned}$$

As in the one-dimensional case, we take $g_{ij} := \xi \varepsilon_{ij}$, a linear relationship. Using again linear basis functions and applying Euler Backward time integration, we obtain the following Galerkin equations:

$$\begin{aligned}
(1 + \xi \Delta t) \sum_{j=0}^{N} (\varepsilon_{11})_j^+ \int_{\Omega^+} \phi_i^+ \phi_j^+ \, \mathrm{d}\Omega \quad &= \quad \sum_{j=0}^{N} (\varepsilon_{11})_j \int_{\Omega(t)} \phi_i \phi_j \, \mathrm{d}\Omega \\
&+ \quad \Delta t \sum_{j=0}^{N} (v_1)_j^+ \int_{\Omega^+} \phi_i^+ \frac{\partial \phi_j^+}{\partial x} \mathrm{d}\Omega \\
&- \quad \Delta t \sum_{l=0}^{N} (\varepsilon_{22})_j^+ \sum_{j=0}^{N} (v_1)_k^+ \int_{\Omega^+} \phi_i^+ \frac{\partial \phi_j^+}{\partial x} \phi_l^+ \, \mathrm{d}\Omega \\
&+ \quad \Delta t \sum_{l=0}^{N} (\varepsilon_{11})_j^+ \sum_{j=0}^{N} (v_2)_k^+ \int_{\Omega^+} \phi_i^+ \frac{\partial \phi_j^+}{\partial y} \phi_l^+ \, \mathrm{d}\Omega \\
&+ \quad \Delta t \sum_{l=0}^{N} (\varepsilon_{12})_j^+ \sum_{j=0}^{N} (v_1)_k^+ \int_{\Omega^+} \phi_i^+ \frac{\partial \phi_j^+}{\partial y} \phi_l^+ \, \mathrm{d}\Omega \\
&- \quad \Delta t \sum_{l=0}^{N} (\varepsilon_{12})_j^+ \sum_{j=0}^{N} (v_2)_k^+ \int_{\Omega^+} \phi_i^+ \frac{\partial \phi_j^+}{\partial x} \phi_l^+ \, \mathrm{d}\Omega
\end{aligned}$$

and

$$\begin{aligned}(1+\xi\Delta t)\sum_{j=0}^{N}(\varepsilon_{12})_j^+\int_{\Omega^+}\phi_i^+\phi_j^+\,\mathrm{d}\Omega &= \sum_{j=0}^{N}(\varepsilon_{12})_j\int_{\Omega(t)}\phi_i\phi_j\,\mathrm{d}\Omega\\ &+ \Delta t\sum_{l=0}^{N}(\varepsilon_{12})_j^+\sum_{j=0}^{N}(v_1)_k^+\int_{\Omega^+}\phi_i^+\frac{\partial\phi_j^+}{\partial x}\phi_l^+\,\mathrm{d}\Omega\\ &+ \Delta t\sum_{l=0}^{N}(\varepsilon_{12})_j^+\sum_{j=0}^{N}(v_2)_k^+\int_{\Omega^+}\phi_i^+\frac{\partial\phi_j^+}{\partial y}\phi_l^+\,\mathrm{d}\Omega\\ &+ \frac{\Delta t}{2}\sum_{j=0}^{N}(v_1)_j^+\int_{\Omega^+}\phi_i^+\frac{\partial\phi_j^+}{\partial y}\mathrm{d}\Omega\\ &- \Delta t\sum_{l=0}^{N}(\varepsilon_{11})_j^+\sum_{j=0}^{N}(v_1)_k^+\int_{\Omega^+}\phi_i^+\frac{\partial\phi_j^+}{\partial y}\phi_l^+\,\mathrm{d}\Omega\\ &+ \frac{\Delta t}{2}\sum_{j=0}^{N}(v_2)_j^+\int_{\Omega^+}\phi_i^+\frac{\partial\phi_j^+}{\partial x}\mathrm{d}\Omega\\ &- \Delta t\sum_{l=0}^{N}(\varepsilon_{22})_j^+\sum_{j=0}^{N}(v_2)_k^+\int_{\Omega^+}\phi_i^+\frac{\partial\phi_j^+}{\partial x}\phi_l^+\,\mathrm{d}\Omega\end{aligned}$$

and

$$\begin{aligned}(1+\xi\Delta t)\sum_{j=0}^{N}(\varepsilon_{22})_j^+\int_{\Omega^+}\phi_i^+\phi_j^+\,\mathrm{d}\Omega &= \sum_{j=0}^{N}(\varepsilon_{22})_j\int_{\Omega(t)}\phi_i\phi_j\,\mathrm{d}\Omega\\ &+ \Delta t\sum_{j=0}^{N}(v_2)_j^+\int_{\Omega^+}\phi_i^+\frac{\partial\phi_j^+}{\partial y}\mathrm{d}\Omega\\ &- \Delta t\sum_{l=0}^{N}(\varepsilon_{11})_j^+\sum_{j=0}^{N}(v_2)_k^+\int_{\Omega^+}\phi_i^+\frac{\partial\phi_j^+}{\partial y}\phi_l^+\,\mathrm{d}\Omega\\ &+ \Delta t\sum_{l=0}^{N}(\varepsilon_{22})_j^+\sum_{j=0}^{N}(v_1)_k^+\int_{\Omega^+}\phi_i^+\frac{\partial\phi_j^+}{\partial x}\phi_l^+\,\mathrm{d}\Omega\\ &+ \Delta t\sum_{l=0}^{N}(\varepsilon_{12})_j^+\sum_{j=0}^{N}(v_1)_k^+\int_{\Omega^+}\phi_i^+\frac{\partial\phi_j^+}{\partial y}\phi_l^+\,\mathrm{d}\Omega\\ &- \Delta t\sum_{l=0}^{N}(\varepsilon_{12})_j^+\sum_{j=0}^{N}(v_2)_k^+\int_{\Omega^+}\phi_i^+\frac{\partial\phi_j^+}{\partial x}\phi_l^+\,\mathrm{d}\Omega.\end{aligned}$$

Note that these equations are nonlinear. We can write this as three systems

$$(1+\xi\Delta t)\,M_1^{k+1}\boldsymbol{\varepsilon}_{11}^{k+1} = M_1^k\boldsymbol{\varepsilon}_{11}^k+\Delta t\,T_1^{k+1}\boldsymbol{v}_1^{k+1}+\Delta t\,\boldsymbol{f}_{\varepsilon_{11}}^{k+1}(\boldsymbol{w}^{k+1}), \tag{A.6.10}$$

$$(1+\xi\Delta t)\,M_1^{k+1}\boldsymbol{\varepsilon}_{12}^{k+1} = M_1^k\boldsymbol{\varepsilon}_{12}^k+\frac{\Delta t}{2}\left(T_2^{k+1}\boldsymbol{v}_1^{k+1}+T_1^{k+1}\boldsymbol{v}_2^{k+1}\right)+\Delta t\,\boldsymbol{f}_{\varepsilon_{12}}^{k+1}(\boldsymbol{w}^{k+1}), \tag{A.6.11}$$

$$(1+\xi\Delta t)\,M_1^{k+1}\boldsymbol{\varepsilon}_{22}^{k+1} = M_1^k\boldsymbol{\varepsilon}_{22}^k+\Delta t\,T_2^{k+1}\boldsymbol{v}_2^{k+1}+\Delta t\,\boldsymbol{f}_{\varepsilon_{22}}^{k+1}(\boldsymbol{w}^{k+1}). \tag{A.6.12}$$

Here, T_1 and T_2 are $(N+1)\times(N+1)$-matrices, with the following element matrices:

$$(T_1^k)_e = \frac{|\Delta|_e^k}{6}\begin{pmatrix}\beta_1 & \beta_2 & \beta_3\\ \beta_1 & \beta_2 & \beta_3\\ \beta_1 & \beta_2 & \beta_3\end{pmatrix}, \tag{A.6.13}$$

$$(T_2^k)_e = \frac{|\Delta|_e^k}{6}\begin{pmatrix}\gamma_1 & \gamma_2 & \gamma_3\\ \gamma_1 & \gamma_2 & \gamma_3\\ \gamma_1 & \gamma_2 & \gamma_3\end{pmatrix}. \tag{A.6.14}$$

Furthermore,

$$\boldsymbol{\varepsilon}^k_{d_1d_2} := \left((\varepsilon_{d_1d_2})^k_0, \ldots, (\varepsilon_{d_1d_2})^k_N\right)^T, \qquad d_1, d_2 \in \{1,2\},$$

and

$$\boldsymbol{w}^k := (\boldsymbol{\varepsilon}^k_{11}, \boldsymbol{\varepsilon}^k_{12}, \boldsymbol{\varepsilon}^k_{22}, \boldsymbol{v}^k_1, \boldsymbol{v}^k_2)^T.$$

Note that $\boldsymbol{f}^{k+1}_{\varepsilon_{11}}$, $\boldsymbol{f}^{k+1}_{\varepsilon_{12}}$ and $\boldsymbol{f}^{k+1}_{\varepsilon_{22}}$ are vector-valued functions of $\boldsymbol{w}^k$ with length $N+1$. The element vectors are defined as

$$(\boldsymbol{f}^k_{\varepsilon_{11}}(\boldsymbol{w}^k))_e := \frac{|\Delta|^k_e}{24}\begin{pmatrix} -\left[\boldsymbol{\beta}_e\cdot(\boldsymbol{v}_1)_e\right]\bar{\boldsymbol{\varepsilon}}^1_{22} + \left[\boldsymbol{\gamma}_e\cdot(\boldsymbol{v}_2)_e\right]\bar{\boldsymbol{\varepsilon}}^1_{11} + \left[\boldsymbol{\gamma}_e\cdot(\boldsymbol{v}_1)_e - \boldsymbol{\beta}_e\cdot(\boldsymbol{v}_2)_e\right]\bar{\boldsymbol{\varepsilon}}^1_{12} \\ -\left[\boldsymbol{\beta}_e\cdot(\boldsymbol{v}_1)_e\right]\bar{\boldsymbol{\varepsilon}}^2_{22} + \left[\boldsymbol{\gamma}_e\cdot(\boldsymbol{v}_2)_e\right]\bar{\boldsymbol{\varepsilon}}^2_{11} + \left[\boldsymbol{\gamma}_e\cdot(\boldsymbol{v}_1)_e - \boldsymbol{\beta}_e\cdot(\boldsymbol{v}_2)_e\right]\bar{\boldsymbol{\varepsilon}}^2_{12} \\ -\left[\boldsymbol{\beta}_e\cdot(\boldsymbol{v}_1)_e\right]\bar{\boldsymbol{\varepsilon}}^3_{22} + \left[\boldsymbol{\gamma}_e\cdot(\boldsymbol{v}_2)_e\right]\bar{\boldsymbol{\varepsilon}}^3_{11} + \left[\boldsymbol{\gamma}_e\cdot(\boldsymbol{v}_1)_e - \boldsymbol{\beta}_e\cdot(\boldsymbol{v}_2)_e\right]\bar{\boldsymbol{\varepsilon}}^3_{12} \end{pmatrix}, \tag{A.6.15}$$

$$(\boldsymbol{f}^k_{\varepsilon_{12}}(\boldsymbol{w}^k))_e := \frac{|\Delta|^k_e}{24}\begin{pmatrix} \left[\boldsymbol{\beta}_e\cdot(\boldsymbol{v}_1)_e + \boldsymbol{\gamma}_e\cdot(\boldsymbol{v}_2)_e\right]\bar{\boldsymbol{\varepsilon}}^1_{12} - \left[\boldsymbol{\gamma}_e\cdot(\boldsymbol{v}_1)_e\right]\bar{\boldsymbol{\varepsilon}}^1_{11} - \left[\boldsymbol{\beta}_e\cdot(\boldsymbol{v}_2)_e\right]\bar{\boldsymbol{\varepsilon}}^1_{22} \\ \left[\boldsymbol{\beta}_e\cdot(\boldsymbol{v}_1)_e + \boldsymbol{\gamma}_e\cdot(\boldsymbol{v}_2)_e\right]\bar{\boldsymbol{\varepsilon}}^2_{12} - \left[\boldsymbol{\gamma}_e\cdot(\boldsymbol{v}_1)_e\right]\bar{\boldsymbol{\varepsilon}}^2_{11} - \left[\boldsymbol{\beta}_e\cdot(\boldsymbol{v}_2)_e\right]\bar{\boldsymbol{\varepsilon}}^2_{22} \\ \left[\boldsymbol{\beta}_e\cdot(\boldsymbol{v}_1)_e + \boldsymbol{\gamma}_e\cdot(\boldsymbol{v}_2)_e\right]\bar{\boldsymbol{\varepsilon}}^3_{12} - \left[\boldsymbol{\gamma}_e\cdot(\boldsymbol{v}_1)_e\right]\bar{\boldsymbol{\varepsilon}}^3_{11} - \left[\boldsymbol{\beta}_e\cdot(\boldsymbol{v}_2)_e\right]\bar{\boldsymbol{\varepsilon}}^3_{22} \end{pmatrix} \tag{A.6.16}$$

and

$$(\boldsymbol{f}^k_{\varepsilon_{22}}(\boldsymbol{w}^k))_e := \frac{|\Delta|^k_e}{24}\begin{pmatrix} -\left[\boldsymbol{\gamma}_e\cdot(\boldsymbol{v}_2)_e\right]\bar{\boldsymbol{\varepsilon}}^1_{11} + \left[\boldsymbol{\beta}_e\cdot(\boldsymbol{v}_1)_e\right]\bar{\boldsymbol{\varepsilon}}^1_{22} + \left[\boldsymbol{\gamma}_e\cdot(\boldsymbol{v}_1)_e - \boldsymbol{\beta}_e\cdot(\boldsymbol{v}_2)_e\right]\bar{\boldsymbol{\varepsilon}}^1_{12} \\ -\left[\boldsymbol{\gamma}_e\cdot(\boldsymbol{v}_2)_e\right]\bar{\boldsymbol{\varepsilon}}^2_{11} + \left[\boldsymbol{\beta}_e\cdot(\boldsymbol{v}_1)_e\right]\bar{\boldsymbol{\varepsilon}}^2_{22} + \left[\boldsymbol{\gamma}_e\cdot(\boldsymbol{v}_1)_e - \boldsymbol{\beta}_e\cdot(\boldsymbol{v}_2)_e\right]\bar{\boldsymbol{\varepsilon}}^2_{12} \\ -\left[\boldsymbol{\gamma}_e\cdot(\boldsymbol{v}_2)_e\right]\bar{\boldsymbol{\varepsilon}}^3_{11} + \left[\boldsymbol{\beta}_e\cdot(\boldsymbol{v}_1)_e\right]\bar{\boldsymbol{\varepsilon}}^3_{22} + \left[\boldsymbol{\gamma}_e\cdot(\boldsymbol{v}_1)_e - \boldsymbol{\beta}_e\cdot(\boldsymbol{v}_2)_e\right]\bar{\boldsymbol{\varepsilon}}^3_{12} \end{pmatrix}. \tag{A.6.17}$$

Here,

$$\boldsymbol{\beta}_e := (\beta_{p1}, \beta_{p2}, \beta_{p3})^T, \qquad \boldsymbol{\gamma}_e := (\gamma_{p1}, \gamma_{p2}, \gamma_{p3})^T.$$

Furthermore,

$$(\boldsymbol{v}_d)_e := ((v_d)_{p_1}, (v_d)_{p_2}, (v_d)_{p_3})^T$$

and

$$\bar{\boldsymbol{\varepsilon}}^i_{d_1d_2} := (\varepsilon_{d_1d_2})_{p_1} + (\varepsilon_{d_1d_2})_{p_2} + (\varepsilon_{d_1d_2})_{p_3} + (\varepsilon_{d_1d_2})_{p_i}.$$

In the morphoelastic model, we are solving for $\underline{\underline{\varepsilon}}$ and $\boldsymbol{v}$. Hence, after time integration and introducing the Finite Element approximations, Equation (A.4.16) and (A.4.17) result in

$$\begin{aligned} \rho\sum_{j=0}^N (v_1)^+_j \int_{\Omega^+}\phi^+_i\phi^+_j\,\mathrm{d}\Omega &= \rho\sum_{j=0}^N (v_1)_j\int_{\Omega(t)}\phi_i\phi_j\,\mathrm{d}\Omega \\ &- \Delta t\frac{E_s\sqrt{\rho}}{1+\eta}\frac{1-\eta}{1-2\eta}\sum_{j=0}^N(\varepsilon_{11})^+_j\int_{\Omega^+}\frac{\partial\phi^+_i}{\partial x}\phi^+_j\,\mathrm{d}\Omega \\ &- \Delta t\frac{E_s\sqrt{\rho}}{1+\eta}\sum_{j=0}^N(\varepsilon_{12})^+_j\int_{\Omega^+}\frac{\partial\phi^+_i}{\partial y}\phi^+_j\,\mathrm{d}\Omega \\ &- \Delta t\frac{E_s\sqrt{\rho}}{1+\eta}\frac{\eta}{1-2\eta}\sum_{j=0}^N(\varepsilon_{22})^+_j\int_{\Omega^+}\frac{\partial\phi^+_i}{\partial x}\phi^+_j\,\mathrm{d}\Omega \\ &+ \Delta t\int_{\Omega^+}f^+_1\phi^+_i\,\mathrm{d}\Omega \end{aligned} \tag{A.6.18}$$

and

$$\begin{aligned} \rho\sum_{j=0}^N (v_2)^+_j \int_{\Omega^+}\phi^+_i\phi^+_j\,\mathrm{d}\Omega &= \rho\sum_{j=0}^N (v_2)_j\int_{\Omega(t)}\phi_i\phi_j\,\mathrm{d}\Omega \\ &- \Delta t\frac{E_s\sqrt{\rho}}{1+\eta}\frac{\eta}{1-2\eta}\sum_{j=0}^N(\varepsilon_{11})^+_j\int_{\Omega^+}\frac{\partial\phi^+_i}{\partial y}\phi^+_j\,\mathrm{d}\Omega \\ &- \Delta t\frac{E_s\sqrt{\rho}}{1+\eta}\sum_{j=0}^N(\varepsilon_{12})^+_j\int_{\Omega^+}\frac{\partial\phi^+_i}{\partial x}\phi^+_j\,\mathrm{d}\Omega \\ &- \Delta t\frac{E_s\sqrt{\rho}}{1+\eta}\frac{1-\eta}{1-2\eta}\sum_{j=0}^N(\varepsilon_{22})^+_j\int_{\Omega^+}\frac{\partial\phi^+_i}{\partial y}\phi^+_j\,\mathrm{d}\Omega \\ &+ \Delta t\int_{\Omega^+}f^+_2\phi^+_i\,\mathrm{d}\Omega. \end{aligned} \tag{A.6.19}$$

This yields elastic systems

$$\begin{aligned}\rho M_1^{k+1}\boldsymbol{v}_1^{k+1} = \rho M_1^k \boldsymbol{v}_1^k &+ \Delta t\frac{E_s\sqrt{\rho}}{1+\eta}\left(\frac{1-\eta}{1-2\eta}P_1^{k+1}\boldsymbol{\varepsilon}_{11}^{k+1} + P_2^{k+1}\boldsymbol{\varepsilon}_{12}^{k+1} + \frac{\eta}{1-2\eta}P_1^{k+1}\boldsymbol{\varepsilon}_{22}^{k+1}\right)\\ &+ \Delta t\left(\left(\left(\mu_1+\mu_2\right)S_1^{k+1} + \frac{\mu_1}{2}S_2^{k+1}\right)\boldsymbol{v}_1^{k+1} + \left(\mu_2 S_3^{k+1} + \frac{\mu_1}{2}S_4^{k+1}\right)\boldsymbol{v}_2^{k+1}\right) \quad \text{(A.6.20)}\\ &+ \Delta t\boldsymbol{f}_1^{k+1} \quad \text{(A.6.21)}\end{aligned}$$

and

$$\begin{aligned}\rho M_1^{k+1}\boldsymbol{v}_2^{k+1} = \rho M_1^k \boldsymbol{v}_2^k &+ \Delta t\frac{E_s\sqrt{\rho}}{1+\eta}\left(\frac{\eta}{1-2\eta}P_2^{k+1}\boldsymbol{\varepsilon}_{11}^{k+1} + P_1^{k+1}\boldsymbol{\varepsilon}_{12}^{k+1} + \frac{1-\eta}{1-2\eta}P_2^{k+1}\boldsymbol{\varepsilon}_{22}^{k+1}\right)\\ &+ \Delta t\left(\left(\frac{\mu_1}{2}S_3^{k+1} + \mu_2 S_4^{k+1}\right)\boldsymbol{v}_1^{k+1} + \left(\frac{\mu_1}{2}S_1^{k+1} + \left(\mu_1+\mu_2\right)S_2^{k+1}\right)\boldsymbol{v}_2^{k+1}\right) \quad \text{(A.6.22)}\\ &+ \Delta t\boldsymbol{f}_2^{k+1}. \quad \text{(A.6.23)}\end{aligned}$$

Here, P_1^k and P_2^k are $(N+1)\times(N+1)$-matrices with corresponding element matrices:

$$(P_1^k)_e = -\frac{|\Delta|_e^k}{6}\begin{pmatrix}\beta_1 & \beta_1 & \beta_1\\ \beta_2 & \beta_2 & \beta_2\\ \beta_3 & \beta_3 & \beta_3\end{pmatrix}, \quad \text{(A.6.24)}$$

$$(P_2^k)_e = -\frac{|\Delta|_e^k}{6}\begin{pmatrix}\gamma_1 & \gamma_1 & \gamma_1\\ \gamma_2 & \gamma_2 & \gamma_2\\ \gamma_3 & \gamma_3 & \gamma_3\end{pmatrix}. \quad \text{(A.6.25)}$$

In the morphoelastic model, we can replace the elastic part of Equation (A.5.9) and (A.5.10) with these equations. Now we can write Equations (A.6.10), (A.6.11), (A.6.12), (A.6.20) and (A.6.21) in one single system, namely:

$$\overline{M}^{k+1}\boldsymbol{w}^{k+1} = M^k\boldsymbol{w}^k + \Delta t S^{k+1}\boldsymbol{w}^{k+1} + \Delta t\boldsymbol{f}^{k+1}(\boldsymbol{w}^{k+1}), \quad \text{(A.6.26)}$$

where

$$\overline{M}^k := \begin{pmatrix}(1+\xi\Delta t)M_1^k & \mathrm{O} & \mathrm{O} & \mathrm{O} & \mathrm{O}\\ \mathrm{O} & (1+\xi\Delta t)M_1^k & \mathrm{O} & \mathrm{O} & \mathrm{O}\\ \mathrm{O} & \mathrm{O} & (1+\xi\Delta t)M_1^k & \mathrm{O} & \mathrm{O}\\ \mathrm{O} & \mathrm{O} & \mathrm{O} & \rho M_1^k & \mathrm{O}\\ \mathrm{O} & \mathrm{O} & \mathrm{O} & \mathrm{O} & \rho M_1^k\end{pmatrix}, \quad \text{(A.6.27)}$$

$$M^k := \begin{pmatrix}M_1^k & \mathrm{O} & \mathrm{O} & \mathrm{O} & \mathrm{O}\\ \mathrm{O} & M_1^k & \mathrm{O} & \mathrm{O} & \mathrm{O}\\ \mathrm{O} & \mathrm{O} & M_1^k & \mathrm{O} & \mathrm{O}\\ \mathrm{O} & \mathrm{O} & \mathrm{O} & \rho M_1^k & \mathrm{O}\\ \mathrm{O} & \mathrm{O} & \mathrm{O} & \mathrm{O} & \rho M_1^k\end{pmatrix}, \quad \text{(A.6.28)}$$

$$S^k := \begin{pmatrix}\mathrm{O} & \mathrm{O} & \mathrm{O} & T_1^k & \mathrm{O}\\ \mathrm{O} & \mathrm{O} & \mathrm{O} & 0.5T_2^k & 0.5T_1^k\\ \mathrm{O} & \mathrm{O} & \mathrm{O} & \mathrm{O} & T_2^k\\ \bar{E}_s\bar{\eta}_1 P_1^k & \bar{E}_s P_2^k & \bar{E}_s\bar{\eta}_2 P_1^k & \bar{\mu}S_1^k + 0.5\mu_1 S_2^k & \mu_2 S_3^k + 0.5\mu_1 S_4^k\\ \bar{E}_s\bar{\eta}_2 P_2^k & \bar{E}_s P_1^k & \bar{E}_s\bar{\eta}_1 P_2^k & 0.5\mu_1 S_3^k + \mu_2 S_4^k & 0.5\mu_1 S_1^k + \bar{\mu}S_2^k\end{pmatrix} \quad \text{(A.6.29)}$$

and

$$\boldsymbol{f}^k(\boldsymbol{w}^k) := \begin{pmatrix}\boldsymbol{f}_{\varepsilon_{11}}^k(\boldsymbol{w}^k)\\ \boldsymbol{f}_{\varepsilon_{12}}^k(\boldsymbol{w}^k)\\ \boldsymbol{f}_{\varepsilon_{22}}^k(\boldsymbol{w}^k)\\ \boldsymbol{f}_1^k\\ \boldsymbol{f}_2^k\end{pmatrix}. \quad \text{(A.6.30)}$$

Here,

$$\bar{E}_s := \frac{E_s\sqrt{\rho}}{1+\eta}, \qquad \bar{\eta}_1 := \frac{1-\eta}{1-2\eta}, \qquad \bar{\eta}_2 := \frac{\eta}{1-2\eta}, \qquad \bar{\mu} := \mu_1+\mu_2.$$

A.7. Boundary condition

In this subsection, we consider the Robin boundary condition for the two-dimensional model. In (A.4.11), we have that

$$\oint_{\partial\Omega(t)} \boldsymbol{\sigma}_{\cdot d} \cdot \boldsymbol{n}\phi \, \mathrm{d}\Gamma = -a \oint_{\partial\Omega(t)} u_d \phi \, \mathrm{d}\Gamma. \tag{A.7.1}$$

Hence, when carrying out the Euler Backward time integration, we should add the following to the right-handside of the equations:

$$-a \cdot \Delta t \cdot \oint_{\partial\Omega^+} u_d^+ \phi_i^+ \mathrm{d}\Gamma \tag{A.7.2}$$

We approximate $u_d^+ := u_d(t+\Delta t)$ with an backward approximation $u_d(t) + \Delta t \cdot v(t+\Delta t)$. Replacing this and carrying out the Finite Element approximation yields

$$-a \cdot \Delta t \cdot \oint_{\partial\Omega^+} u_d \phi_i^+ \mathrm{d}\Gamma - a \cdot \Delta t^2 \sum_{j=0}^{N} (v_d)_j^+ \oint_{\partial\Omega^+} \phi_j^+ \phi_i^+ \mathrm{d}\Gamma. \tag{A.7.3}$$

The first part

$$-a\Delta t \oint_{\partial\Omega^+} u_d \phi_i^+ \mathrm{d}\Gamma \tag{A.7.4}$$

will cause a boundary vector $-a \cdot \Delta t \cdot \boldsymbol{b}^k$ to be added to the right-handside of the system. Suppose we have a boundary element $be = [\boldsymbol{q}_1^k, \boldsymbol{q}_2^k]$, then the corresponding boundary element vector is:

$$(\boldsymbol{b}_d^k)_{be} = \frac{||\boldsymbol{q}_2^{k+1} - \boldsymbol{q}_1^{k+1}||}{2} \begin{pmatrix} u_d(\boldsymbol{q}_1^k, k\Delta t) \\ u_d(\boldsymbol{q}_2^k, k\Delta t) \end{pmatrix}, \tag{A.7.5}$$

for $d = 1, 2$. Furthermore, the second part of (A.7.3)

$$-a\Delta t \sum_{j=0}^{N} (v_d)_j^+ \oint_{\partial\Omega^+} \phi_j^+ \phi_i^+ \mathrm{d}\Gamma \tag{A.7.6}$$

can be put to the left-handside of the equation. Then a boundary element matrix can be defined with

$$B_{be}^k = a \cdot \frac{||\boldsymbol{q}_2^k - \boldsymbol{q}_1^k||}{6} \begin{pmatrix} 2 & 1 \\ 1 & 2 \end{pmatrix}, \tag{A.7.7}$$

Then the following should be added to the left-handside of the system:

$$\Delta t^2 \begin{pmatrix} B^{k+1} & \mathrm{O} \\ \mathrm{O} & B^{k+1} \end{pmatrix} \boldsymbol{v}^{k+1}. \tag{A.7.8}$$

This holds in the pure elastic and viscoelastic case. In case of the morphoelastic system, the following has to be added to the left-handside:

$$\Delta t^2 \begin{pmatrix} \mathrm{O} & \mathrm{O} & \mathrm{O} & \mathrm{O} & \mathrm{O} \\ \mathrm{O} & \mathrm{O} & \mathrm{O} & \mathrm{O} & \mathrm{O} \\ \mathrm{O} & \mathrm{O} & \mathrm{O} & \mathrm{O} & \mathrm{O} \\ \mathrm{O} & \mathrm{O} & \mathrm{O} & B^{k+1} & \mathrm{O} \\ \mathrm{O} & \mathrm{O} & \mathrm{O} & \mathrm{O} & B^{k+1} \end{pmatrix} \boldsymbol{w}^{k+1}. \tag{A.7.9}$$

Bibliography

[1] Boon, W.M. (2014). *Incorporation of Contracture Formation during Dermal Wound Healing: a Mathematical Model* (master's thesis). Retrieved from http://ta.twi.tudelft.nl/users/vuik/numanal/boon_afst.pdf

[2] Brocks, W., Steglich, D. (2017). *Engineering Mechanics.* [Photograph] Retrieved from https://www.researchgate.net/figure/3-Stress-state-in-a-material-point-The-physical-dimension-of-the-components-of-the_fig4_312948862

[3] Ding, Y., Xu, GK., Wang, GF. (2017). *On the determination of elastic moduli of cells by AFM based indentation.* Sci Rep **7,** 45575. https://doi.org/10.1038/srep45575

[4] Dziuk, G., Elliot, C. (2007). *Finite elements on evolving surfaces* IMA Journal of Numerical Analysis 27(2) DOI 10.1093/imanum/drl023

[5] European Space Agency. (n.d.). *More Moduli?* There is far more to a material than just tensile stiffness. [Photograph] Retrieved from: http://www.spaceflight.esa.int/impress/text/education/Mechanical%20Properties/MoreModuli.html

[6] Geerligs, M. (2006). *In vitro mechanical characterization of human skin layers: stratum corneum, epidermis and hypodermis* (proefschrift) Retrieved from http://www.mate.tue.nl/mate/pdfs/11389.pdf

[7] Gere, J. M., Timoshenko, S.P. (1999). *Mechanics of Materials.* Fourth SI Edition. Cheltenham: Stanley Thornes (Publishers) Ltd

[8] Gorter, W.S. (2020). *Mathematical Model of Elastics* (literature report).

[9] Gorter, W.S. (2019). *Validating Mathematical Model of Burn Injuries* (internship report).

[10] Hall, C. L. (2008). *Modelling of some biological materials using continuum mechanics* (Doctor of Philosophy's thesis). Retrieved from https://eprints.qut.edu.au/37244/

[11] Hofmann, P. (2015). *Relationship between elastic constants* (attachment to *Solid State Physics*). Retrieved from https://philiphofmann.net/solid-state-physics-book/solid-state-notes/

[12] Kleimann, E.D. (2018). *Mathematical modelling of burn injuries* (master's thesis). Retrieved from http://resolver.tudelft.nl/uuid:bb4aec96-0555-4903-9c52-e692ab5ed146

[13] Koppenol, D. (2017). *Biomedical implications from mathematical models for the simulation of dermal wound healing.* Retrieved from https://doi.org/10.4233/uuid:cdc7392f-4ac6-404c-9615-dc425f67efae

[14] OpenStax College. (2013). *Anatomy and physiology* [Photograph]. Houston, TX: OpenStax CNX. Retrieved from http://cnx.org/content/col11496/latest/

[15] Peng, Q., Vermolen F. (2019). *Point forces and their alternatives in cell-based models for skin contraction.* (Reports of the Delft Institute of Applied Mathematics; Vol. 19-03). Delft University of Technology. 1389-6520(19-03)

[16] Peng, Q., Vermolen F. (2020). *Agent-based modelling and parameter sensitivity analysis with a finite-element method for skin contraction.* Biomech Model Mechanobiol 19, 2525–2551 (2020). Retrieved from https://doi.org/10.1007/s10237-020-01354-z

[17] Pinterest. (n.d.). *Comparison of Compression and Tensile Strengths* [Photograph]. Retrieved from https://www.pinterest.com/pin/189925309271703571/

[18] Smits, D. (2019). *Morphoelastic models for burn contraction* (master's thesis). Retrieved from http://resolver.tudelft.nl/uuid:163f140d-35dd-4f35-a9ff-2c580311a10a

[19] Smlease Design (n.d.). *Stress Strain Curve : Strength of Materials* [Photograph]. Retrieved from https://www.smlease.com/entries/mechanical-design-basics/stress-strain-curve-diagram/

[20] StackExchange (n.d.). *Is shear modulus only applicable to cubical solids?* [Photograph]. Retrieved from https://physics.stackexchange.com/questions/139294/is-shear-modulus-only-applicable-to-cubical-solids

[21] Vermolen, F.J., Koppenol, D, Niessen, F. & van Zuijlen, P. (2017). *Wiskundige modellering van contractuur en hypertrofie bij brandwonden.* (Dutch). Retrieved from https://www.wcs.nl/wondwiki/wiskundige-modellering-van-contractuur-en-hypertrofie-bij-brandwonden/

[22] Vermolen, F.J., Gefen, A. (2012). *A semi-stochastic cell-based formalism to model the dynamics of migration of cells in colonies.* Biomechanics and Modelling in Mechanobiology. https://doi.org/10.1007/s10237-011-0302-6

[23] Weihs D., Gefen A. Vermolen F.J. (2016). *Review on experiment-based two- and three-dimensional models for wound healing.* Retrieved from https://europepmc.org/article/pmc/pmc4992741#s4

[24] Wikiwand (n.d.). *Dashpot* [Photograph]. Retrieved from https://www.wikiwand.com/en/Dashpot